Development of Palladium and Non-noble Metal Based Nanocomposite Electrocatalysts Toward Methanol Oxidation in DMFC Applications

THESIS

SUBMITTED IN PARTIAL FULFILMENT OF THE REQUIREMENTS
FOR THE AWARD OF THE DEGREE OF

Doctor of Philosophy

IN

CHEMISTRY

BY

V. SUNIL KUMAR

(Roll No. 714164)

RESEARCH SUPERVISORS

Prof. K. V. GOBI

DEPARTMENT OF CHEMISTRY

NATIONAL INSTITUTE OF TECHNOLOGY WARANGAL

WARANGAL – 506004, TELANGANA, INDIA

JUNE – 2020

DECLARATION

This is to declare that the work presented in the thesis entitled *"Development of Palladium and Non-noble Metal Based Nanocomposite Electrocatalysts Toward Methanol Oxidation in DMFC Applications"* is a bonafide work done by me under the supervision of **Prof. K. V. Gobi**, Professor in the Department of Chemistry, and was not submitted elsewhere for the award of any degree.

I declare that this written submission represents my ideas in my own words, and where others' ideas or words have been included, I have adequately cited and referenced the original sources. I also declare that I have adhered to all principles of academic honesty and integrity and have not misrepresented or fabricated or falsified any idea/data/fact/ source in my submission. I understand that any violation of the above will be a cause for disciplinary action by the Institute and can also evoke penal action from the sources which have thus not been properly cited or from whom proper permission has not been taken when needed.
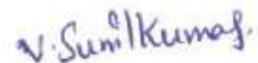
Date: 20-11-2020　　　　　　　　　　　　　　　　　　**(V. Sunil Kumar)**

Place: **NIT Warangal**　　　　　　　　　　　　　　Roll Number: **714164**

CERTIFICATE

This is to certify that the work presented in the thesis entitled *"Development of Palladium and Non-noble Metal Based Nanocomposite Electrocatalysts Toward Methanol Oxidation in DMFC Applications"* is a bonafide work carried out by **Mr. V. Sunil Kumar** under my supervision and was not submitted elsewhere for the award of any degree.

Prof. K. V. GOBI
(Research Supervisor)
Professor
Department of Chemistry
NIT Warangal

ACKNOWLEDGEMENTS
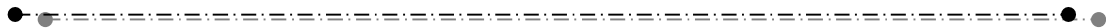
ACKNOWLEDGEMENTS

During the course of my Doctoral Research work, I have received the assistance and support from the following people:

First and foremost, I am truly indebted and I express my earnest gratitude for my Research Supervisor **Prof. K. V. Gobi**, Professor, Department of Chemistry, National Institute of Technology Warangal for his inestimable expertise and astute guidance. His unabated enthusiasm, which stems from his absolute command over the subject, has been a constant source of inspiration for me to work hard and the outcome is expressed in the form of this thesis.

I am grateful to **The Director**, National Institute of Technology, Warangal for giving me the opportunity to carry out the work and allowing me to submit in the form of a thesis. I greatly acknowledge **MHRD** for the financial support in the form of fellowship.

I express my gratitude to the Doctoral Scrutiny Committee members: **Prof. P. V. Srilakshmi**, Chairman and Head, Department of Chemistry, **Prof. K. Laxma Reddy**, Department of Chemistry, **Dr. Vishnu Shankar,** Department of Chemistry, and **Dr. Abdul Azeem,** Department of Physics, NIT Warangal for their detailed review, constructive suggestions and excellent advice during the progress of this research work.

My sincere thanks are due to **former Heads** of the Department of Chemistry during the period of my research work.

I want to thank all the faculty members from the Department of Chemistry, namelyProf. A. Ramachandraiah, Prof. V. Rajeswar Rao, Dr. Venkatathri Narayanan, Dr. Vishnu Shanker, Dr. D. Kashinath, Dr. B. Srinivas, Dr. K. Hari Prasad, Dr. Raghu Chitta, Dr. S. Nagarajan, Dr. M. Ragha Sudha, Dr. Ch. Jugun Prakash, Dr. Ravinder Pawar, Dr. Mukul Pradhan, Dr. Rajeshkhanna Gaddam, Dr. V. Rajeshkumar and all the other faculty members for their valuable advice and encouragement throughout the research work.

I convey my special thanks from the bottom of my heart to my seniors, **Dr. K. Koteshwara Reddy, Dr. M. Satyanarayana, Dr. K. Yugender Goud,** to my juniors **Mr. V.V.N. Phanikumar, Ms. S. Manasa, Mr. K. Shekher, Mr. K. Sampath and Ms. G. Aarti** for their continuous support and encouragement in each and every step of my research work.

Date: 20-11-2020.   **(V. Sunil Kumar)**

CONTENTS

Table of Contents

SYMBOLS AND ABBREVIATIONS

DMFC	:	Direct Methanol Fuel Cell
DLFC	:	Direct Liquid Fuel Cell
MOR	:	Methanol Oxidation Reaction
Å	:	Angstrom
θ	:	Theta
eV	:	Electron volt
cm	:	Centimeter
nm	:	Nanometer
mg	:	Milligram
h	:	Hour
s	:	Seconds
min	:	Minute
ºC	:	Degree centigrade
i	:	Current
E	:	Potential
ν	:	Scan Rate
mA	:	Milliampere
mV	:	Millivolt
μC	:	Microcoulomb
M	:	Molarity
E_{op}	:	Onset potential
GCE	:	Glassy Carbon Electrode
EASA	:	Electrochemical Active Surface Area
CNT	:	Carbon Nanotubes
FCNT	:	Functionalized carbon nanotubes
NBCNT	:	Nitrobenzene functionalized Carbon Nanotubes
GO	:	Graphene Oxide
rGO	:	Reduced Graphene Oxide
NG180	:	N-doped Graphene
CV	:	Cyclic Voltammetry
SEM	:	Scanning Electron Microscopy
FESEM	:	Field Emission Scanning Electron Microscopy
EDS	:	Energy Dispersive X-ray Spectroscopy

TEM	:	Transmission Electron Microscopy
HRTEM	:	High-Resolution Transmission Electron Microscopy
XRD	:	X-ray Diffraction
UV	:	Ultra-violet
XPS	:	X-ray Photoelectron Spectroscopy
TGA	:	Thermogravimetric Analysis

Chapter 1

Introduction

1. Introduction

The consumption of world's energy is progressively increasing from so many years. But the energy production is not reaching the demand. Currently, fossil fuels (oil, coal and natural gas) are the main energy sources to fill the energy demand. However, there are some major problems integrated with the use of fossil fuels. Utilization of fossil fuels majorly emptying the natural resources and lead to the emission of green-house gases, which originates the global warming. So, solving these problems by using cleaner energy sources are prime concern in energy field, in order to preserve the natural resources, to decrease the environmental pollution and to control the green-house effect. Fuel cell is an emerging and promising new technology due to their use of non-depleting, non-fossil and clean sources of fuel. Fuel cells have been known around 150 years ago in the fields of scientific engineering. The fuel cell principle was first demonstrated by a Swiss scientist Christian Schoenberg and first constructed by Sir William Grove in 1839. Fuel cells have been comprehensively investigated during the second half of the 20th and early 21st century[1,2].

A fuel cell is an electrochemical device which converts the chemical energy into electrical energy similar to the battery. Certainly, both fuel cells and batteries belong to Galvanic cells, which represent the known method to produce the electrical energy through a reaction between the chemical ingredients. Since a battery deals with a predetermined supply of chemical reactants as input, it is having a finite work period, beyond which it would not function or it should be recharged. But, in the case of fuel cells, the reactants are stored outside of the cell and the electrical power is produced for long-lasting as the reactants are supplied to it. In addition to producing electricity, the by-products are water and heat. A fuel cell is an efficient device that does not require any moving part to function. However, it is very expensive to manufacture in large scale for widespread commercial and industrial applications. Some of the applications of fuel cells are stationary power (e.g. power generating stations and auxiliary units), transportation (e.g. buses and cars) and portable electronics (e.g. laptops and mobile phones)[2–6].

1.1. Classification of fuel cells

There are various types of fuel cells, categorized based on the type of electrolyte, operating temperature and/or the fuel employed[2,7].

Based on the type of electrolyte:

1. Microbial fuel cell (MFC)

2. Direct methanol fuel cell (DMFC)

3. Proton exchange membrane fuel cell (PEMFC)

4. Alkaline fuel cell (AFC)

5. Phosphoric acid fuel cell (PAFC)

6. Molten carbonate fuel cell (MCFC)

7. Solid oxide fuel cell (SOFC)

8. Regenerative fuel cell (RFC)

Based on operating temperature

1. High temperature fuel cells (800-1000 °C)

2. Medium temperature fuel cells (120-250 °C)

3. Low temperature fuel cells (80-120 °C)

Based on types of fuel and oxidant

1. Hydrogen (pure) - Oxygen (pure) fuel cell

2. Hydrogen rich gas - air fuel cell

3. Hydrocarbon (gas) - air fuel cell

4. Synthetic gas - air fuel cell

5. Ammonia - air fuel cell

Table 1.1. Evaluation of type of fuel cells, their working conditions and characteristics[7].

Type of fuel cell	Anode reaction (A) Cathode reaction (C) Overall reaction (O)	Operating temp (ºC)	Electrolyte material	Primary fuel used	Charge carrier	Applications
MFC	A: $CH_3COOH + 2\ H_2O \rightarrow 2\ CO_2 + 8\ H^+ + 8\ e^-$ C: $8\ H^+ + 8\ e^- + 2\ O_2 \rightarrow 4\ H_2O$ O: $CH_3COOH + 2\ O_2 \rightarrow 2\ CO_2 + 2\ H_2O$	20-30	Proton conducting membrane	Acetic acid (CH_3COOH)	H^+	Stationary power, Wastewater treatment and Biohydrogen production
DMFC	A: $CH_3OH + H_2O \rightarrow CO_2 + 6\ H^+ + 6\ e^-$ C: $1\frac{1}{2}\ O_2 + 6\ e^- + 6\ H^+ \rightarrow 3\ H_2O$ O: $CH_3OH + 1\frac{1}{2}\ O_2 + H_2O \rightarrow CO_2 + 3\ H_2O$	80-90	Proton conducting membrane	Methanol (CH_3OH)	H^+	Transportation and Portable power
PEMFC	A: $H_2 \rightarrow 2\ H^+ + 2\ e^-$ C: $\frac{1}{2}\ O_2 + 2e^- + 2\ H^+ \rightarrow H_2O$ O: $H_2 + \frac{1}{2}\ O_2 \rightarrow H_2O$	80-100	Proton conducting membrane	Pure H_2	H^+	Automotive and Stationary power
AFC	A: $2\ H_2 + 4\ OH^- \rightarrow 4\ H_2O + 4\ e^-$ C: $O_2 + 2\ H_2O + 4\ e^- \rightarrow 4\ OH^-$ O: $2\ H_2 + O_2 \rightarrow 2\ H_2O$	90-120	Potassium hydroxide	Pure H_2	OH^-	Space vehicles and drinking water
PAFC	A: $H_2 \rightarrow 2\ H^+ + 2\ e^-$ C: $\frac{1}{2}\ O_2 + 2\ e^- + 2\ H^+ \rightarrow H_2O$ O: $H_2 + \frac{1}{2}\ O_2 \rightarrow H_2O$	220	Phosphoric acid	Pure H_2	H^+	Stationary power
MCFC	A: $2\ H_2 + 2\ CO_3^{2-} \rightarrow 2\ H_2O + 2\ CO_2 + 4\ e^-$ C: $O_2 + 2\ CO_2 + 4\ e^- \rightarrow 2\ CO_3^{2-}$ O: $2\ H_2 + O_2 \rightarrow 2\ H_2O$	650	Lithium and Potassium carbonate	H_2, CO and CH_4	CO_3^{2-}	Stationary power
SOFC	A: $2\ H_2 + 2\ O^{2-} \rightarrow 2\ H_2O + 4e^-$ C: $O_2 + 4\ e^- \rightarrow 2\ O^{2-}$ O: $2\ H_2 + O_2 \rightarrow 2\ H_2O$	750-1000	Yttrium-stabilized Zirconia oxide	H_2, CO and CH_4	O^{2-}	Stationary power and Transportation
RFC	A: $O^{2-} \rightarrow \frac{1}{2}\ O_2 + 2\ e^-$ C: $H_2O + 2\ e^- \rightarrow H_2 + O^{2-}$ O: $H_2O \rightarrow \frac{1}{2}\ O_2 + H_2$		Yttrium-stabilized Zirconia oxide		O^{2-} and/ or H^+	Automotive, Stationary power and Transportation

1.2. Direct liquid fuel cells (DLFCs)

Direct liquid fuel cells (DLFCs) are one type of fuel cells classified based on the liquid state of the fuel as the energy source and are presently under extensive investigations due to their benefits when compared with polymer electrolyte membrane fuel cells (PEMFCs). In PEMFCs, hydrogen gas fuel typically and selectively stored under high pressure throughout the operation, and this could lead to mishaps such as explosions, if H_2 gas is not being handled properly. It is the key safety issue pertaining to the applications of PEMFCs for widespread commercial use. Additionally, hydrogen fuel is highly flammable and possesses transport and storage problems [7,8]. DLFCs seems to be an alternative type of fuel cell since the source is liquid fuel, and it is also easy in handling the fuel [8–12].
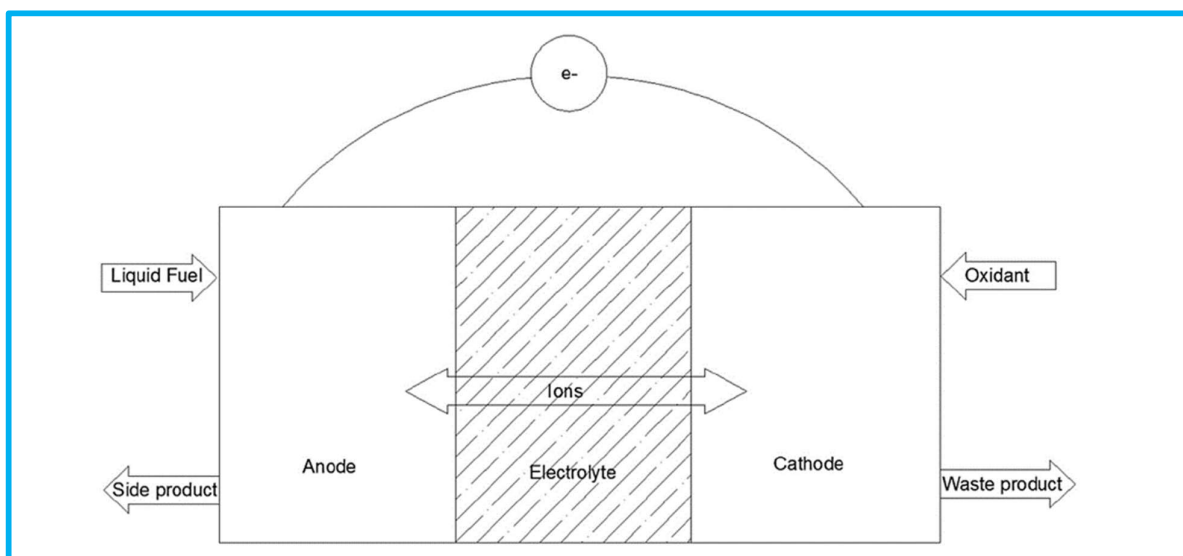
Fig. 1.1. General operating principle of DLFCs.

Many different types of liquid fuels have been used in DLFCs, each one with its own advantages and disadvantages. Alcohols, such as CH_3OH and C_2H_5OH, are the most common sources of fuel in DLFC applications. Non-alcohol fuels, such as sodium borohydride, ammonia-borane, hydrazine, formic acid and dimethyl ether, were also employed in DLFCs. Table 1.2 describes the reactions of these types of fuels as a source and the theoretical energy density and cell potential of the respective fuels in DLFCs[12].

Table 1.2. General reactions of DLFCs with different fuels.

Type of fuel	Reaction		Standard theoretical potential, E^0 (V)	Energy density (Wh L^{-1})
Methanol	Anode Cathode Overall	$CH_3OH + H_2O \rightarrow CO_2 + 6 H^+ + 6 e^-$ $6 H^+ + 6 e^- + (3/2) O_2 \rightarrow 3 H_2O$ $CH_3OH + (3/2) O_2 \rightarrow CO_2 + 2 H_2O$	1.213	4820
Ethanol	Anode Cathode Overall	$C_2H_5OH + 3 H_2O \rightarrow 2 CO_2 + 12 H^+ + 12 e^-$ $12 H^+ + 12 e^- + 3 O_2 \rightarrow 6 H_2O$ $C_2H_5OH + 3 O_2 \rightarrow 2 CO_2 + 3 H_2O$	1.145	6280
Propanol	Anode Cathode Overall	$C_3H_7OH + 5 H_2O \rightarrow 3 CO_2 + 18 H^+ + 18 e^-$ $18 H^+ + (9/2) O_2 + 18e^- \rightarrow 9 H_2O$ $C_3H_7OH + (9/2) O_2 \rightarrow 3 CO_2 + 4 H_2O$	1.122	7080
Ethylene glycol	Anode Cathode Overall	$C_2H_6O_2 + 2 H_2O \rightarrow 2 CO_2 + 10 H^+ + 10 e^-$ $10 H^+ + 10 e^- + (5/2) O_2 \rightarrow 5 H_2O$ $C_2H_6O_2 + (5/2) O_2 \rightarrow 2 CO_2 + 3 H_2O$	1.220	5800
Glycerol	Anode Cathode Overall	$C_3H_8O_3 + 3 H_2O \rightarrow 3 CO_2 + 14 H^+ + 14e^-$ $14 H^+ + 14 e^- + (7/2) O_2 \rightarrow 7 H_2O$ $C_3H_8O_3 + (7/2) O_2 \rightarrow 3 CO_2 + 4 H_2O$	1.210	6400
Formic acid	Anode Cathode Overall	$HCOOH \rightarrow CO_2 + 2 H^+ + 2 e^-$ $2 H^+ + 2 e^- + (1/2) O_2 \rightarrow H_2O$ $HCOOH + (1/2) O_2 \rightarrow CO_2 + H_2O$	1.400	1750
Dimethyl ether	Anode Cathode Overall	$(CH_3)_2O + 3 H_2O \rightarrow 2 CO_2 + 12 H^+ + 12 e^-$ $12 H^+ + 12 e^- + 3 O_2 \rightarrow 6 H_2O$ $(CH_3)_2O + 3 O_2 \rightarrow 2 CO_2 + 3 H_2O$	1.198	5610
Hydrazine	Anode Cathode Overall	$N_2H_4 \rightarrow N_2 + 4 H^+ + 4 e^-$ $4 H^+ + 4 e^- + O_2 \rightarrow 2 H_2O$ $N_2H_4 + O_2 \rightarrow N_2 + 2 H_2O$	1.615	5400
Ammonia borane	Anode Cathode Overall	$BH_2^- + 6 OH^- \rightarrow BO_2^- + 4 H_2O + 6 e^-$ $3 H_2O + 6 e^- + (3/2) O_2 \rightarrow 6 OH^-$ $BH_2^- + (3/2)O_2 \rightarrow BO_2^- + H_2O$	1.620	6100

DLFCs could operate under both acid and alkaline medium, depending on the requirements, as each type has its strengths and weaknesses, as listed in Table 1.3. General comparison between acid and alkaline fuel cell has been presented in the Table.

Table 1.3. General comparison between acid and alkaline fuel cells.

Fuel cell type	Typical electrolyte	Advantages	Disadvantages
Acid	Proton exchange membrane	Start up quickly Higher ion conductivity Less sensitive to contaminant High power density	Requisite for high cost noble catalyst Higher fuel crossover
Alkaline	KOH Anion exchange membrane	Capable to use low cost non-noble catalysts Oxygen reduction reaction (ORR) performs superior under alkaline condition Lower fuel crossover	Lower ion conductivity Formation of carbonates More sensitive to contaminant (Easily poisoned by carbon monoxide)
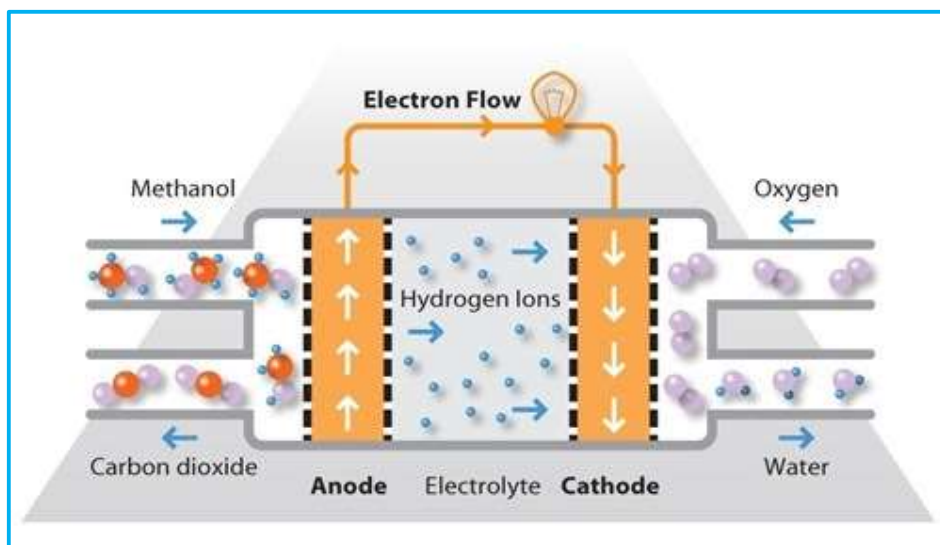
Fig. 1.2. Schematic illustration of DMFC process. (https://hydrogeneurope.eu/fuel-cells).

1.3. Direct methanol fuel cells (DMFCs)

DMFCs are one among the most prevalent type of DLFCs. A huge extent of researchers have been ardent to these type of fuel cells on account of the methanol's admirable properties. Methanol can be employed directly into the anode in the form of liquid deprived of any pre-reforming procedure. Methanol can be easily handled, transported and stored, and it has a high energy to carbon ratio, which creates it as a good fuel[13–15]. Because of its availability,

biodegradable, good electrochemical activity and relatively cheap, DMFC marks its importance in DLFC applications. Compared to other fuels like hydrogen (180 Wh L^{-1}), methanol has a high energy density of 4820 Wh L^{-1}. Apart from this, methanol is mildly toxic, so little care and precautions should be taken while handling it, exclusively when it is employed in commercialization of fuel cell systems. DMFC mainly depend on the oxidation of methanol on the surface of electrocatalyst in order to generate the end product CO_2. H_2O is produced at cathode, which is being consumed at anode side. While the protons (H$^+$) are transported across the proton exchange membrane, which is commonly prepared from Nafion, to cathode side, and at that point they react with oxygen to generate H_2O molecule. Electrons are transported over an external circuit from anode to cathode, generating power to the connected devices, as shown in Fig. 1.2.

1.3.1. DMFC applications

➢ The power generated from the DMFC system is limited, but it can still store a high energy content in a little space. It illustrates that they can generate a small amount of power over a long period of time.

➢ Suitable for smaller vehicles, like forklifts and tuggers.

➢ Suitable for consumer goods and portable electronic devices like laptops, digital cameras and mobile phones.

➢ DMFCs are now becoming an emerging application in the fields of military, because of their unique advantages like low noise, thermal significance and no toxic effluents.

1.4. Nanomaterials and their applications

Nanomaterials are the materials which are having the structural features such as crystallite size or grain size, lamellar spacing, etc. in a very small range of nano-size level between 1 to 100 nm at least in one dimension and predefined superstructure in all three dimensions[16]. They show novel characteristics and specific surface property due to increased strength, hardness, chemical reactivity, high catalytic activity and conductivity[16–18]. Due to nanoscale dimensions, nanomaterials are of remarkable interest to show extraordinary performance, improved functionality, higher activity and long-term durability, because of their unique and tailored electrical, optical, magnetic properties[19,20]. The nanostructured form of metal colloids is described to re-disperse the metals in solution, in small aggregates with zero-valent metal (1-50 nm), that can be stabilized by organic protecting agents such as surfactant, polymer and ligands. The lipophilic or hydrophilic protecting agents are used for stabilizing the metal colloids, with which they become soluble in organic or aqueous solvents. Nanomaterials

are having versatile applications in producing novel catalysts with high selectivity, enhanced reactivity and versatility for multi-component reactions. Further, bimetallic nanostructured materials have synergetic effects, long-term stability and sustainability [21]. Due to this unique physical (electronic, structural, optical and magnetic) as well as chemical (catalytic) properties, various kinds of nanomaterials are produced and investigated in large scales. In addition, the nanomaterials would be made available in different shapes and structures such as spherical, hexagonal, rods, wires, fibers, tubes, sheets, solid, hollow and core-shell structures[22].

Generally, nanomaterials are classified according to their dimensional structures: (i) zero dimension (0D) such as nanoparticles, quantum dots and fullerene; (ii) one dimension (1D) such as nanotubes, nanobelts and nanowires; and (iii) two dimension (2D) such as graphene or reduced graphene oxide, nanofilms and nanowalls[23,24]. Therefore, nanomaterials contain carbon-based materials like carbon nanotubes (CNTs) [25], graphene [24] and fullerenes[26], metal-based materials such as inorganic metallic nanoparticles of Au, Ag, Co, Ni, Cu, Ru and Mo [27,28] and metal oxides of TiO_2, MnO_2, V_2O_5, SnO_2, CeO_2 and MoO_3 [29–34], dendrimers, selenides ($MoSe_2$) [35] and quantum dots of metal sulphides [36]. Metal nanoparticles have attracted much attention due to their unique properties associated with their dimensions. The unique and novel properties of the nanoparticles are not only due to their small size but also to their narrow size distribution [37]. Functional nanomaterials have enormous applications with the control on the properties of matter at molecular level by controlling the size, shape, structure and morphology[24]. They have unique and remarkable properties such as higher surface to volume ratio, electrochemical stability, high tensile strength, elasticity, electrical conductivity, adsorptivity, capacitance and quantum effects. All these features make them more focused for potential applications in the field of catalysis, surface engineering, electronics, energy storage, sensors, textile, biomedical, medicine (such as drug delivery, diagnosis, cancer treatment and imaging), food, environmental, material science, cosmetics, paints and others[22]. The functional nanomaterials as catalysts and its applications are reported in Fig. 1.3.
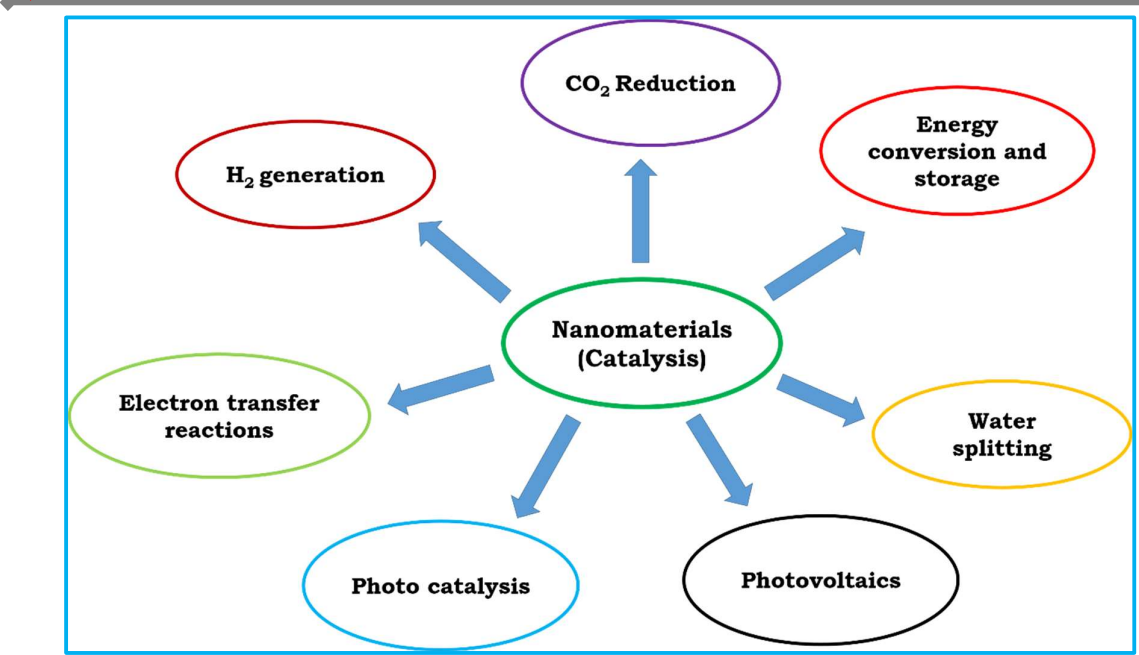
Fig. 1.3. Engineered nanomaterials in different applications.

1.5. Electrocatalysts for DMFC applications

There are numerous catalysts introduced as anode and cathode catalytic materials for DMFC systems. The most common catalysts that have currently been studied are platinum and palladium. Platinum is the most widely employed as electrocatalysts in fuel cell development and has shown good results.

1.5.1. Pt based nanocomposite materials

Plantinum (Pt) is mostly employed as an active metal towards the electrocatalytic applications in the fields of fuel cells. It was observed from the decades, and it is used with different carbon supports as electrocatalysts. The carbon supports which are being employed are Vulcan XC-72, CNT, graphene, etc.

Zeng et al. have prepared the Pt NPs decorated Vulcan XC-72 carbon and studied the electrocatalytic activity towards methanol oxidation reaction (MOR). They have synthesized the colloidal Pt nanoparticles of polyhedra with different shapes by H_2 gas mediated synthesis. They have observed the mass activity of 575 mA mg^{-1}, which was 55 % higher than that observed for Pt/C catalyst, 370 mA mg^{-1} [38]. Mu et al. have studied the controlled deposition of Pt on CNT with the aid of organic molecules as a cross linker and identified that the Pt/CNT electrocatalyst showed an enhanced electrocatalytic activity as well as a better tolerance towards the poisoning intermediate compared to commercial Pt/C in MOR [39].

Huang et al. have described the synthesis of Pt-multiwalled carbon nanotube (Pt/MWNT) nanocomposites with the help of simple soft chemical route in order to avoid the cumbersome acid treatment by introducing only a few defects to the external walls of the NTs. They have observed that PtLM (low-defect MWNTs) exhibited enhanced electrocatalytic activity and excellent CO poisoning tolerance for methanol oxidation, compared to acid treated MWNT (PtAM) electrocatalysts [40]. Li et al. have synthesized the electrocatalysts of graphene nanosheets embedded with Pt nanoclusters with the aid of $NaBH_4$ chemical reduction method. They observed that the peak current density for Pt/graphene electrocatalyst (199.6 mA mg^{-1}) is nearly twice when compared to that for Pt/Vulcan carbon (101.2 mA mg^{-1}) [41].

Choi et al. have deposited Pt nanoparticles (PtNPs) on graphene nanosheets with high metal loading (40–80 wt%), and they specifically used the thermal exfoliated-graphene nanosheets as a functionalized carbon support. The mass activities of the developed Pt/graphene electrocatalysts were observed to be at least twice when compared with conventional Pt/C catalysts [42]. Naidoo et al. have employed solvent free method, wet chemical method and also organo-metallic chemical vapour deposition (OMCVD) technique for the syntheses of PtNPs supported on CNT. They have studied the effect of different metal loading with 20-60 wt%, and they have observed that the Pt/CNT catalysts with 40 wt% metal loading showed the higher electrocatalytic activity when compared to those of other wt% and commercial Pt/C catalysts. They have also observed that the PtRu/CNT catalyst exhibited comparable improvements when compared with commercial PtRu/C electrocatalysts [43].

Huang et al. have synthesized PtCo/MWCNT electrocatalysts by using a soft chemical method without damaging the active sites of MWCNT by solvothermal process. They have observed that PtCo/MWCNT (428.0 mA mg^{-1}) showed the enhanced electrocatalytic activity, which was thrice to that of Pt/MWCNT (145.7 mA mg^{-1}). It showed high durability towards MOR and low poisoning effect caused due to intermediates when compared to Pt/MWCNT [44]. Sun et al. have synthesized PtSn/CNT by surfactant-free aqueous solution method and observed that this electrocatalyst have shown the enhanced electrocatalytic activity in oxygen reduction reaction (ORR) for polymer electrolyte membrane fuel cells (PEMFCs) and methanol oxidation reaction (MOR) for DMFCs and also exhibited high CO tolerance compared with commercial Pt/C catalyst [45].

Ahmadi et al. have synthesized PtCo/S-doped CNT electrocatalysts by impregnation method followed by alloying at 800 ºC under H_2/Ar atmosphere. They have observed that Pt_3Co/CNT electrocatalyst (1302.1 mA mg^{-1}) showed highest MOR activity when compared to Pt/CNT catalysts (971.3 mA mg^{-1}) and commercial Pt/C catalysts (399.3 mA mg^{-1}). It also

exhibited enhanced CO tolerance and long-term durability [46]. Yuan et al. have synthesized PMo/Pt$_x$Ir$_1$/MWCNT (x = 1, 2, 4, 8) (PMo = phosphomolybdic acid) catalysts by polyol reduction method. They have used PMo for functionalizing MWCNT by ultrasonication. They observed that PMo/Pt$_4$Ir$_1$/MWCNT catalysts exhibited high current density (288 mA mg^{-1}), which was 2.5 times higher than that of Pt$_4$Ir$_1$/MWCNT catalysts, and also exhibited high CO tolerance [47].

Zhao et al. have synthesized PtRu/graphene electrocatalyst by low temperature supercritical fluid (SCF) route which is an environmentally friendly method. They have observed that the composite electrocatalyst showed significantly 1.7 times enhanced catalytic activity towards methanol oxidation and also high stability [48]. Lu et al. have synthesized PtPd/rGO catalyst by one-pot hydrothermal method and observed that PtPd/rGO catalyst showed an excellent electrocatalytic activity toward methanol oxidation with enhanced current density and lower onset potential, when compared to unsupported PtPd and commercial Pt/C catalyst [49].

Hu et al. have synthesized PtAu/Graphene by electrodeposition of Pt and Au nano particles on the surface of graphene sheets and showed that PtAu/graphene electrocatalysts showed higher catalytic activity and long-term stability, when compared to Au/graphene and Pt/graphene catalysts for both ORR and MOR. The enhanced activity was observed for the electrocatalyst with Pt:Au molar ratio of 2:1 [50]. Huajie et al. have synthesized PtCo/graphene by deposition of PtCo alloy nanoparticles on to graphene with the help of a facile and reproducible hydrothermal method. PtCo/graphene electrocatalyst exhibited excellent electrocatalytic activity and also enhanced poisoning tolerance, when compared to Pt/graphene, PtCo/MWNTs composites and commercial Pt/C toward MOR [51].

Yang et al. have synthesized PtAu/NG (N-doped graphene) electrocatalyst by microwave assisted synthesis and observed that the electrocatalyst with Pt:Au atomic ratio of 3:1 showed enhanced electrocatalytic activity and stability towards MOR, because of the alloying effect of Pt and Au and due to their synergistic interaction with NG sheets [52].

Yu et al. have synthesized Pt/CeO$_2$-graphene by solvothermal method and observed that CeO$_2$ is capable of assisting as an oxygen buffer in order to alter surface oxygen content of the electrocatalysts and facilitate in improving the catalytic activity toward MOR by removing the intermediate species. The electrocatalytic activity toward methanol electrooxidation enhanced by 1.3 times, the onset potential for ORR shifted by 22 mV towards positive direction, and the long term stability also increased by approximately 2.5 times toward MOR when compared with Pt/G catalyst[53]. Huang et al. have synthesized ternary Pt/MnO$_2$/GS (graphene sheets)

nanocomposites by solvothermal method. They have observed that $Pt/MnO_2/GS$ exhibited high electrocatalytic activity (1224 mA mg^{-1}) towards MOR. The current density was 3.5 times higher than that of Pt/GS (357 mA mg^{-1}) and 5.5 times higher than that of Pt/XC-72 (225 mA mg^{-1}) [54].

Yudai Ito et al. have synthesized PtRu/TECNF (TiO_2-embedded carbon nanofiber) by chemical reduction method. The nanofiber support material was synthesized by electrospinning of polyacrylonitrile with TiO_2 nanoparticles and was subjected to carbonization and steam activation of the nanofibers. Then, the deposition of PtRu nanoparticles was carried out by $NaBH_4$ reduction method, and the optimum Ti/C ratio was observed to be 1. The PtRu/TECNF electrocatalyst showed enhanced electrocatalytic activity towards MOR and exhibited four times higher mass activity when compared to commercial PtRu/C catalyst [55].

Yang et al. have synthesized Pt/Mn_3O_4-CNT composite by solvothermal method and observed that the incorporation of Mn_3O_4 into the matrix of CNT carbon support led to a remarkable increase in the electrocatalytic activity toward MOR in acidic medium and also a long term stability against CO poisoning. Pt/Mn_3O_4-CNT electrocatalyst exhibited nearly two times higher mass activity (970.2 mA mg^{-1}) when compared to Pt/CNT (544.9 mA mg^{-1}) and commercial PtRu/C (420.9 mA mg^{-1}) catalysts[56].

Qian et al. have synthesized carbon-supported bimetallic PtNi electrocatalysts with different Pt/Ni atomic ratios through a polyol method and observed an enhanced electrocatalytic activity by Pt_mNi_n/C electrocatalysts compared to Pt/C as well as a higher power density in direct methanol fuel cell test with Pt_3Ni_1/C as the anode catalyst[57].

Table 1.4. Electrocatalytic performances of different types of Pt based anode catalysts toward methanol oxidation reactions.

Catalyst	Synthesis method	Testing conditions Electrolyte	CH$_3$OH	Specific/mass activity	Ref.
Pt/C	Polyol	0.5 M H$_2$SO$_4$, 20 mV s^{-1}	1 M	575 mA mg^{-1}	[38]
PtNi/C	Hydrogen gas reduction	1 M NaOH, 50 mV s^{-1}	1 M	48.5 mA cm^{-2}	[57]
Pt/CNT	Polyol	1 M H$_2$SO$_4$, 20 mV s^{-1}	2 M	47.4 mA cm^{-2}	[40]
Pt/graphene	Chemical reduction	0.5 M H$_2$SO$_4$, 50 mV s^{-1}	1 M	199.6 mA mg^{-1}	[41]
PtRu/CNT	Organo-metallic chemical vapour deposition (OMCVD)	0.5 M H$_2$SO$_4$, 50 mV s^{-1}	0.5 M	205 mA cm^{-2}	[43]
PtCo/CNT	Chemical reduction	1 M H$_2$SO$_4$, 50 mV s^{-1}	2 M	428.0 mA mg^{-1}	[44]
PtSn/CNT	Thermal evaporation	0.5 M H$_2$SO$_4$, 50 mV s^{-1}	1 M	91.0 mA mg^{-1}	[45]
PtCo/CNT	Impregnation	0.5 M H$_2$SO$_4$, 20 mV s^{-1}	1 M	1302.1 mA mg^{-1}	[46]
PtIr/CNT	Solvothermal	0.5 M H$_2$SO$_4$, 50 mV s^{-1}	0.5 M	311 mA mg^{-1}	[47]
PtRu/graphene	Supercritical fluid (SCF)	0.5 M H$_2$SO$_4$, 50 mV s^{-1}	1 M	205.7 mA mg^{-1}	[48]
PtPd/graphene	Hydrothermal method	0.1 M HClO$_4$, 50 mV s^{-1}	1.0 M	198 mA mg^{-1}	[49]
PtAu/graphene	Electrodeposition	0.5 M H$_2$SO$_4$, 50 mV s^{-1}	0.5 M	394 mA mg^{-1}	[50]
PtCo/graphene	Chemical reduction	1 M H$_2$SO$_4$, 20 mV s^{-1}	2 M	35.8 mA cm^{-2}	[51]
PtAu/graphene	Microwave	0.5 M H$_2$SO$_4$, 50 mV s^{-1}	0.5 M	417 mA mg^{-1}	[52]
Pt/CeO$_2$/graphene	Polyol	0.5 M H$_2$SO$_4$, 50 mV s^{-1}	1 M	440 mA mg^{-1}	[53]
Pt/MnO$_2$/graphene	Polyol	1 M H$_2$SO$_4$, 20 mV s^{-1}	2 M	1224 mA mg^{-1}	[54]
PtRu/TiO$_2$/CNF	Chemical reduction	0.5 M H$_2$SO$_4$, 20 mV s^{-1}	2 M	516 mA mg^{-1}	[55]
Pt/Mn$_3$O$_4$-CNT	Solvothermal	0.5 M H$_2$SO$_4$, 50 mV s^{-1}	1 M	970 mA mg^{-1}	[56].

1.5.2. Pd based nanocomposite materials

Palladium is the second most widely employed metal as an active catalytic material towards the electrocatalytic application in the fields of fuel cells in order to replace Pt, because of the depletion of Pt reserves and also due to its high cost. As the palladium is four times more abundant than Pt and also exhibits the electrocatalytic activity similar to Pt electrocatalysts. The efficiency of methanol oxidation reaction (MOR) highly relies up on the performance of the anode electrocatalysts in terms of enhanced electrocatalytic activity, improved poison tolerance and consistent stability.

1.5.2.1. Pd based electrocatalysts with carbon as solid support

Zhang et al. have synthesized Pd/C composite by microwave-assisted ionic liquid method and observed that the Pd/C electrocatalyst showed excellent electrocatalytic activity for MOR and long-term cycle stability[58]. Chenyao Hu et al. have synthesized Pd nanoparticles supported on Vulcan XC-72 carbon through a chemical reduction method without the use of any surfactant and cumbersome heating process, and the synthesized Pd/CB electrocatalyst exhibited 2.5 times higher electrochemical active surface area (EASA) compared to that of commercial Pd/C and also enhanced current density (1451 mA mg^{-1}), electrical conductivity and excellent long-term stability toward MOR [59].

Liu et al. have synthesized PdNi nanoparticles supported on Vulcan XC-72 carbon by a chemical reduction, and the PdNi/C catalyst exhibited lower onset potential, higher peak current density and better electrocatalytic activity than Pd/C catalyst [60]. Wanga Yi et al. have synthesized Pd/C and PdCo/C catalysts through a simple simultaneous sodium borohydride reduction method in aqueous solution, and the synthesized PdCo(8:1)/C electrocatalyst exhibited enhanced current density and higher tolerance towards CO poisoning[61].

Zhen Yin et al. have synthesized PdAg/C electrocatalysts with the aid of emulsion-assisted ethylene glycol (EG) method. The formation of PdAg nanoparticles occurred through a two-stage growth process, primarily associated with nucleation, growth of the primary nanoclusters, followed by the formation of the secondary nanoparticles with the selection of size process via the aggregation or combination of the primary nanoclusters. It was observed that $Pd_{80}Ag_{20}$/C exhibited distinctly enhanced current density (691.6 mA mg^{-1}) toward methanol oxidation, when compared to Pd/C (210.5 mA mg^{-1}) and commercial Pt/C (689.3 mA mg^{-1}) electrocatalysts [62].

Kaustab Mandala et al. have synthesized PdCu nanoparticles with the aid of a facile room temperature based soft chemical-route by templating Pd^{2+} and Cu^{2+} with ethylenediaminetetraacetic acid (EDTA) followed by controlled chemical reduction of metal-EDTA complex with hydrazine without any inert atmosphere. They observed that PdCu (3:1)/C electrocatalyst exhibited enhanced current density (659.4 mA mg^{-1}) and long term stability toward methanol oxidation, when compared to Pd/C electrocatalyst[63]. Jurzinsky et al. have synthesized the carbon supported Pd_XRh electrocatalysts by wet chemical reduction method and compared with Pd/C and commercially available Pt/C electrocatalysts. It was observed that Pd_3Rh/C electrocatalyst showed enhanced current density (955.7 mA mg^{-1}) as well as long term stability, when compared to Pd/C (543.8 mA mg^{-1}) and Pt/C (669.9 mA mg^{-1}) electrocatalysts toward methanol oxidation [64].

Zhen Yin et al. have prepared PdAu nanoparticles by emulsion assisted synthetic methodology with controlled composition by the help of ternary metal precursors along with surfactants of oleic acid and oleylamine. They have observed that $Pd_{30}Au_{70}$ nanoparticles with significantly low Pd content showed remarkably enhanced current density (950.6 mA mg^{-1}) and long term stability toward methanol oxidation, when compared to Pd/C (210.5 mA mg^{-1}) and commercial Pt/C (689.3 mA mg^{-1}) catalysts [65]. Fathirad F et al. have synthesized carbon supported Pd and PdMo composites with different Pd:Mo atomic ratios by a simple hydrothermal synthesis route, and observed that Pd_3Mo/C electrocatalyst exhibited excellent electrocatalytic activity, current density (71.2 mA cm^{-2}), high durability and stability toward methanol oxidation, when compared to Pd/C electrocatalyst (22 mA cm^{-2}) [66].

Solis-Tobias et al. have synthesized $Pd-CeO_2$/C electrocatalysts by chemical reduction employing two different types of CeO_2, and it was observed that the insertion of CeO_2 into the catalysts enhanced the electrocatalytic activity, long term stability and CO tolerance towards MOR. $Pd-CeO_2$/C electrocatalyst showed enhanced current density (2444 mA mg^{-1}), when compared to Pd/C (784 mA mg^{-1}) electrocatalyst [67]. Jiaxin Li et al. have synthesized the carbon supported $Pd-Y_2O_3$ electrocatalyst by microwave-assisted ethylene glycol reduction method, and the strong electronic effect originated from the interaction of Pd and Y_2O_3 have mostly contributed for the enhanced performance and higher anti-poisoning ability. $Pd-Y_2O_3$/C showed an enormously increased current density (145 mA cm^{-2}) with 20 wt.% Y_2O_3, when compared to Pd/C (60 mA cm^{-2}) electrocatalyst [68]. Kai-Hang Ye et al. have synthesized the carbon supported Pd based electrocatalysts with different metal oxides like Co_3O_4, CeO_2, Mn_3O_4 and NiO by chemical reduction method. It was observed that the current densities for the synthesized electrocatalysts were found to be 74.4 mA cm^{-2} for Pd-NiO/C > 65.1 mA cm^{-2} for

Pd–Co$_3$O$_4$/C > 46.2 mA cm^{-2} for Pd-Mn$_3$O$_4$/C > 36.6 mA cm^{-2} for Pd-CeO$_2$/C > 14.4 mA cm^{-2} for Pd/C electrocatalysts [29].

Table 1.5. Electrocatalytic performances of Pd based anode catalysts with carbon support toward methanol oxidation reaction.

Catalyst	Synthesis method	Testing conditions		Specific/mass activity	Ref
		Electrolyte	CH$_3$OH		
Pd/CB	Chemical reduction	1 M NaOH, 50 mV s^{-1}	1 M	1451 mA mg^{-1}	[59].
Pd$_{80}$Ag$_{20}$/C	Solvothermal	1 M KOH, 50 mV s^{-1}	1 M	691.6 mA mg^{-1}	[62]
PdCu (3:1)/C	Chemical reduction	1 M NaOH, 50 mV s^{-1}	0.5 M	659.4 mA mg^{-1}	[63]
Pd$_{30}$Au$_{70}$/C	Emulsion assisted synthetic methodology	1 M KOH, 50 mV s^{-1}	1 M	950.6 mA mg^{-1}	[65]
Pd$_3$Rh/C	Wet chemical reduction	0.5 M KOH, 20 mV s^{-1}	0.5 M	955.7 mA mg^{-1}	[64]
Pd$_3$Mo/C	Hydrothermal	1 M NaOH, 10 mV s^{-1}	1 M	71.2 mA cm^{-2}	[66]
Pd-CeO$_2$/C	Chemical reduction	0.5 M KOH, 20 mV s^{-1}	0.5 M	2444 mA mg^{-1}	[67]
Pd-Y$_2$O$_3$/C	Microwave-assisted ethylene glycol reduction	0.5 M KOH, 20 mV s^{-1}	1 M	145 mA cm^{-2}	[68]
Pd/C	Chemical reduction	1 M KOH, 50 mV s^{-1}	1 M	14.4 mA cm^{-2}	[29]
Pd-NiO/C	Chemical reduction	1 M KOH, 50 mV s^{-1}	1 M	74.4 mA cm^{-2}	[29]
Pd-CeO$_2$/C	Chemical reduction	1 M KOH, 50 mV s^{-1}	1 M	36.6 mA cm^{-2}	[29]
Pd-Co$_3$O$_4$/C	Chemical reduction	1 M KOH, 50 mV s^{-1}	1 M	65.1 mA cm^{-2}	[29]
Pd-Mn$_3$O$_4$/C	Chemical reduction	1 M KOH, 50 mV s^{-1}	1 M	46.2 mA cm^{-2}	[29]
Pd/Co-CeO$_2$/C	Microwave-assisted ethylene glycol reduction	1 M KOH, 50 mV s^{-1}	1 M	2418.5 mA mg^{-1}	[69]

1.5.2.2. Pd based electrocatalysts with CNT as solid support

Carbon nanotubes (CNTs) have attracted great interest as catalyst supports for fuel cells because of their unique electrical and structural properties. CNTs have been investigated in detail because of their excellent properties such as high mechanical strength, ability to be synthesized as nanowires of a few hundred micrometers length, long tubular geometry,

chemically inert behaviour and high electrical conductivity. They are used as an ideal catalyst carrier and support material for loading noble and non-noble metal nanoparticles in various catalytic applications. However, realistic applications have been hindered by the difficulties associated with processing. Therefore, to obtain the homogeneously dispersed nanoparticles, the surface of CNTs must be modified through the functionalization process. This can be achieved either by covalent or by non-covalent functionalization methods.

Zhi-Peng Sun et al. have synthesized Pd/S-MWCNTs electrocatalysts by chemical reduction method and observed that Pd/S-MWCNTs catalyst exhibited higher current density (19.01 mA cm^{-2}), enhanced CO tolerance and better stability toward methanol oxidation, when compared to Pd/P-MWCNTs (8.75 mA cm^{-2}) and Pd/F-MWCNTs (14.91 mA cm^{-2}) electrocatalysts [70]

Yanchun Zhao et al. have synthesized Pd/APZ-MWCNTs electrocatalysts by chemical reduction method with Pd nanoparticles supported on 2-aminophenoxazin-3-one (APZ) functionalized MWCNT (APZ-MWCNTs). It was observed that Pd/APZ-MWCNTs electrocatalyst exhibited enhanced current density (579.2 mA mg^{-1}), electroactive surface area, long-term stability and high CO tolerance ability towards MOR, when compared to Pd/AO-MWCNTs (398.2 mA mg^{-1}) and Pd/C (323.4 mA mg^{-1}) electrocatalysts [71].

Abolghasemi Fard et al. have synthesized Pd nanoflowers (NFs) by a facile electrochemical deposition method on a polypyrrole@MWCNTs (PPy@MWCNTs) support, and it was observed that the mass activity of Pd NFs/PPy@MWCNTs (725 mA mg^{-1}) is 8.1 times higher than that of Pd NFs catalyst (89.6 mA mg^{-1}) and similarly higher electroactive surface area, long-term stability, high CO tolerance toward methanol oxidation [72]. Yanchun Zhao et al. have synthesized Ni@Pd core-shell nanoparticles supported on MWCNT (Ni@Pd/MWCNT) electrocatalysts by chemical reduction method with an aid of SDS (sodium dodecyl sulfate) as surfactant, and the synthesized Ni@Pd/MWCNT exhibited enhanced current density (770.7 mA mg^{-1}), electrocatalytic activity and stability toward methanol oxidation, when compared to PdNi/MWCNTs (482.2 mA mg^{-1}) and Pd/MWCNTs (315.1 mA mg^{-1}) electrocatalysts [73].

Kakati et al. have synthesized Pd@Mo/MWCNT electrocatalysts by hydrothermal method at different pH, and it was observed that the synthesized Mo@Pd/MWCNT electrocatalyst exhibited enhanced current density (395.61 mA mg^{-1}), long-term stability and high poisoning tolerance toward methanol oxidation, when compared to Pd/MWCNT (230.15 mA mg^{-1}) electrocatalyst [74]. Satyanarayana et al. have synthesized PdAu/CNT electrocatalysts by microwave assisted ethylene glycol reduction method, and they have observed enhanced

current densities, long-term stability and high CO tolerance towards methanol oxidation, with the incorporation of Ag nanoparticle by decreasing Pd content with CNT as carbon support. It was observed that $Pd_{10}Ag_{10}$/CNT electrocatalyst exhibited high current density (731 mA mg^{-1}) than Pd/CNT (408 mA mg^{-1}) electrocatalyst [75].

Yanchun Zhao et al. have synthesized Pd-MnO$_2$/MWCNTs electrocatalyst by chemical reduction method, and the synthesized Pd-MnO$_2$/MWCNTs exhibited higher current density (431.02 mA mg^{-1}) and stability toward methanol oxidation, when compared to Pd/MWCNTs (288.65 mA mg^{-1}) and Pd/C (205.41 mA mg^{-1}) electrocatalysts [76]. Yanbiao Ren et al. have synthesized Pd-SnO$_2$/MWCNTs electrocatalysts by microwave (MW)-assisted polyol reduction, and the synthesized Pd-SnO$_2$/MWCNTs catalyst exhibited enhanced current density (778.8 mA mg^{-1}), long-term stability and high poisoning tolerance toward methanol oxidation, when compared to Pd/C (414.2 mA mg^{-1}) and Pd-SnO$_2$/C (566.7 mA mg^{-1}) electrocatalysts [77].

Table 1.6. Electrocatalytic performances of Pd based anode catalysts with carbon nanotube as support toward methanol oxidation reactions.

Catalyst	Synthesis method	Testing conditions		Specific/mass activity	Ref.
		Electrolyte	CH$_3$OH		
Pd/S-MWCNTs	Chemical reduction	0.5 M KOH, 5 mV s^{-1}	1 M	19.01 mA cm^{-2}	[70]
Pd/APZ-MWCNTs	Chemical reduction	0.5 M NaOH, 50 mV s^{-1}	1 M	579.2 mA mg^{-1}	[71]
Pd NFs/ PPy@MWCNTs	Electrochemical deposition method	0.5 M KOH, 100 mV s^{-1}	1 M	725 mA mg^{-1}	[72]
Ni@Pd/MWCNTs	Chemical reduction	0.5 M NaOH, 50 mV s^{-1}	1 M	770.7 mA mg^{-1}	[73]
Pd@Mo/MWCNT	Hydrothermal reduction	1 M KOH, 50 mV s^{-1}	1 M	395.61 mA mg^{-1}	[74]
Pd$_{10}$Ag$_{10}$/CNT	Microwave assisted ethylene glycol reduction	1 M KOH, 50 mV s^{-1}	0.5 M	731 mA mg^{-1}	[75]
Pd-MnO$_2$/MWCNTs	Chemical reduction	0.5 M NaOH, 50 mV s^{-1}	1 M	431.02 mA mg^{-1}	[76]
Pd-SnO$_2$/MWCNTs	Microwave - assisted polyol reduction	1 M KOH, 20 mV s^{-1}	1 M	778.8 mA mg^{-1}	[77]
Pd-P/PCNTs	Chemical reduction	0.5 M NaOH, 50 mV s^{-1}	1 M	772.67 mA mg^{-1}	[78]
PdCuSn/CNT	Chemical reduction	1 M KOH, 50 mV s^{-1}	0.5 M	395.94 mA mg^{-1}	[79]

Xie et al. have synthesized Pd-P/PCNTs and Pd-P/OCNTs by chemical reduction method by employing phosphorous oxide incorporated carbon nanotubes (PCNTs) and nitric acid treated carbon nanotubes (OCNTs) as carbon supports, respectively. It was observed that

Pd-P/PCNTs catalyst exhibited high current density (772.67 mA mg^{-1}) and long-term stability toward methanol oxidation, when compared to Pd-P/OCNTs (533.51 mA mg^{-1}) electrocatalyst [78].

Zhu et al. have synthesized PdCuSn/CNT electrocatalysts by chemical reduction with NaBH$_4$ as reducing agent, and the co-alloying of Pd with Cu and Sn introduced an enhanced electrocatalytic activity. High tolerance, long-term stability and high current density were observed for PdCuSn/CNT electrocatalyst (395.94 mA mg^{-1}) when compared with binary PdCu/CNT (360.42 mA mg^{-1}), PdSn/CNT (350.03 mA mg^{-1}) and Pd/CNT (274.49 mA mg^{-1}) electrocatalysts [79].

1.5.2.3. Pd based electrocatalysts with graphene as solid support

Graphene, 2D nanostructure, has an atomic layer of carbon in the form of a sp^2 hybridized chemically bonded hexagonal nanostructure. Graphene has the characteristics of the precursor graphite. The articulate structure of graphene enables the control on the catalytic operation into a pathway that would facilitate in enhancing the electrochemical kinetics when employed as an electrocatalyst or support loaded with nanomaterials. Graphene as an electrocatalyst support has contributed towards enhancing the durability and electrocatalytic activity. In particular, the huge possible surface area, conductivity, selectivity, stability, catalytic activity and tunable properties of graphene and graphene-based electrocatalysts towards methanol oxidation reaction have produced significant interest.

Yanchun Zhao et al. have synthesized Pd/PPy-graphene electrocatalyst by chemical reduction method using polypyrrole-functionalized graphene (PPy-graphene) as the catalyst support. It was observed that Pd/PPy–graphene electrocatalyst exhibited higher electrocatalytic activity (359.8 mA mg^{-1}) and long-term stability toward methanol oxidation, when compared to Pd/graphene (265.8 mA mg^{-1}) and Pd/C (205.3 mA mg^{-1}) electrocatalysts [80]. Huang et al. have synthesized Pd/low-defect graphene (Pd/LDG) electrocatalyst by solvothermal method, and the synthesized Pd/LDG exhibited excellent electrocatalytic activity (27.6 mA cm^{-2}) and stability toward methanol oxidation, far outperforming compared to Pd/CNT (11.6 mA cm^{-2}), Pd/rGO (15.0 mA cm^{-2}) and Pd/C (7.3 mA cm^{-2}) electrocatalysts [81].

Ng et al. have synthesized Pd/rGO$_{guanine}$ catalyst by microwave assisted method with the help of guanine functionalized reduced graphene oxide, and it was observed that Pd/rGO$_{guanine}$ electrocatalyst showed an enhanced electrocatalytic activity (1017.42 mA mg^{-1}) and stability towards methanol oxidation, when compared to Pd/rGO (359.80 mA mg^{-1}) catalyst [82]. Lingzhi Li et al. have synthesized bimetallic PdAg nanoparticles supported on reduced graphene oxide with different Pd/Ag ratios on rGO (PdAg/rGO) were prepared by green method without using

any additional reducing or dispersing agents. It was observed that PdAg(1:1)/rGO electrocatalyst exhibited enhanced electrocatalytic activity (630 mA mg^{-1}) and long-term stability towards methanol oxidation with the help of hetero atom insertion, when compared to other electrocatalyst and bare Pd/rGO (311 mA mg^{-1}) electrocatalyst [83].

Zheng et al. have synthesized AuPd@Pd/rGO electrocatalyst by a facile, simple and green wet-chemical method with the aid of 2-[4-(2-hydroxyethyl)-1-piperazinyl]ethanesulfonic acid (HEPES) buffer as a reducing agent as well as a shape directing agent. It was observed that AuPd@Pd/rGO electrocatalyst (69.5 mA cm^{-2}) showed the enhanced electrocatalytic activity and stability towards MOR, when compared to Pd/rGO (65 mA cm^{-2}) and Pd/C (30.3 mA cm^{-2}) electrocatalysts [84]. Awasthi et al. have synthesized 40%Pd–x%Ru (where x = 0, 1, 3, 5, 6 and 10) nanoparticles dispersed on graphene nanosheets (GNS) by microwave-assisted polyol reduction method, and it was observed that 40%Pd–5%Ru/GNS electrocatalyst (118 mA cm^{-2}) exhibited enhanced electrocatalytic activity and stability towards MOR, when compared to other compositions and Pd/GNS (27 mA cm^{-2}) electrocatalyst [85].

Wang et al. have synthesized PdCo bimetallic nanoparticles supported on reduced graphene oxide sheets (PdCo/rGO) by a rapid chemical reduction method using sodium hypophosphite as the reducing agent. The electrocatalysts were synthesized with same loading of Pd whereas varying the initial amount of cobalt precursor and reducing agent proportionally. It was observed that PdCo$_2$/rGO electrocatalyst had exhibited enhanced electrocatalytic activity (320.8 mA mg^{-1}) and long-term stability towards MOR, when compared with other compositions and Pd/rGO electrocatalyst [86]. Na et al. have synthesized PdCu nanoparticles supported on reduced graphene oxide by a two-step solvothermal method with different Pd/Cu ratios, and it was observed that PdCu(1:1)/rGO electrocatalyst exhibited enhanced electrocatalytic activity (1153.4 mA mg^{-1}) and long-term stability towards MOR, when compared to all the other compositions and Pd/rGO (358.5 mA mg^{-1}) electrocatalyst [87].

Zhang et al. have synthesized Ni@Pd/graphene electrocatalyst by a two-step method involving a microwave synthesis step and a replacement step, and it was observed that Ni@Pd/graphene electrocatalyst showed an enhanced current density of 34 mA cm^{-2} towards methanol oxidation in alkaline medium. The performance of the electrocatalysts with different types of alcohols, such as ethanol and isopropanol, were compared [88]. Hsieh et al. have synthesized Pd–Rh nanoparticles supported on reduced graphene oxide sheets by pulse microwave polyol method with different atomic compositions, and it was observed that Pd$_{75}$Rh$_{25}$/rGO electrocatalyst exhibited higher electrocatalytic activity (99.3 mA mg^{-1}) and

stability towards methanol oxidation, when compared to the other composites and Pd/rGO (72.4 mA mg^{-1}) electrocatalyst [89].

Cui et al. have synthesized porous bimetallic PdCu nanofingers supported on graphene by chemical reduction method with varying Pd/Cu ratios, and it was observed that Pd$_7$Cu$_3$/rGO electrocatalyst exhibited high current density (2025.6 mA mg^{-1}) and long-term stability towards methanol oxidation by the synergetic effect of the heteroatom, when compared to the other composites and Pd/rGO electrocatalyst [90]. Ji et al. have synthesized the binary PdM (M = Co, Ni, Cu) electrocatalysts by sodium borohydride reduction under the existence of polyethylene glycol (PEG), and the effect of binary metal composition with Pd coexistence was analyzed. The observed electrocatalytic current density and long-term stability towards methanol oxidation reaction are in the order of PdCo/rGO, PdNi/rGO, PdCu/rGO, Pd/rGO and Pd/C electrocatalysts with the current density of 1004.1, 1092.5, 911.3, 400.0 and 142.7 mA mg^{-1}, respectively [91].

Huang et al. have synthesized Pd/MnO$_2$ nanolamella–graphene sheets (Pd/MNL/GS) electrocatalyst by ethylene glycol assisted solvothermal synthesis, and it was observed that Pd/MNL/GS electrocatalyst exhibited enhanced electrocatalytic activity (838 mA mg^{-1}) and long-term stability towards methanol oxidation, when compared to Pd/GS (224 mA mg^{-1}) and Pd/C (138 mA mg^{-1}) electrocatalysts [31]. Hu et al. have synthesized Pd–SnO$_2$/rGO electrocatalyst by chemical reduction method, and it was observed that Pd–SnO$_2$/rGO electrocatalyst had exhibited enhanced current density (1032.8 mA mg^{-1}) and long-term stability towards methanol oxidation, when compared to Pd (48.1 mA mg^{-1}), Pd/rGO (311.6 mA mg^{-1}) and Pd/SnO$_2$ (780.5 mA mg^{-1}) electrocatalysts [92].

Ajay Kumar et al. have synthesized the highly dispersed Pd and Pd-Ru alloy nanoparticles on 10 wt% CoWO$_4$-doped graphene nano sheets, xPd/10 wt% CoWO$_4$-GNS hybrids (where x = 5, 10, 15 and 20 mg), by microwave-assisted polyol reduction. It was observed that 15Pd/10 wt% CoWO$_4$-GNS electrocatalyst exhibited enhanced current density (316.0 mA mg^{-1}) and long-term stability, when compared with the other composite electrocatalysts [93]. Yang et al. have synthesized silica nanosphere supported Pd nanoparticles encapsulated with graphene (Pd/SiO$_2$@rGO) by a two-step reduction method with the aid of hydrothermal treatment. It was observed that the hybrid nanostructure electrocatalyst, Pd/SiO$_2$@rGO, exhibited enhanced current density (1533 mA mg^{-1}) with the incorporation of SiO$_2$@rGO matrix and long-term stability, when compared to Pd/rGO (388 mA mg^{-1}) and Pd/C (734 mA mg^{-1}) electrocatalysts [94]. Yang et al. have synthesized trimetallic Pd-Cu-Co nanoparticles supported on reduced graphene oxide (PdCuCo/rGO) with different molar ratios

of each by facile chemical reduction with $NaBH_4$ as reductant and cetyltrimethylammonium bromide (CTAB) as stabilizer. They have observed that $Pd_{72}Cu_{14}Co_{14}$/rGO electrocatalyst exhibited enhanced current density (1062.52 mA mg^{-1}) and long-term durability towards methanol oxidation, when compared to other different composites and Pd/rGO (391.50 mA mg^{-1}) electrocatalysts [95].

Table 1.7. Electrocatalytic performances of Pd based anode catalysts with graphene support toward methanol oxidation reaction.

Catalyst	Synthesis method	Testing conditions		Specific/mass activity	Ref
		Electrolyte	CH₃OH		
Pd/graphene	Chemical reduction	0.5 M NaOH, 50 mV s⁻¹	1 M	265.8 mA mg⁻¹	[80]
Pd/PPy-graphene	Chemical reduction	0.5 M NaOH, 50 mV s⁻¹	1 M	359.8 mA mg⁻¹	[80]
Pd/LDG	Solvothermal	0.5 M NaOH, 50 mV s⁻¹	1 M	27.6 mA cm⁻²	[81]
Pd/rGO$_{guanine}$	Microwave	1 M KOH, 50 mV s⁻¹	1 M	1017.42 mA mg⁻¹	[82]
PdAg (1:1)/rGO	Thermal treatment	1 M KOH, 50 mV s⁻¹	1 M	630 mA mg⁻¹	[83]
AuPd@Pd/rGO	Chemical reduction	1 M KOH, 50 mV s⁻¹	1 M	69.5 mA cm⁻²	[84]
40%Pd–5%Ru/GNS	Microwave-assisted polyol reduction	1 M KOH, 50 mV s⁻¹	1 M	118 mA cm⁻²	[85]
PdCo*2/rGO	Chemical reduction	1 M KOH, 50 mV s⁻¹	1 M	320.8 mA mg⁻¹	[86]
PdCu(1:1)/rGO	Solvothermal	1 M KOH, 50 mV s⁻¹	1 M	1153.4 mA mg⁻¹	[87]
Ni@Pd/graphene	Microwave	1 M KOH, 50 mV s⁻¹	1 M	34 mA cm⁻²	[88]
Pd₇₅Rh₂₅/rGO	Microwave-assisted polyol reduction	1 M NaOH, 50 mV s⁻¹	1 M	99.3 mA mg⁻¹	[89]
Pd₇Cu₃/rGO	Chemical reduction	1 M KOH, 50 mV s⁻¹	1 M	2025.6 mA mg⁻¹	[90]
PdCo/rGO	Chemical reduction	0.5 M KOH, 50 mV s⁻¹	2 M	1004.1 mA mg⁻¹	[91]
PdNi/rGO	Chemical reduction	0.5 M KOH, 50 mV s⁻¹	2 M	1092.5 mA mg⁻¹	[91]
PdCu/rGO	Chemical reduction	0.5 M KOH, 50 mV s⁻¹	2 M	473.2 mA mg⁻¹	[91]
Pd/MnO₂/GS	Solvothermal	0.5 M NaOH, 50 mV s⁻¹	1 M	838 mA mg⁻¹	[31]
Pd–SnO₂/rGO	Chemical reduction	0.5 M KOH, 50 mV s⁻¹	1 M	1032.8 mA mg⁻¹	[92]
15Pd/10 wt% CoWO₄-GNS	Microwave-assisted polyol reduction	1 M KOH, 50 mV s⁻¹	1 M	316.0 mA mg⁻¹	[93]
Pd/SiO₂@rGO	Hydrothermal reduction	1 M KOH, 50 mV s⁻¹	1 M	1533 mA mg⁻¹	[94]
Pd₇₂Cu₁₄Co₁₄/rGO	Chemical reduction	1 M KOH, 50 mV s⁻¹	1 M	1062.52 mA mg⁻¹	[95]

1.6. Approaches for synthesis of metal nanoparticles

Metal nanoparticles are presently under extensive research investigations and are having applications in a wide variety of fields such as energy storage, magnetic resonance imaging, gas sensors, optoelectronics and biomedicine. High surface area is required (surface area to volume ratio is high (S/V)) to enhance catalysis in heterogeneous reactions and is resulted by more edges and corners and low coordination number. In catalysis, this ratio determines the development of cost effective metal nanoparticles, which are chemically reactive, catalytically active and robust to increase the reaction rate [96,97].

There are two basic approaches commonly used to prepare the nanoparticles: the "top down approach" and the "bottom up approach", as shown in Fig. 1.4. The top down approach employs physical methods such as ball milling or attrition, whereas the bottom up approach employs solution based chemical synthetic procedures. By applying top down approaches, large production of nanoparticles can be achieved, however it is very difficult to produce uniform particle size and also difficult to manipulate the particle size with the top down approach [98–100]. Physical methods always come under the top down approach and widely operate at high energy radiations, applying high mechanical pressure, electrical energy and thermal energy towards generating the nanoparticles by using material abrasion, melting, attrition, pyrolysis, ball milling, condensation or evaporation [100,101]. The main advantage of the approach is no contamination of solvent. This approach is less economical because abundant waste is produced during the synthesis. The most commonly employed physical methods to produce the nanoparticles are physical vapour deposition (PVD), laser ablation, high energy ball milling, inert gas condensation, flash spray pyrolysis, laser pyrolysis, electrospraying and melt mixing[101].

The bottom up approach represented as powerful tool to synthesize well defined and uniform size nanoparticles with controlled size. This approach is involving in the coalescence or accumulating of atoms and molecules to generate diverse range of nanoparticles. Most of the chemical methods come under the bottom up approaches, whereas the nanoparticles are formed by self-assembling of monomer/polymer molecules, precipitation, pyrolysis, deposition and spraying methods. These chemical or solution based synthetic approaches used for synthesizing the multifunctional, well-defined crystallographic, facet directed electrocatalysts have been generating nanomaterials with superior, controlled and selective electrocatalytic activity. Subsequently, the solution based "bottom up" synthesis methods offering accuracy in the design of the desired structural properties of electrocatalysts such as size, shape, composition and controlled growth [98–100]. The modification of key reaction parameters is very simple by

utilizing the solution based synthetic approaches to synthesize the nanoparticles, which can lead to the creation of high index facets performing enhanced chemical and thermal stability under both oxidising and reducing conditions, as well as at high temperatures. Therefore, the high index Pt-based nanoparticles are predicted to present the outstanding catalytic activity and selectivity even in severe acidic reaction conditions, executing them as good electrocatalysts for fuel cell applications. The most common bottom up approach or chemical methods used for the synthesis of nanoparticles are sol-gel method, hydrothermal synthesis, microemulsion technique, chemical vapour synthesis, polyol synthesis and plasma enhanced chemical vapour deposition (CVD) technique [100,102].
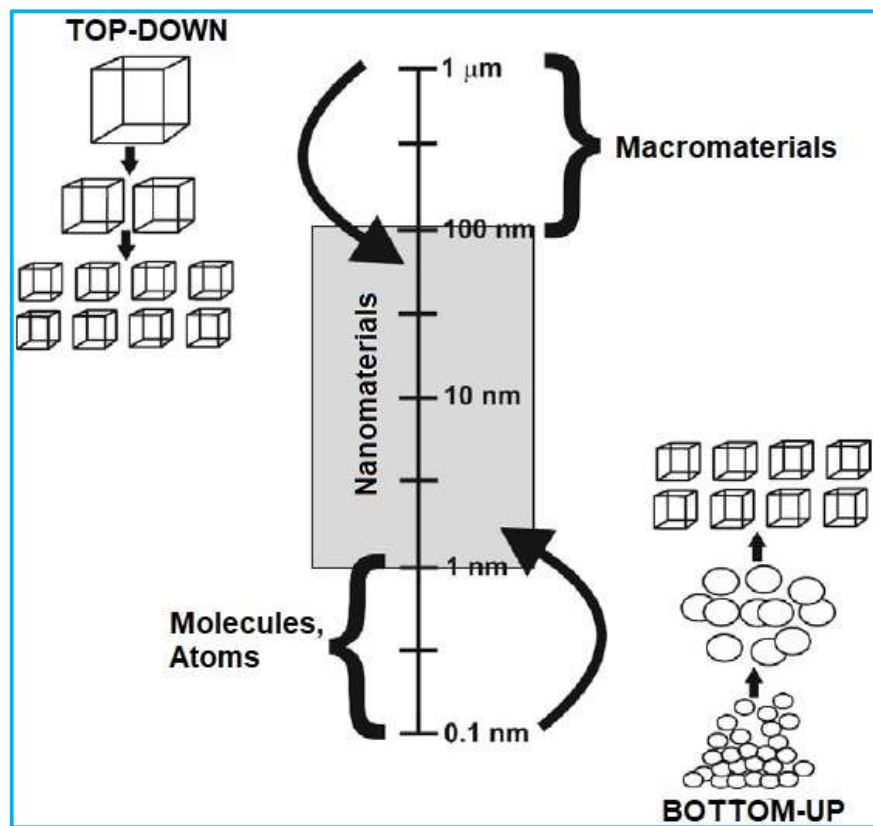
Fig. 1.4. Scheme of the two approaches used in the fabrication of nanomaterials: "top down" and "bottom up".

1.7. Methods for synthesis of metal nanoparticles

Metal nanoparticles were synthesized with high quality, accurate size and morphology, required composition and shape, achieving through the manipulation of the synthesis parameters or regulation of the experimental parameters [103]. The research is going on the development of feasible and precise synthetic routes, which would lead to distinctive structural properties of the nanoparticles [104]. There is a need to develop reproducible synthetic routes to prepare Pt-based or Pd-based sole or bimetallic nanoparticles. It is important to understand,

how the second metal influence the selectivity, catalytic activity and stability of the metal nanoparticles [105–107]. The structure of bimetallic nanoparticles depends on the synthetic methods involved in the preparation and distribution of the two distinctive metal atoms such as alloys, aggregates, core-shell, particle-in-particle, particle-on-particle (hetero-structure), separate and super core-shell nanoparticles [18,108].

Recently most of the researchers have essentially focused on control over the morphology and composition of Pt-based nanostructures to improve their stability and electrocatalytic activity as practical methodologies for fuel cell catalysts [109]. Up to the end, several methods have been established in order to control the shape and particle size of Pt-based nanoparticles by means of different preparation methods, for example, polyol method used in aqueous or organic solution with thermal-decomposition process, electrochemical and photochemical reduction techniques [110]. In addition, the synthesis of varied Pt and Pd based nanostructures have been established by controlling the morphology and composition of catalytic nanostructures to understand basically their catalytic activity and performance with their dimensional (D) versatility, such as 0D (cube, octahedron, truncated cube, and icosahedron), 1D (wire and rod), 2D (plate and disk) and 3D nanostructures (star, flower and dendrite) [18,103–110].

In general, synthesis methods for nanoparticles can be divided into physical, chemical and biological methods and also classified into electroless preparation, electrochemical deposition, physical vapour deposition and irradiation assisted methods. Figure 1.5 exhibits the classification of synthesis methods for the preparation of carbon supported metal nanoparticles, which have been briefly described in the following sections.
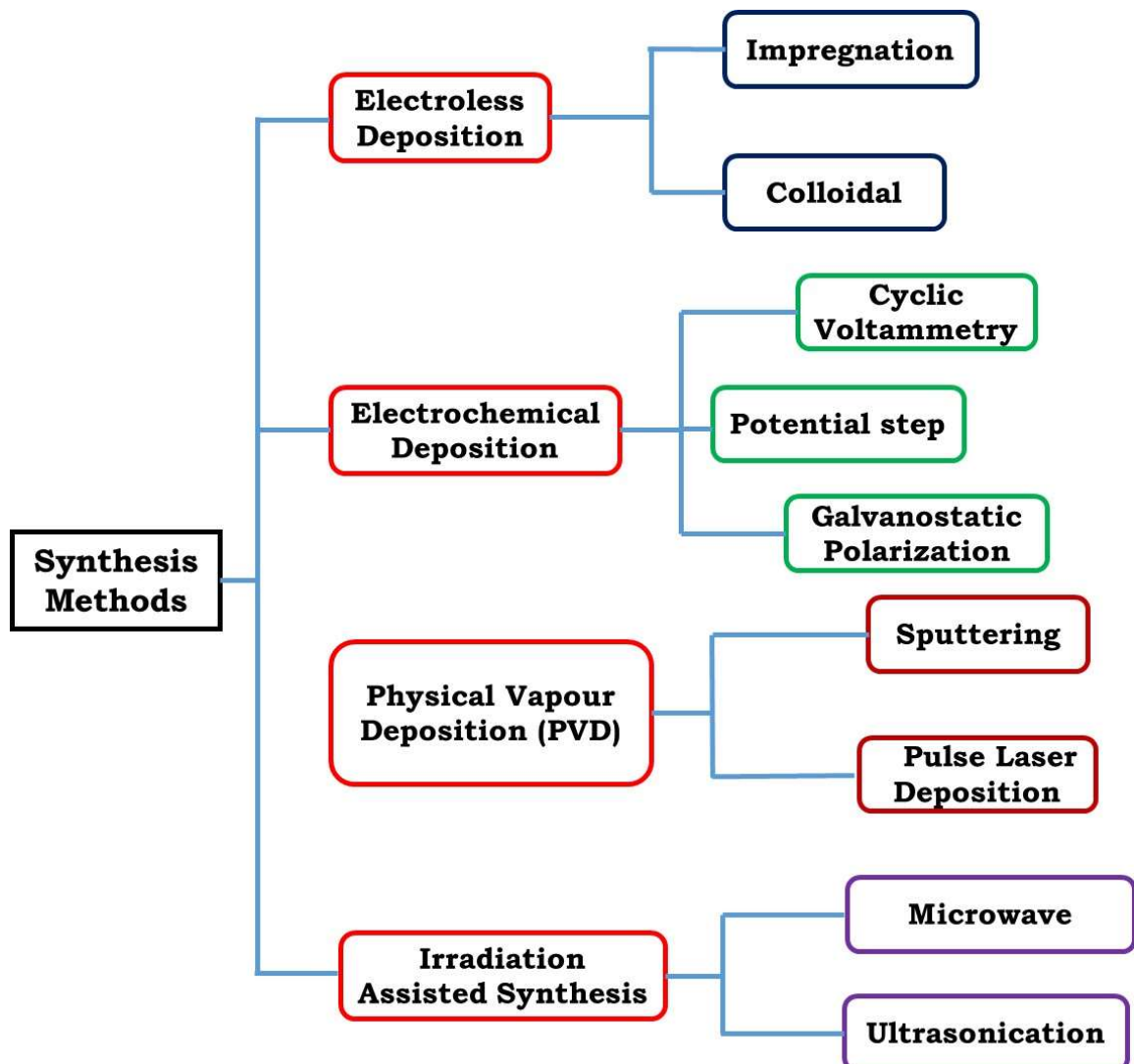
Fig. 1.5. Various synthesis methods for the preparation of different types of carbon supported electrocatalysts.

1.7.1. Electroless deposition methods

Pt and Pd-based nanoparticles are deposited on the carbon substrates, and the deposition on the electrode surface could be possible to develop the electrode surface by electroless deposition/electroless plating technique, which involves spontaneous reduction of metal ions without the use of electric current. The electroless deposition method requires a reducing agent and the reaction is carried out in acidic, basic or neutral aqueous solutions [111–114]. The electroless deposition method is classified into two types: autocatalytic deposition and galvanic displacement. Do et al. have synthesized the Pt/C nanoparticles using electroless deposition method with and without ethylene glycol [115]. Walbart et al. have synthesized partially porous Pt-nanotube networks (NTNWs), which increases the performance of DMFC through increasing the methanol oxidation reduction (MOR) than the commercially available Pt nanoparticles [116].

The autocatalytic deposition method uses the reducing agent (such as $NaBH_4$, N_2H_2, etc.) to reduce the metallic ions in solution and deposition of film can be achieved by oxidation of the chemical compound on the surface. The galvanic displacement is different from the autocatalytic deposition and it does not require any reducing agents, because the base material behaves like a reducing agent. The galvanic displacement takes place when the base material is dissolved and displaced into the solution by the metallic ions in solution, which are reduced on the surface of the base material. Electroless deposition methods include impregnation and colloidal approaches, which are most cost-effective and straight forward techniques[117]. Figure 1.6 explains the preparation procedure of carbon solid supports with impregnated metal nanoparticles using electroless deposition methods.
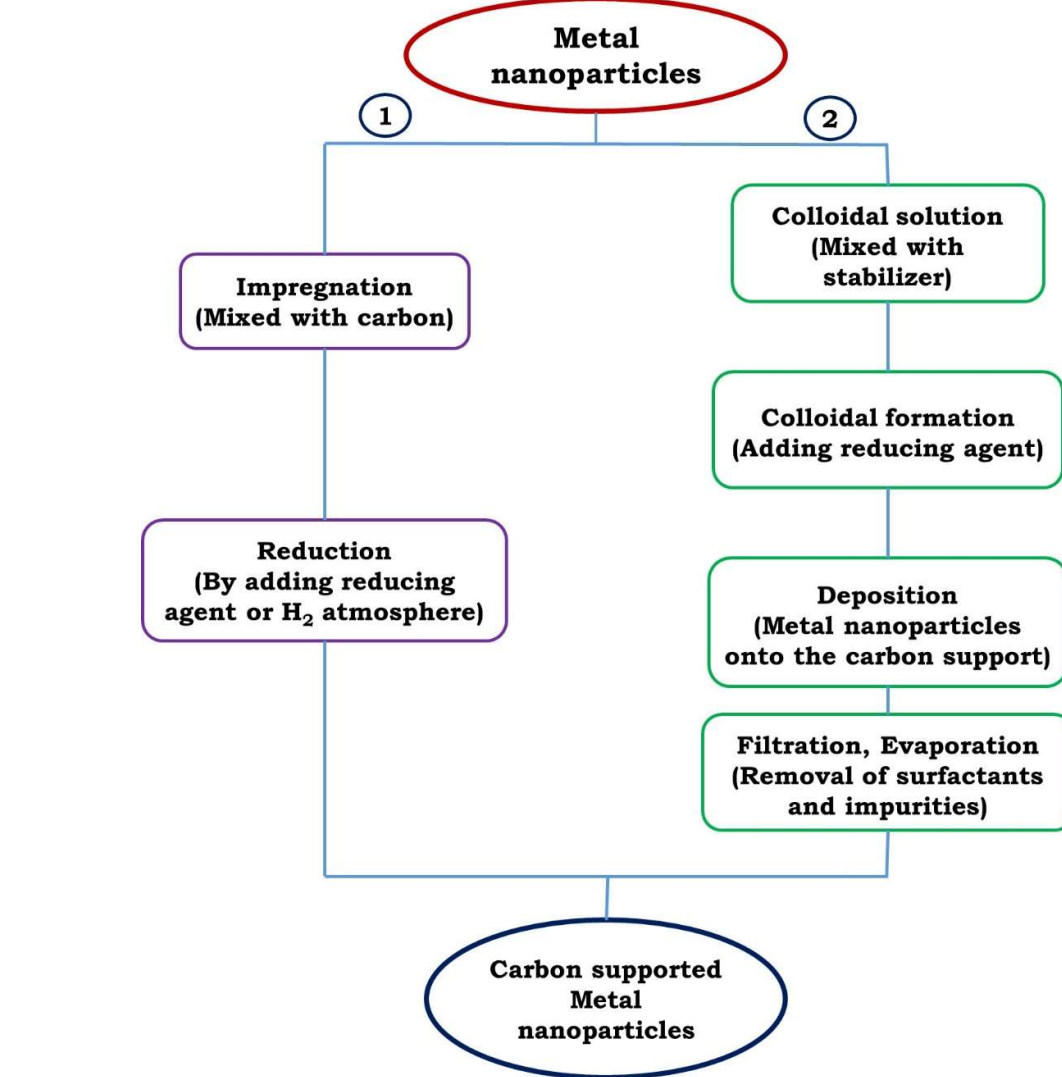
Fig. 1.6. Electroless deposition methods for preparation of carbon supported metal nanoparticles as electrocatalysts by (1) Impregnation method and (2) Colloidal method.

1.7.1.1. Impregnation method

Impregnation method is simple and has been used most commonly for the synthesis of nanoparticles. Pt or other metal ions are deposited onto the carbon support after the reduction of precursors. The metal precursors are dissolved or soaked in the solvents like water and deposited into the pores of support before reducing the metals to metal ions. The chemical reduction of the metal precursor solutions were realized using reducing agents (hydrazine, borohydride and formic acid) or gas phase reduction agents (hydrogen) at high temperatures ($> 3000\ ^0C$) under an inert atmosphere. The particle size depends on the morphology and pore size of the porous substrate, reaction time and mass-transfer kinetics of reducing agent [118]. Zhang et al. prepared three Pt/C cathode catalysts for PEM fuel cell by using impregnation

reduction method [119]. They have compared the effects of the reducing agents, $NaBH_4$, N_2H_4 and HCHO, on the catalytic activity and finalised the order as follows Pt (HCHO) > Pt ($NaBH_4$) > Pt (N_2H_4).

1.7.1.2. Colloidal method

Colloidal methods are most commonly used, easy, cheap and powerful methods for the synthesis of nanoparticles using both organic and inorganic reactants. The metal precursors or salts are homogeneously dispersed in a liquid and reduced to form nano size particles (1 to 200 nm). Agglomeration of the particles is prevented by electrostatic repulsion or the addition of a stabilizing agent, and the particle size depends on the initial concentration of precursor and operating conditions [112]. The carbon supported metal nanoparticles are prepared using different colloidal methods. Colloidal methods have been classified into sol-gel, polyol, microemulsion, solvothermal/hydrothermal methods, etc.

A. Sol-gel method

Sol-gel (solution-gelation) process is a type of colloidal or wet chemical method used to synthesize Pt and Pt-based nanoparticles efficiently and economically. The sol-gel method is used to produce uniform size nanoparticles from their hydrolyzable precursors (like metal alkoxides). These metal alkoxides are subjected to hydrolysis and polycondensation reactions along with the successive drying to form various metal products [120][121]. Kim et al. synthesized Pt-Ru nanoparticles with high EASA, showing good catalytic activity on anode side of the direct methanol fuel cells (DMFCs) [122].

B. Polyol method

Polyol process is a cheapest and simple method to synthesize Pt and Pt-based nanoparticles using polyalcohols (glycols) as reaction medium, which acts as solvent, reducing agent and stabilizing agent [120–123]. In this method, high-boiling point alcohols (such as ethylene glycol (197 ^{0}C), diethylene glycol (244 ^{0}C), glycerol (290 ^{0}C), etc.) are used as the solvents to control the nucleation and particle growth during reaction. Especially, the ethylene glycol has been widely used as the solvent material in the polyol process. Because, it is having a strong reducing capability, relatively high boiling point and high dielectric constant, which increases the solubility of metal salts. On the other hand, some reducing agents such as sodium borohydride ($NaBH_4$), hydrazine (N_2H_4) and formaldehyde (HCHO) and some surfactants/capping agents such as polyvinylpyrrolidone (PVP), cetyltrimethylammonium

bromide (CTAB) and sodium dodecyl sulfate (SDS) are added to control the catalytic activity, which influences the performance of the fuel cell [124–127].

C. Solvothermal/Hydrothermal method

Solvothermal/hydrothermal methods are easy and surfactant free techniques to synthesize Pt and Pt-based nanoparticles at high pressures and temperatures. These techniques are occurred in closed systems, and heterogeneous reactions are involved in these methods. Both methods used different types of precursors for the preparation of nanoparticles. The reacting precursors are insoluble at normal temperature while solubility increases with temperature [113,128–131]. Gemuci et al. have synthesized cubic shaped Pt nanocrystals using dimethylformamide (DMF) as solvent and reducing agent through solvothermal method [132]. They have explored the effect of time, temperature, DMF to water ratio and the type of precursor salt. Ji et al. prepared ultrafine Pt nanoparticles using PVP as capping agent through hydrothermal method [133].

1.7.2. Electrochemical deposition methods

Electrochemical (electro) deposition is a low cost and mass production technique to generate Pt and Pt-based nanoparticles. In this method, the electrons are produced by applying external source, whereas reducing agents are used to produce the electrons in the electroless deposition method. Electrochemical cell is used for the deposition of Pt or Pt-based nanoparticles on the electrode surface as films or layers, either by applying the electrode potential or current density in the electrochemical cell [133]. Kim et al. have synthesized Pt nanoparticles on carbon nanotubes (CNTs) surface using electrochemical deposition method [134]. Electrochemical deposition methods are classified into cyclic voltammetry, potential pulse/step electrodeposition, galvanostatic/potentiostatic polarization, chronoamperometry, chronopotentiometry, electrophoresis and current pulse experiments.

1.7.2.1. Cyclic voltammetry

Another electrodeposition method widely used to synthesize Pt and Pt based nanoparticles is cyclic voltammetry method. In this method, Pt(IV) complex intermediates are generated in the initial stage through the electrochemical deposition. Then, the Pt(IV) complex is reduced to Pt(0) and deposited on the support material by applying the potential. More number of cycling steps increases the uniform dispersion of Pt nanoparticles (2 nm size) on support material which leads to increase the electrocatalytic activity[135,136]. Kheirmand and Eshghi have reported that the Pt nanoparticles were deposited onto rGO/GCE electrode by the cyclic voltammetry deposition method [137].

1.7.2.2. Pulse electrodeposition

Potential pulse electrodeposition is one of the most effective electrodeposition methods for the synthesis of Pt and Pt-based nanomaterials. In this method, potential is applied in a repetitive square wave manner with peak current density, pulse-on time and pulse-off time. The grain size is greatly reduced by pulse-on time and pulse-off time with the application of a very high current density. This means that the nucleation begins and the new grain will form and grow in the pulse-on time, and the grain size reduces to nano level and successively stops the growth of the grain in the pulse-off time [138][139]. Huang et al. have prepared Pt/C electrocatalyst for ORR in PEM fuel cells using pulse electroplating method. They have established that the aggregation of Pt nanoparticles can be overcome, and the catalyst performance can be improved by using this method [140].

1.7.2.3. Galvanostatic/Potentiostatic polarization

Galvanostatic polarization is another type of electrochemical deposition technique to synthesize Pt and Pt based nanoparticles. The single and multiple pulse galvanostatic polarizations are applied in additive and precursor solutions. Then, different pulsed currents were applied for the deposition of nanomaterials on the support material. The parameters such as pH, type and concentration of additive, concentration of precursor, solution temperature, pulse time, relaxation time and pulsed current amplitude were modified to enhance the deposition of nanomaterials on support material [134,138]. Yaldagard et al. synthesized Pt-Co nanoparticles (11.37 nm) using galvanostatic codeposition onto the reduced graphene nanoplates (GNP) on carbon paper (Pt-Co/GNP/GDL) [141–143]. Paoletti et al. electrodeposited Pt nanoparticles on porous and high surface carbon substrates (carbon black and carbon nanotubes) for PEM fuel cells using both single and multiple pulse galvanostatic polarization techniques [144].

1.7.3. Physical Vapour Deposition (PVD)

Physical vapour deposition (PVD) method is a versatile method to synthesize Pt and Pt based nanoparticles. In this method, Pt and Pt based atoms or molecules deposited on the carbon support from a vapour phase. PVD is an eco-friendly deposition technique involving three important steps: (1) vaporization of the material from a solid source, (2) transportation of the vaporized material and (3) nucleation and growth to generate the nanoparticles [111–113,117,120]. Suitable particles size is obtained by maintaining the substrate temperature, particle energy and reactive gas properties in the PVD method. PVD is a dry coating method and having some

advantages such as multicomponent layers, low deposition temperature, high coating density and strong adhesion than the wet coating methods. PVD methods are classified into sputter deposition, electron beam deposition, pulsed laser deposition, vacuum arc deposition and ion plating. Dobrzanski et al. synthesized Pt nanowires using a three-step PVD method. This method involves dispersion/deposition of carbon nanotubes (CNTs) on glass/silicon substrate. Platinum nanoparticles are deposited on CNTs by PVD, and subsequently carbonaceous mass is removed by heating at 700 ^{0}C for 90 min. The deposition thickness (5-20 nm) determines the agglomeration of Pt nanoparticles [145].

1.7.3.1. Sputter deposition

Sputter deposition is a vacuum based PVD method, which has been commonly used to synthesize Pt and Pt based nanoparticles and films. In this deposition, the atoms are ejected from the target by the ion bombardment, and these ejected atoms are deposited on the plated surface and formed a thin film of nanoparticles. Sputter deposition having many advantages such as formation of smooth, dense and continuous films more easily than other deposition methods due to the high energy flux produced that leads to high surface mobility on the substrate surface. Sputter deposition is classified into simple sputtering and magnetron sputtering. The main difference is that the magnetron sputtering consisted of magnets behind the target [111–113,117,120]. Kim et al. developed a new layer with the combination of carbon black (CB) and carbon nanotubes (CNTs), and Pt is sputtered on this new surface [146].

1.7.3.2 Pulsed laser deposition

Pulsed laser deposition (PLD) or laser ablation (LA) is another type of PVD, and it is having a procedure similar to the electron beam deposition (EBD) but operates at high power pulsed laser in place of electron beam. The high power laser pulses initially evaporates the particles from a solid source, draws to hit the target surface leading to melting, evaporation and ionization of the material and finally the materials deposit onto the substrate [113][120]. In this method, the chamber pressure decides the structure and morphology of the synthesized nanoparticles. It is a powerful and useful method and operates at normal conditions, and it can also be combined with other methods such as chemical vapour deposition. The Pt layer thickness and diameter of the Pt nanoparticles increases with increasing the number of pulses [147]. Nguyen et al. synthesized Pt nanoparticles through laser ablation method using Nd:YAG laser in solutions of ethanol and trisodium citrate in water. They have found that the size of the Pt nanoparticles prepared in ethanol (7-9 nm) was less than that prepared with trisodium citrate in water (10-12 nm) [148].

1.7.4. Irradiation assisted synthesis methods

Irradiation assisted techniques are typically simple, economical, eco-friendly and are carried out in short time and at very mild conditions with high reproducibility to synthesize Pt and Pt-based nanoparticles. The main advantage of irradiation technique is the precursor solutions or metal ions are reduced to zerovalent metal atoms or nanoparticles without the addition of any chemical reducing and stabilizing agents [113]. Other advantages of the synthesized nanoparticles are high stability, uniform distribution onto the solid support materials and without the production of unwanted by-products. Enormously, a number of hydrated electrons (e^-), hydrogen $(H^\bullet)$ and hydroxyl $(OH^\bullet)$ radicals are generated during radiolysis of aqueous solutions in the irradiation method. These radicals act as strong reducing agents and reduce the metal ions (M^+) into the zerovalent (M^0) metal particles[149]. The zerovalent nuclei amount can be controlled by altering the dosage of irradiation energy. Recently Chau et al. have synthesized bimetallic Pt-Au and Fe-Pt nanoparticles using high-intensity laser irradiation method [150]. They have reported that the average size of the bimetallic nanoparticles increases with the irradiation time in aqueous solution without the addition of any chemical reducing agent. The irradiation methods are classified into microwave, ultraviolet (UV), gamma (γ) and ultrasonic irradiation methods.

1.7.4.1. Microwave irradiation method

Microwave irradiation or heating is versatile method to synthesize Pt and Pd based nanoparticles. On microwave irradiation in solvents, existed electric dipoles generate an electric field with which the materials respond and friction developed between molecules, which subsequently generate the heat. The heat capacity of the microwave accelerates the reduction of metal precursor and the nucleation rate of crystals [151]. The crystal size of the metal nanoparticles depends on the uniform heating and control over the heating process, which are simplified to the local temperature and concentration gradients, hence encouraging the formation of well distributed nanoparticles on the solid support. The advantages of the microwave heating over the conventional heating are high efficiency, fast heating, shorter crystallization time, no solvent or minimum solvent utilized and eco-friendly nanoparticles [152]. Chen et al. have prepared Pt/C nanoparticles with 3.5 - 4.0 nm diameter with uniform distribution using microwave heating method for methanol fuel cells [153].

1.7.4.2. Ultrasonic irradiation method

Ultrasound reduction method is used to synthesize Pt and Pt based nanoparticles using ultrasonic waves with a frequency of 20-200 kHz in aqueous solutions. Ultrasonic irradiation

system is simple and scalable, and it provides extreme (high temperature, ~5000 ^{0}C and high pressure, ~2000 kPa) conditions. Several designs of ultrasound irradiation devices are available commercially such as ultrasound bath, ultrasound probe sonicator and flow reactors. The sonicator generally contains a power source, a piezoelectric system consisting of electrodes and a bath container for bath sonicator or a probe with a stainless steel neck and a reaction vessel for probe sonicator [154]. Ultrasound is a reason for producing the cavitations, which reduce the chemical precursors dissolved in aqueous solutions. Cavitation initiates the formation of bubble at first stage, growth occurs at second stage and collapse of bubble occurs at the final stage, which liberates enormous energy with the breakage of chemical bond. High strength ultrasound irradiations may increase the precursor reduction rate in the aqueous solution. Recently, Park et al. synthesized titanium carbide (TiC) supported Mn with the inclusion of Pt nanoparticles (Pt(Mn)/TiC) (4-6 nm size) in ethylene glycol with different Pt loadings (without addition of any other additives) for methanol oxidation reduction (MOR) in acidic media [155].

Apart from the above methods, various other following methods are used to synthesize Pt and Pd based nanoparticles for various applications, such as chemical vapour deposition [156], nanocapsule [157], chemical dealloying [157], freeze drying [158], surfactant free strategy [159], capping agent [160], atomic layer deposition [161], surface segregation [162], metal organic chemical fluid deposition (MOCFD) [163], supercritical fluid-chemical vapour deposition (SCF-CVD) [164], carbonyl chemical route [165] and low pressure plasma [166].

1.8 .Techniques for characterization of nanomaterials

Morphology, structure, chemical composition, crystallinity, size, shape, hollow, solid, core-shell structure and surface area of the synthesized materials and their composites are determined by different characterization techniques, which are described hereunder. The detailed explanation and interpretation of the results obtained by the different characterization techniques are discussed in the respective chapters.

1.8.1. Powder X-Ray diffraction (PXRD)

PXRD technique is one of the most versatile techniques used to determine the crystal structure of the materials. It is also employed to know the qualitative and quantitative analysis of solid phases and provides information on the particle size of specific components. PXRD spectrum is obtained by the interaction of high energy X-ray beam with crystalline materials, which satisfies the Bragg's law. Bragg's law is expressed by an equation as follows [167].

$$n\lambda = 2dsin\theta \qquad (1.1)$$

where n = order of diffraction

λ = wavelength of the x-ray beam

d = lattice space constant between the crystal planes

θ = angle of incidence
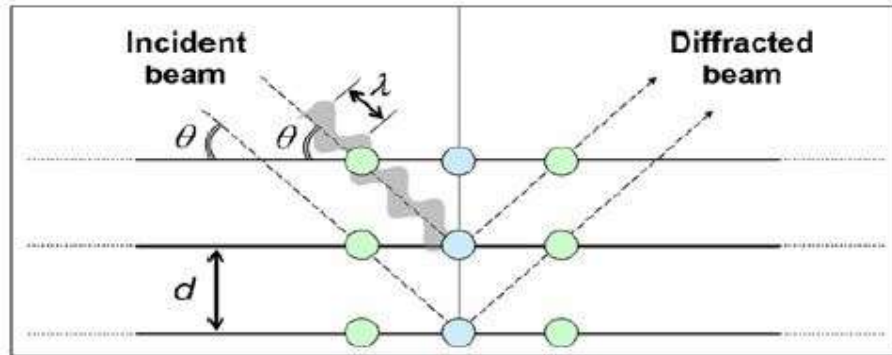
Fig. 1.7. Bragg's Law for X-ray diffraction.

The universal database also known as the Joint Committee on Powder Diffraction Standards (JCPDS) is used to identify the crystal structures of the materials.[168] The JCPDS is a collection of standard XRD patterns, which defines the inter-planar distances of specific crystallographic structures of the materials. In the present study, the X-ray diffraction patterns of synthesized materials were recorded by the XRD instrument, PANalytical Advance, using Cu-Kα (λ=1.54 Å) radiation, and the data are collected in the 2θ range of 10-160°. The grain size can be determined from the broadening of the diffracted beam using the Scherrer's formula:[169]

$$t = \frac{0.9\lambda}{Bcos\theta} \qquad (1.2)$$

where t = diameter of the grain

λ = wavelength of the X-ray beam

θ = diffraction angle

B = full width at half maximum (FWHM) of the diffraction peak.

The B is measured from the broaden peak at FWHM and obtained from Warren's formula:

$$B^2 = B_M^2 - B_S^2 \qquad (1.3)$$

where B_M = FWHM of the sample

B_S = FWHM of a standard sample of grain size of around 2 μm.

1.8.2. Raman spectroscopy

Raman spectroscopy is a powerful technique named after Sir C.V. Raman and useful to identify the chemical and structural properties of the materials. Raman scattering is obtained when a monochromatic light usually a laser light is interacted with the electron cloud of the sample and generates a minuscule measure of Raman scattered light, which is identified as spectra utilizing a charge-coupled detector and camera (Fig. 1.8 (a))[170].

If the energies of the incident and scattered lights are equal, it is named as Rayleigh scattering (elastic scattering). Whereas, if the energy of the scattered light is less than that of the incident light, it is known as Stokes line, and if the energy of the scattered light is higher than that of the incident light, it is known as an anti-Stokes line.[171]. These two types of scattering are Raman active (inelastic scattering), and the peaks in the spectrum are characteristic of the specific material (Fig. 1.8. (b)). The Raman shift is calculated using the following equation:

$$Raman\ shift\ (\Delta_\omega) = \left(\frac{1}{\lambda_0} - \frac{1}{\lambda_1}\right) \qquad (1.4)$$

where λ_0 = excitation wavelength

λ_1 = Raman spectral wavelength

In the present study, Raman spectra were recorded on a Horiba Scientific confocal Raman microscope with the laser power 2-5 mW at 532 nm laser excitation.
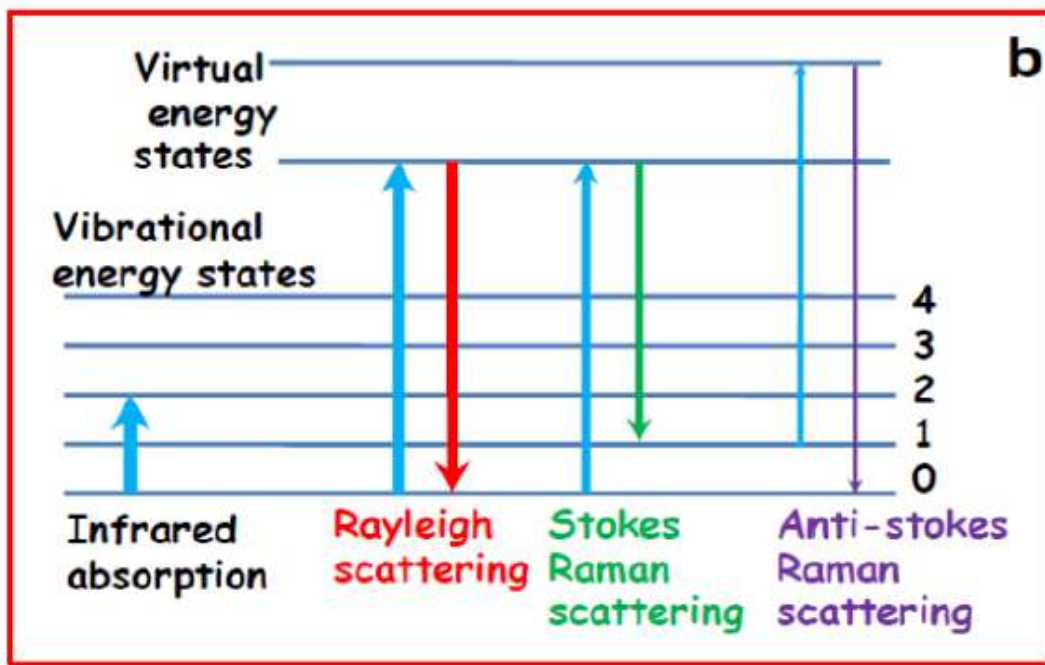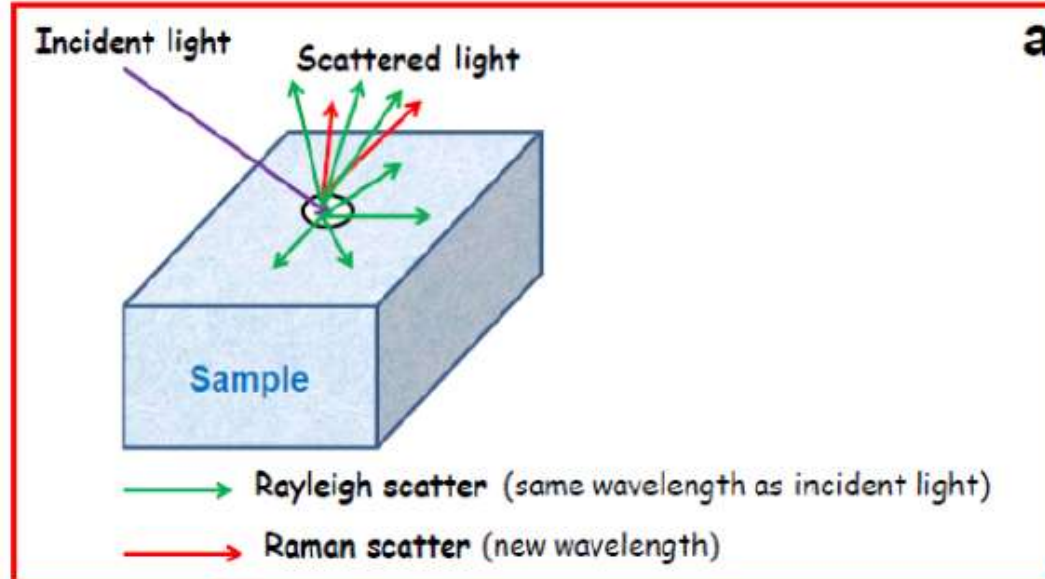
Fig. 1.8. (a) Illustration of incident light scattering, and (b) energy level diagram showing the states involved in the Raman signal.

1.8.3. X-ray photoelectron spectroscopy (XPS)

XPS is a surface analytical technique, also called widely as "Electron Spectroscopy for Chemical Analysis (ESCA)", which is helpful to determine the elemental composition at parts per thousand ranges, chemical and electronic state of the elements that exist in the samples. When a beam of X-ray is irradiated on the sample, the electrons are ejected from the surface and the binding energy of the ejected electrons is calculated by using the equation 1.5.[172]

$$Kinetic\ energy = h\vartheta - BE - \varphi_s \qquad (1.5)$$

where, hυ = energy of the photons

BE = binding energy of an electron

φ_s = work function.

In the present study, the XPS spectra of synthesized materials were recorded on Physical Electronics, PHI 5000 Versa Probe III instrument with monochromatic Al Kα X-ray radiation.

1.8.4. Scanning electron microscopy (SEM)

SEM is a powerful technique that is classified under scanning probe microscopy (SPM); and it uses a focused beam of high energy electrons to give the morphological structure of the compound by scanning.[173]. The electron collision with the atoms on the surface gives several signals that can be observed. It gives information about the orientation of materials making up the sample, sample external morphology and elemental composition. Finally, data is collected over a particular area of the compound, and a 2D image is generated. SEM facilitates the analysis of samples with a resolution down to nanometre scales. In the present study, the morphological characteristics and chemical composition were recorded on a scanning electron microscope (SEM), VEGA3, Tescon, USA integrated with an energy dispersive X-ray spectrometer (EDS).

1.8.5. Field emission Scanning electron microscopy (FE-SEM)

FE-SEM is magnifying instrument equipped with field emitter and emission source. The electron source produces an electron beam at a large and stable current in the small beam, and these electrons are made to incident on the sample in a zig-zag pattern to obtain surface morphological properties of the sample. There are two classes of emission source: thermionic emitter and field-emission source. Emitter type is the main difference between SEM and FE-SEM. In the present study, the morphological characteristics and chemical composition are investigated by field emission scanning electron microscope (FE-SEM, TESCAN-MIRA 3 LMH, 2014 and FEI-Apreo LoVac) integrated with an energy dispersive X-ray spectrometer (EDS).

1.8.6. Transmission electron microscopy (TEM)

TEM is an SPM technique in which an electron beam having the energy of the order of hundreds of KeV is transmitted over an ultra-thin film of a sample, interacting with the sample as it passes through to provide morphological, topographical, compositional and crystallographic information of the sample. An image is obtained from the interaction between electrons and sample; the image has a magnified image captured by a sensor.[174] High-resolution TEM allows the researchers to outlook samples on a molecular level in the order of a few angstroms (10^{-10} m), making it possible to analyze structure and texture at a significantly high resolution. TEM operates nearly on equal basic principles as SEM and both use electron beam source. In the present study, the morphology of the as-synthesized materials was examined by using TEM and high-resolution TEM (HRTEM), FEI Tecnai G^2 transmission electron microscope operated at 200 kV, TEM, JEOL 1010 operated at 100 kV and HR-TEM, JEOL 2010 operated at 200 kV.

1.8.7. Energy-dispersive X-ray spectroscopy (EDS)

EDS is a quantitative and qualitative X-ray micro-analytical technique that can determine the chemical composition of a sample. A beam of the electron is directed on the compound in either SEM or TEM. The primary beam of electrons penetrates the sample surface of the compound and interrelates with the compositional atoms. The X-rays generated from the sample surface are recorded by an Energy Dispersive detector, which shows the signal as a spectrum[175].

1.8.8. Thermo-gravimetric analysis (TGA)

TGA is a continuous procedure to contemplate the thermal degradation of materials. The analysis includes the estimation of sample weight with respect to the reaction temperature based on the programmed rate of heating. Along these lines, the mass of the sample reduces rapidly in a narrow temperature range and ultimately levels off as the reactant becomes spent, which is shown as residual mass. This estimation gives data about physical and chemical phenomena like phase transitions, adsorption, desorption, thermal decomposition, chemisorption. In the present study, TGA was carried out on a NETZSCH, STA-2500 Regulus thermo analyzer with the heating rate of 10 °C/min (from RT to 1000 °C) under O_2 atmosphere.

1.9. Objectives and scope of the present work

Direct methanol fuel cells (DMFCs) are usually considered as promising power sources for portable systems on account of their unique properties like lightweight, small size and high energy density. But, the practical usage of DMFCs still has not been well attained even though researchers all over the world have been accompanied for two decades. It is primarily ascribed to the deficit of highly active and durable electrocatalysts for methanol oxidation reaction (MOR) at anode. For DMFCs, platinum (Pt)-based electrocatalysts usually exhibit enhanced electrocatalytic MOR activity at the anode. However, conventional Pt-based electrocatalysts still suffer from the high price and metal loading, poor stability, methanol cross-over and sluggish kinetics. Pt surface can easily adsorb CO species along with the other carbonaceous species resulted during MOR, which eventually leads in blocking the active sites of the electrocatalysts to lower electrocatalytic activity. The other main problem is the cost and depletion of Pt reserves. Therefore, as an alternative to the commercial high efficient Pt, Pd is chosen as an appropriate alternate which is cheaper than Pt, four time more abundant and highly reactive toward MOR in initial studies.

$$CH_3OH \longrightarrow CO_{ads} + 4\,H^+ + 4\,e^- \qquad \text{eq (1.6)}$$

$$CO_{ads} + 2\,OH^- \longrightarrow CO_2 + H_2O + 2\,e^- \qquad \text{eq (1.7)}$$

$$CO_{ads} + OH_{ads} \longrightarrow CO_2 + H_2O \qquad \text{eq (1.8)}$$
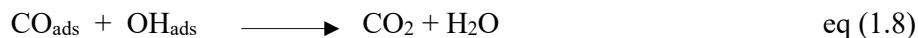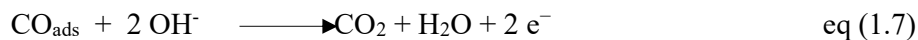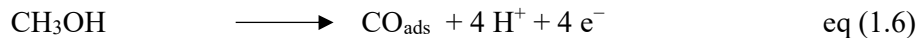
In methanol oxidation reaction, the dehydrogenation of CH_3OH takes place initially in order to form CO_{ads} (eq 1.6), and the removal of surface-adsorbed CO species (CO_{ads}) by oxidation, which is considered as the main step for MOR. This is encouraged by the existence of OH^- species on (or adjacent to) active sites of Pt (eqs 1.7 and 1.8). Even though the OH_{ads} is beneficial for the elimination of adsorbed CO species, which are adsorbed on the neighbouring or on the active site of Pt, the excessive adsorption of OH (OH_{ads}) leads for oxidizing Pt to PtO at high potentials and results in catalyst corrosion and low durability.

In alkaline environments, the free OH^- may remove the adsorbed CO (CO_{ads}) from the surface of the electrocatalysts by Eley−Rideal (E-R) mechanism (eq 1.7). But, Lu et al. reported that the reaction for the removal of CO_{ads} primarily occurred via the Langmuir−Hinshelwood (L-H) mechanism (eq 1.8) rather than the E-R mechanism (eq 1.7). Additionally, they also specified that bifunctional electrocatalysts with both OH^- and CO adsorption sites are more necessary for MOR [176]. Therefore, in order to build a hybrid heterostructured electrocatalyst favourable in enhancing the MOR activity, materials possessing binding affinities to both OH_{ads}

and O-containing intermediates (CO, etc.) were included. With the current trend in technology, carbon black (Vulcan XC-72R) supported Pt nanoparticles (Pt/C) is mostly used as a catalyst for fuel cell. It offers high surface area, electrical conductivity and highly porous structures. The major drawback of this catalyst is short durability, stability and corrosion due to electrochemical oxidation. The performance of the fuel cell reduces due to the segregation of metal nanoparticles and electronic isolation from the carbon support.

Therefore, for the improvement in the performance of fuel cell.

- It is necessary to find out more stable alternative support material to replace carbon with different carbon support materials.

- The alternative materials (graphene, carbon nanotubes (CNT), conducting polymers, metal oxides, nitrides, carbide, etc.) as a support for nanomaterials should have some of significant properties including higher corrosion resistance, electronic conductivity, electrochemical stability, surface area, uniform distribution of nanoparticles on the surface of support and strong interaction between support and metal nanoparticles.

- By employing different synthesis procedures like chemical reduction method, solvothermal and microwave assisted method along with different carbon supports like CNT, NBCNT(non-covalent functionalized CNT), NG180 (N-doped graphene) and rGO with Pd as electrocatalysts, a number of hybrid nanocomposite electrocatalysts are synthesized in our laboratory, well characterised and studied as anode catalysts for MOR.

- We have selected and fabricated a set of hybrid nanocomposite materials, which include Pd/C, Pd/CNT, Pd/NBCNT/, Pd/NG180, $Pd_{20-x}Au_x$/NG180 and Pd-MoSe$_2$-rGO, characterized, studied for MOR in alkaline conditions and discussed in the following chapters of the Thesis.

- Structural characteristics, compositions, electronic states and morphologies of the hybrid nanocomposites and electrochemical characteristics, electrocatalytic activity, CO poisoning and long-time durability towards MOR are discussed to arrive at conclusions and strategies for the development of efficient electrocatalytic composite materials for electrochemical methanol oxidation toward direct-methanol fuel cells.

Chapter 2

Pd Nanoparticles Embedded Carbon Nanotube Interface for Electrocatalytic Oxidation of Methanol towards DMFC Applications

2. Pd Nanoparticles Embedded Carbon Nanotube Interface for Electrocatalytic Oxidation of Methanol towards DMFC Applications

2.1. Introduction

Most of the world energy requirements are currently achieved by using fossil fuels. The use of fossil fuels in combustion engines and thermal processes leads to the consequences in terms of atmospheric pollution, impact on public health, greenhouse effect, global warming, etc. due to the release of NO_x gases, volatile organic compounds and particulate matter emissions. Clean energy initiatives are increasingly important areas for technological innovation owing to rapidly increasing global populations and energy demands[177–181]. Furthermore, a typical gasoline automobile engine operates only at around 20% thermal efficiency. Fuel cells have attracted great interest due to the adverse effect of the fossil fuels on the environment and also depletion of fossil reserves for the past few decades. Fuel cells are promising candidates to meet future energy demands as clean energy resources because of their higher fuel efficiencies (up to 60%) than thermal engines (around 20%), zero emissions and suitability for distributed power generation. Fuel cells eliminate all the environmental and health concerns related to the use of combustion engines. Direct use of methanol eliminates the complexity of converting methanol to hydrogen through an external reformation process. Direct methanol fuel cell (DMFC) is in today's world an increasingly interesting field of research among various types of fuel cells, because of its excellent features like high energy density, friendly operating conditions, ease of fuel storage and portability[182–186]. Direct methanol fuel cells (DMFCs) have been envisioned as suitable clean energy sources for electric cars, laptops, mobile phones, etc. and started to replace batteries in mobile phones and laptops commercially. The volumetric energy density of fabricated methanol fuel cells is at least a few times higher than various kinds of batteries, e.g. Ni-Cd, Ni-MH and Li-ion batteries. DMFCs devices currently suffer from methanol crossover and sluggish methanol electro-oxidation kinetics[181,187,188].

Noble metals and non-noble metals have attracted great interest as a source of anode and cathode catalysts in fuel cells. Platinum-based anode and cathode catalysts have taken a key role in the fuel cell research [40,189–192]. The development of efficient anode catalysts has attracted great interest in DMFC applications, and platinum-based catalysts have performed as the best electrocatalysts for methanol oxidation. However, these catalysts are costly and easily poisoned

by the intermediates formed. In recent years, it is observed that the behavior of Pd towards methanol oxidation especially in alkaline medium is similar to Pt. Further, Pd is highly abundant, low cost and relatively resistant to CO poisoning [190,193–196].

Unfortunately, bare Pd nanoparticles generally more prone to aggregate which leads to an adverse impact on their electrocatalytic activity. Carbon supports prevent the aggregation of nanoparticles. Carbon materials of the high surface area were generally employed as catalyst supports because of their good electrical conducting behavior as well as stability in both alkaline and acidic media. In recent years, numerous types of carbon sources have been explored and investigated as support for Pd-based electrocatalysts such as carbon black [197–199], carbon nanotubes [43,200–202], carbon fiber [203], mesoporous carbon and graphene [23,204,205].

Among the various types of carbon support materials, multi-walled carbon nanotubes (MWCNTs) have attracted great interest as catalyst supports for fuel cells because of its unique electrical and structural properties. MWCNTs are investigated immensely due to their wide variety of salient features such as high mechanical strength, nanowires of few hundred micrometers, long tubular geometry and its chemically inert behavior with high electrical conductivity. They are used as an ideal catalyst carrier and support material for loading noble and non-noble metal nanoparticles in various catalytic applications. However, pristine MWCNTs are chemically inert due to the lack of sufficient binding sites for anchoring precursor metal ions or metal nanoparticles, which probably leads to poor dispersion and also aggregation of nanoparticles especially when employed at high metal loading. Thus, to introduce more surface anchoring groups like -COOH, chemical oxidative processes have been generally employed.

Chitosan is a biopolymer [206] derived from the shells of shrimp and other crustaceans. It attracted great interest for dispersion of MWCNTs because of its salient features such as excellent film forming ability, high dispersion in water, good in adhesion, high mechanical strength and biocompatible. Apart from chitosan, Nafion was also employed as a dispersing agent in the preparation of modified electrodes. We have compared the influences of these two dispersants (chitosan (CS) and Nafion (Nf)) on the binding of Pd-MWCNT nanocomposites onto the electrode surface and on the electrocatalytic performances of the prepared nanocomposite electrodes.

In this work, we synthesized Pd-MWCNT catalysts in different weight ratios of Pd and MWCNT (1:5, 2:5 and 3:5) for the electrocatalytic oxidation of methanol in an alkaline system. The electrocatalytic efficiencies of the Pd-MWCNT catalysts were investigated by two different dispersing agents such as chitosan and Nafion, which were used in the preparation of Pd-MWCNT dispersed catalytic inks. The electrocatalytic efficiencies of the Pd nanocomposites for methanol oxidation in 0.5 M NaOH solution were investigated thoroughly by analyzing the electroactive surface area, electrocatalytic methanol oxidation and CO stripping characteristics by cyclic voltammetry (CV) and chronoamperometry (CA) measurements.

2.2. Experimental

2.2.1. Chemicals

$PdCl_2$, $NaBH_4$, nitric acid, ethanol, methanol, NaOH and acetic acid were procured from Merck, India. All the chemicals and reagents used in this experiment were of analytical grade and were used as received without further purification. MWCNTs (95%, 30–50 nm OD and 10–30 μm length) were purchased from Sisco Research Laboratories, India. Chitosan of low molecular weight range (from crab shells, 60–120 kDa, and minimum 85% deacetylation) and Nafion were obtained from Sigma-Aldrich, USA. All aqueous solutions were prepared using the double distilled water purified by ultrahigh water purifier (Smart2Pure UV UF; Thermo Scientific, HongKong) with the output resistance of 18.2 Mohm.cm and finally dispensed through 0.2 micron filter.

2.2.2. Functionalization of MWCNT

MWCNTs were functionalized with –COOH groups by employing a method described in the literature [207,208]. Typically, MWCNT (120 mg) added to 10 mL of 3 M HNO_3 was stirred for 24 h at 60 ºC. The resulted black solid suspension was filtered and then washed several times with ultra-pure water until the filtrate solution became neutral (pH = 7). The resulting black solid product was collected in a Petri dish and dried in an oven at 80 ºC for 24 h. HNO_3 oxidizes MWCNTs and introduces numerous –COOH groups at the ends and at the sidewall defects of the MWCNT structure, which could enhance the metal loading with fine distribution and could increase the dispersion of MWCNT in the catalytic ink. To characterize the functionalized

MWCNTs, the number of –COOH groups per gram of MWCNTs was analyzed by an acid–base back titration method and was observed to be 2.14 ± 0.08 mmol g^{-1} (n = 4).

2.2.3. Preparation of Pd-MWCNT nanocomposites

Pd-MWCNT nanocomposites were synthesized using the borohydride reduction method. $PdCl_2$ was ultrasonicated in water at 50 ºC for 1 h to obtain a homogenous solution. The functionalized MWCNTs were dissolved in double distilled water and then stirred for a period of 30 min. The Pd solution was then added to the resulting mixture and then stirred for a period of 1 h. Aqueous $NaBH_4$ ($Pd:NaBH_4$ = 1:70 w/w) solution was added to the above homogeneous mixture drop-by-drop and further stirred for a period 8 h before being filtered and washed several times with the double distilled water and then dried in an oven at 80 ºC for 24 h [209]. The catalysts were prepared in three different weight ratios of Pd and MWCNT as (1:5), (2:5) and (3:5).

2.2.4. Preparation of Pd-MWCNT-CS and Pd-MWCNT-Nf modified electrodes

At first, glassy carbon electrodes (GCEs; 3 mm diameter; CH Instruments, USA) were polished with aqueous alumina slurries of 1 μm and 50 nm, washed thoroughly with double distilled water, sonicated in 1:1 aq. HNO_3, ethanol and double distilled water consecutively and finally dried at room temperature. A solution of 0.1 % (w/v) chitosan was prepared by dissolving 100 mg of chitosan in 100 mL of aq. 1% (v/v) glacial acetic acid and sonicated for 30 min. Chitosan (0.1 % w/v) and Nafion (0.05 % w/v) were used for the preparation of catalytic inks. Then 2.5 mg Pd-MWCNT catalyst was added to 500 μL chitosan or Nafion solution as prepared earlier and sonicated for 5 min. Then, 2 μL of the resultant homogeneous suspension was cast onto the surface of the cleaned GCE and dried for 24 h at room temperature, and the resulting modified electrodes were denoted as Pd-MWCNT-CS and Pd-MWCNT-Nf.

2.2.5. Characterization

Powder X-ray diffraction (XRD) of Pd-MWCNT composites were recorded in the range of 10º – 90º 2θ on a Bruker AXS D8 diffractometer and Cu was used as the target (K_α = 1.5406 Å) with a step size of 0.002º and a scan speed of 0.5 s per step. The composition of the catalysts was determined using energy dispersive X-ray spectroscopy (EDS). Transmission electron microscopy (TEM) was taken using JEOL JEM-2100 (Japan) operated at 200 kV. X-ray photoelectron

spectroscopy (XPS) was carried out on a Thermo VG scientific ESCALAB 250 spectrometer with an Al Kα radiator and the vacuum in the chamber was maintained at about 10^{-9} millibar.

2.2.6. Electrochemical analysis

Voltammetric experiments were performed by using an Electrochemical Potentiostat/Galvanostat (Model 619d, CH Instruments, USA). A three electrode conventional cell of 20 mL volume was used with bare or modified glassy carbon electrode as the working electrode and spiral Pt wire as the counter electrode. All the potentials were referred against Ag|AgCl (3 N KCl) at room temperature. The catalytic performances of the prepared catalysts were analyzed by CV in aq. 0.5 M NaOH +1 M CH_3OH at 25 ºC. Chronoamperometry tests were also carried out at -0.1 V for 8000 s. Before performing each test, the solution was purged with ultra-high purity N_2 for 15 min to eliminate the dissolved O_2. CO stripping experiments were performed in a solution of 0.5 M NaOH with a scan rate of 50 mV s^{-1}. Pd-MWCNT electrodes were subjected to CO adsorption in aq. 0.5 M NaOH by purging CO gas 5 min. Then, the solution was purged with N_2 for 15 min to eliminate the dissolved CO before recording CO stripping voltammograms.

2.3. Results and discussion

2.3.1. Characterization of Pd-MWCNT nanocomposites

XRD technique was used to study the crystalline nature of the prepared Pd-MWCNT catalysts of three different wt ratios (1:5, 2:5 and 3:5) of Pd and MWCNTs. All the synthesized Pd-MWCNT catalysts exhibited a broad peak at 26.0º (Fig. 2.1 (A)), which corresponds to the (002) plane of graphitized carbon. The typical characteristic peaks of a face-centered cubic (FCC) crystalline Pd were observed at 39.9º, 46.5º, 68.3º and 81.8º (2θ), which could be attributed respectively to (111), (200), (220) and (311) diffraction planes (JCPDS No. 87-0638) [193]. The crystallite size of Pd nanoparticles was calculated by using Scherrer formula, and the average crystallite size observed from the calculation was 8 – 9 nm for all the Pd-MWCNT composites. It was further confirmed by TEM analysis (Fig. 2.2 (B), *vide infra*). Figure 2.1 (B) shows the EDS spectrum of Pd-MWCNT (1:5) nanocomposite and it confirms that Pd nanoparticles were successfully deposited on MWCNTs.
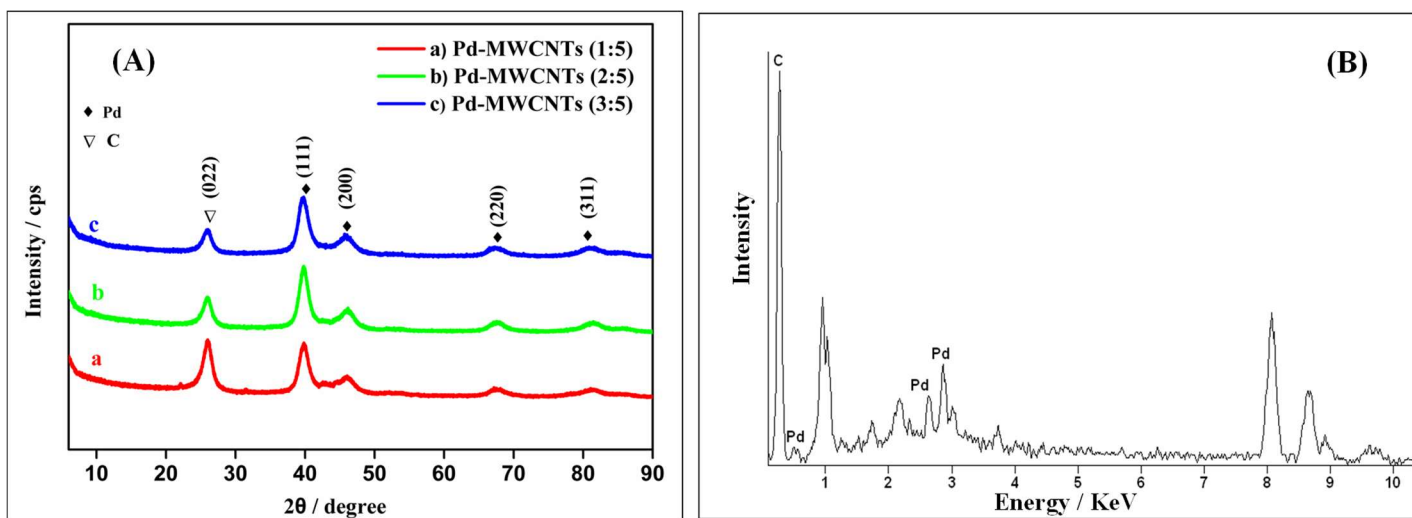
Fig. 2.1. (A) XRD patterns of Pd-MWCNT nanocomposites of different wt ratios (a) 1:5, (b) 2:5 and (c) 3:5. (B) EDS spectrum of Pd-MWCNT (1:5) nanocomposite.

TEM analyses were also carried out for the synthesized Pd-MWCNT catalysts at different magnifications. From Fig. 2.2 (A, B), it was observed that the MWCNT seemed to exhibit clean and smooth surfaces from the pretreatment process. The TEM images clearly show that the Pd nanoparticles were embedded on the surface of MWCNT and well dispersed with only a little Pd agglomeration at some places in the synthesized Pd-MWCNT catalyst. It is evident from the TEM studies that MWCNTs possessed the –COOH functional groups and the Pd nanoparticles were embedded on the surface of the MWCNTs with uniform distribution all over the MWCNT matrix and with a finite size for Pd nanoparticles within 8 - 9 nm.

XPS studies have been done to study the nature of Pd-MWCNT nanocomposites. Figure 2.2 (C) shows the survey spectrum of the Pd-MWCNT (2:5) nanocomposite, where it shows the characteristic peaks of C 1s, O 1s and Pd 3d. Figure 2.2 (D) shows the high-resolution XPS spectrum of Pd 3d. The deconvoluted Pd 3d XPS spectrum of the catalyst exhibits two characteristic photoelectron peaks at 335.3 and 340.5 eV of Pd $3d_{5/2}$ and Pd $3d_{3/2}$, ascribed to metallic Pd^0. The other two characteristic photoelectron peaks at 336.3 and 342.2 eV of Pd $3d_{5/2}$ and Pd $3d_{3/2}$ are ascribed to $Pd^{II}O$ [202].
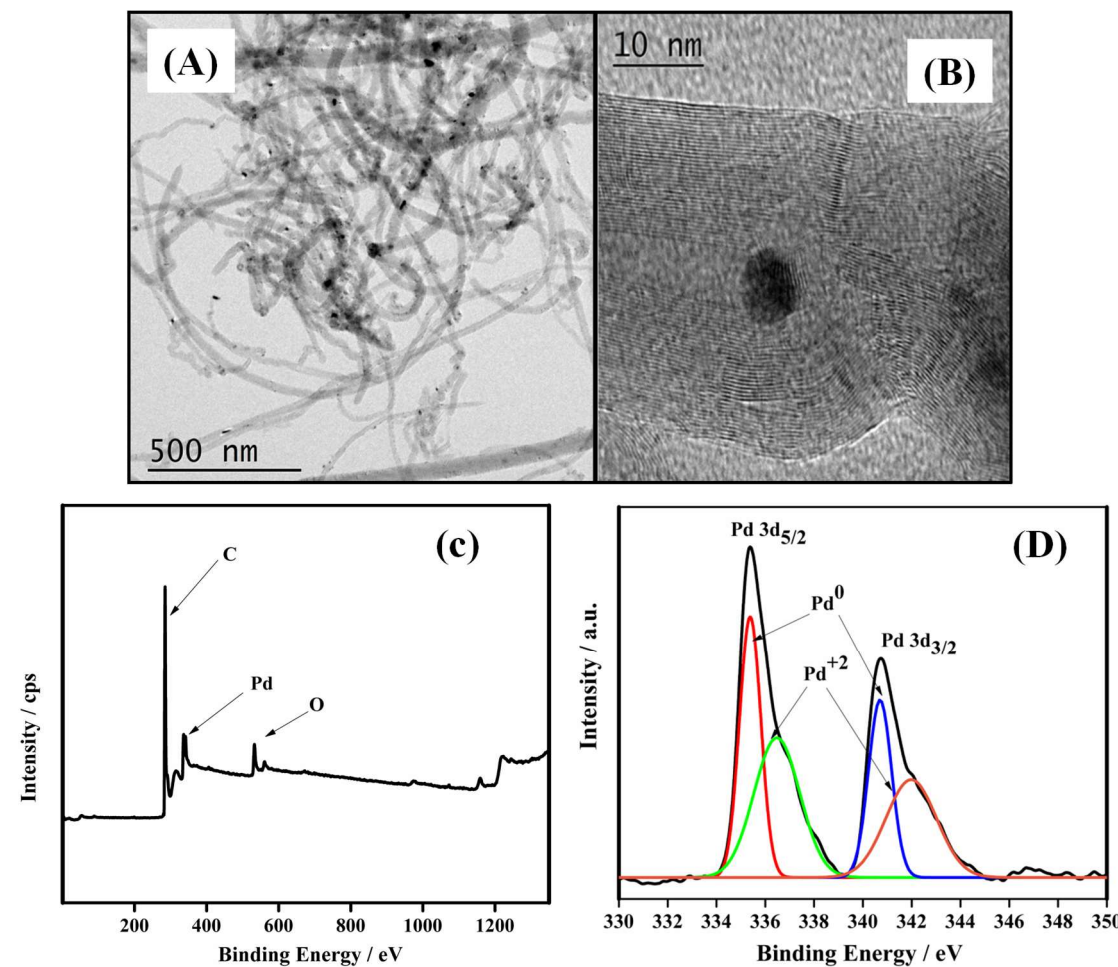
Fig. 2.2. (A, B) TEM images of Pd-MWCNT (2:5) nanocomposites at different magnifications. (C) XPS survey spectrum for Pd-MWCNT (2:5) nanocomposites. (D) The high-resolution XPS spectrum of Pd-MWCNT (2:5) nanocomposite in Pd 3d region along with deconvolution peaks.

2.3.2. Electrochemical active surface area (EASA)

The electrocatalytic activity of an electrode material is known to depend upon the geometrical and also on electronic properties of the material. Therefore, the electrochemical active surface area (EASA) of the modified GCE was determined, as described elsewhere [203,210,211]. The EASA of the modified electrodes were calculated by determining the coulombic charge (Q) for the reduction of PdO. The CVs recorded for the determination of EASA are shown in Fig. 2.3. The resultant EASA values from the CV studies were shown in Table 2.1, which were determined by using the relation, EASA = Q/Sl, where 'S' is the proportionality constant used to relate charge with the active surface area and 'l' is the catalyst loading in 'g'. A coulombic charge of 405 μC

cm^{-2} was assumed for the reduction of PdO monolayer. Pd-MWCNT nanocomposites with 2:5 wt ratio have shown high EASA values with the both chitosan and Nafion dispersants. The EASA values were 138.9 m^2 g^{-1}_{Pd} and 108.1 m^2 g^{-1}_{Pd} for 2:5 wt ratio of Pd-MWCNT-CS and Pd-MWCNT-Nf, respectively (Fig. 2.3). EASA values of chitosan-based Pd-MWCNT nanocomposite electrodes are higher than those of Nafion-based Pd-MWCNT electrodes. The higher EASA values for Pd-MWCNT-CS would have resulted in an enhancement in the electroactive surface area and as well as by the high dispersion of the nanocatalyst in chitosan ink.
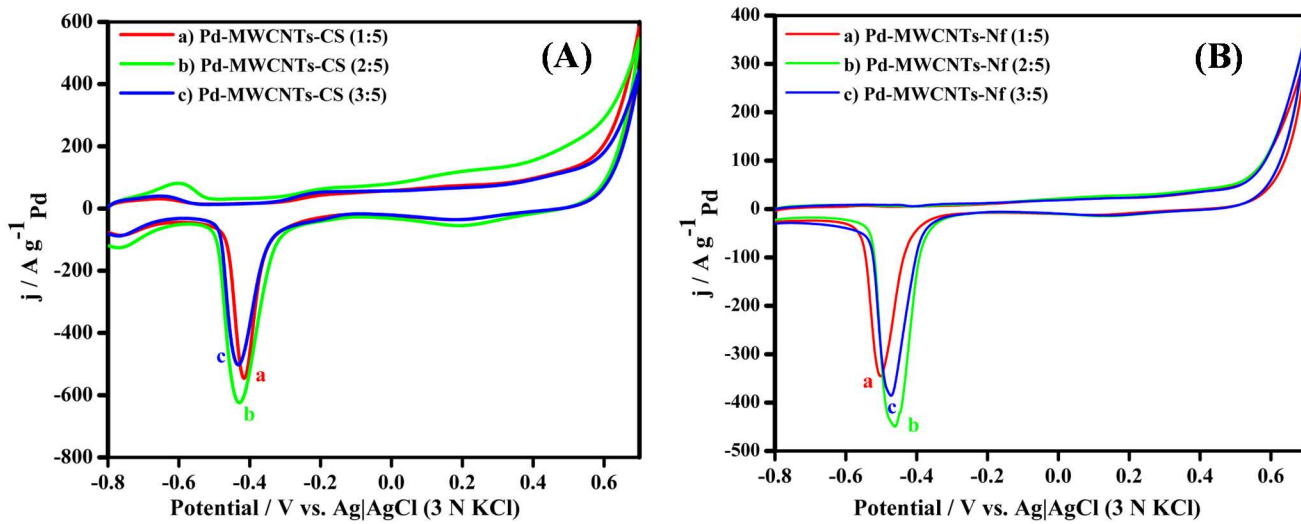
Fig. 2.3. Cyclic voltammograms of (A) Pd-MWCNT-CS and (B) Pd-MWCNT-Nf modified electrodes of different wt ratios (1:5, 2:5 and 3:5) of Pd and MWCNT in aq. 0.5 M NaOH at the scan rate of 50 mV s^{-1}.

2.3.3. Electrocatalytic oxidation of Methanol

A series of cyclic voltammetry (CV) measurements were carried out to investigate the electrocatalytic performance of the Pd nanocatalysts of Pd-MWCNT-CS and Pd-MWCNT-Nf electrodes towards methanol oxidation. Figure 2.4 (A, B) shows cyclic voltammograms of Pd-MWCNT-CS and Pd-MWCNT-Nf electrodes of different Pd:MWCNT wt ratios 1:5, 2:5 and 3:5 in aq. 0.5 M NaOH + 1 M CH_3OH at a scan rate of 50 mV s^{-1}. CVs exhibited two characteristic oxidation peaks, with one peak each in the forward and reverse scans, and the peak in the reverse scan is observed at more negative potentials compared to that in the forward scan. The peak observed in the forward scan corresponds to the oxidation of methanol, whereas the other oxidation peak observed in the backward scan corresponds to the removal of the residual adsorbed carbon

species (eg. CO) formed during the forward scan [194,211]. The peak current densities of methanol oxidation at the nanocomposite electrodes and the anodic peak potentials are given in Table 2.1. Pd-MWCNT-CS electrodes exhibit high current densities by more than two times when compared to Pd-MWCNT-Nf modified electrodes, and the methanol oxidation occurs at less over potentials (by ~120 mV) in the case of Pd-MWCNT-Nf electrodes compared to Pd-MWCNT-CS electrodes. It was observed that the Pd-MWCNT-CS nanocomposite of 2:5 wt ratio exhibited the maximum current density (2396 A g^{-1}_{Pd}) among all the electrodes and is very much high compared to that of Pd-MWCNT-Nf electrode (1041 A g^{-1}_{Pd}) of the same wt ratio (2:5). From these results, it was concluded that the Pd-MWCNT nanocomposites of 2:5 wt ratio show high electrocatalytic activity compared to those of 1:5 and 3:5 wt ratios and that the use of chitosan as dispersant dramatically enhanced the electrocatalytic oxidation of methanol.
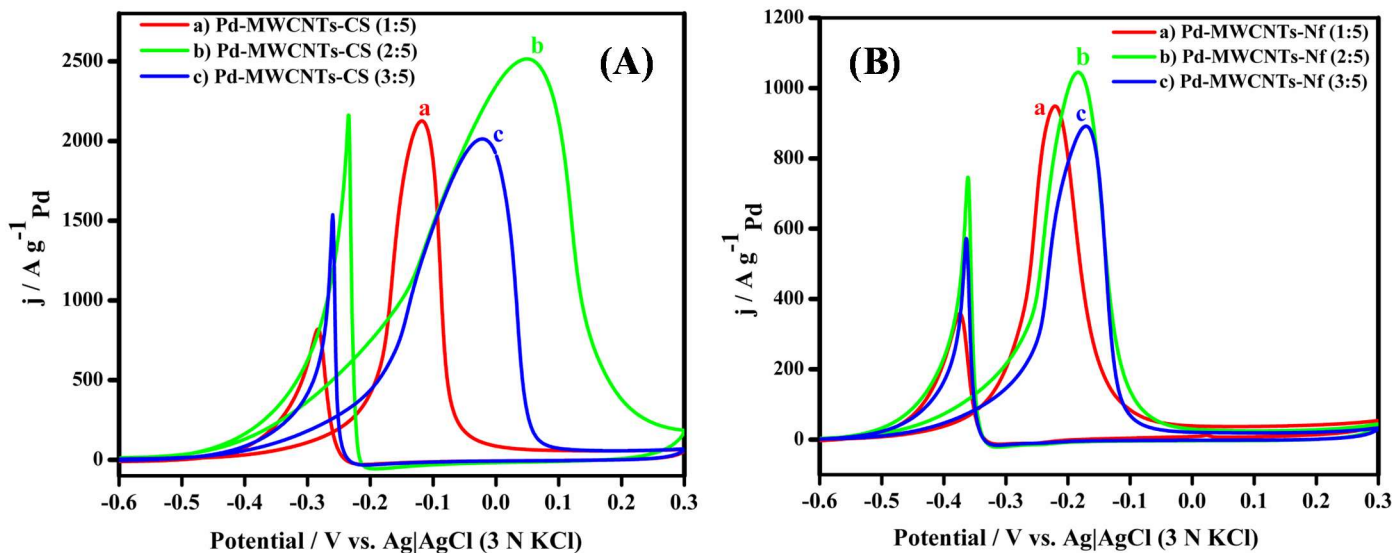
**Fig. 2.4.** Cyclic voltammograms of (A) Pd-MWCNT-CS and (B) Pd-MWCNT-Nf modified electrodes of different wt ratios of Pd and MWCNT in aq. 0.5 M NaOH + 1 M CH₃OH at the scan rate of 50 mV s⁻¹.

Table 2.1. CV analysis of Pd-MWCNT-CS and Pd-MWCNT-Nf electrodes of different wt ratios of Pd and MWCNT (1:5, 2:5 and 3:5) in aq. 0.5 M NaOH + 1 M CH$_3$OH at the scan rate of 50 mV s^{-1}.

Electrode	EASA (m^2 g^{-1}$_{Pd}$)	Anodic Peak		I$_f$/I$_b$	Q$_f$/Q$_b$
		j (A g^{-1}$_{Pd}$)	E$_p$ (V)		
Pd-MWCNT-CS (1:5)	103.4	2127	-0.28	2.6	2.7
Pd-MWCNT-CS (2:5)	138.9	2541	-0.23	1.1	4.6
Pd-MWCNT-CS (3:5)	118.1	2016	-0.25	1.3	4.4
Pd-MWCNT-Nf (1:5)	83.7	947	-0.37	2.6	3.7
Pd-MWCNT-Nf (2:5)	108.1	1041	-0.35	1.4	3.4
Pd-MWCNT-Nf (3:5)	91.1	891	-0.36	1.5	3.2

CO tolerance of Pd-MWCNT catalysts could be analyzed from the cyclic voltammograms recorded for methanol oxidation. The ratio of the anodic peak currents of the forward and reverse scans of the CVs (I$_f$/I$_b$) is a characteristic of the CO tolerance (Table 2.1). However, the ratio of the respective coulombic charges (Q$_f$/Q$_b$) would be more appropriate to evaluate the CO tolerance of the catalysts. The Q$_f$/Q$_b$ ratio of Pd-MWCNT-CS electrodes is high compared to that of Pd-MWCNT-Nf electrodes, and the Q$_f$/Q$_b$ ratio is maximum for the Pd-MWCNT-CS catalyst of 2:5 wt ratio. Consequently, such a high CO tolerance is very much in support of the maximum peak current density observed at the Pd-MWCNT-CS (2:5 ratio) electrode. The electrocatalytic activity of these nanocomposite catalysts for methanol oxidation was further studied by steady state current vs. time measurements.

2.3.4. Chronoamperometry studies of methanol oxidation

Figure 2.5 (A, B) shows the chronoamperometry plots of Pd-MWCNT-CS and Pd-MWCNT-Nf modified electrodes in aq. 0.5 M NaOH + 1 M CH$_3$OH at a constant potential of -0.1 V vs. Ag/AgCl. The plots show an initial rapid decrease followed by a gradual decrease in the mass activity or current density with time [211]. This decrease can be attributed to the poisoning of electrocatalysts due to the formation of adsorbed intermediates, particularly CO species onto the

surface of Pd catalysts. The current density for methanol oxidation of all the chitosan-based Pd-MWCNT electrodes is high compared to Nafion-based electrodes.
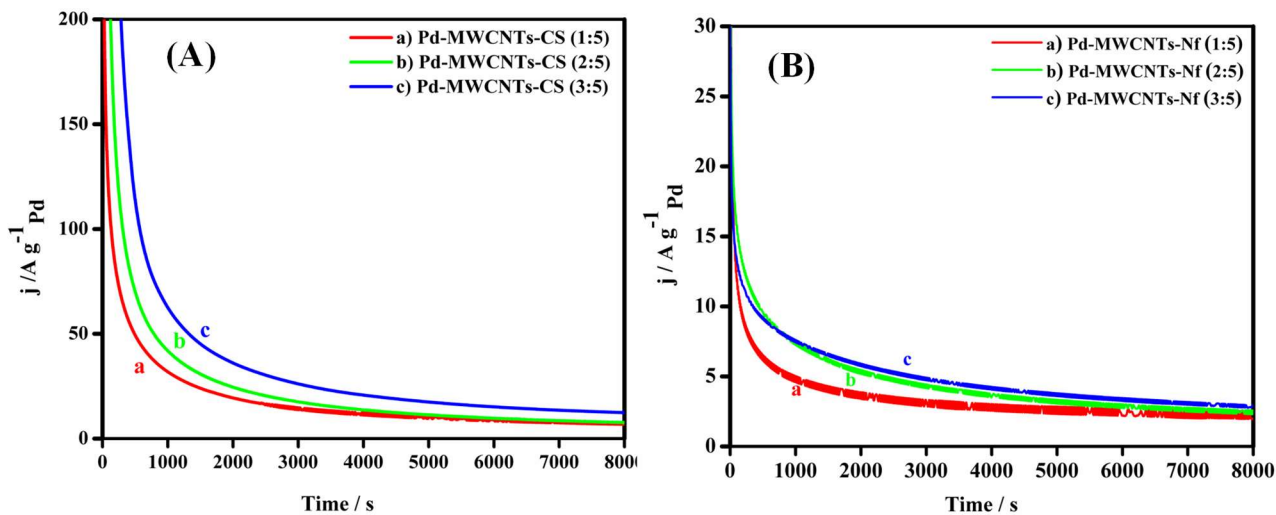

Fig. 2.5. Chronoamperometry plots of (A) Pd-MWCNT-CS and (B) Pd-MWCNT-Nf modified electrodes of different wt ratios of Pd and MWCNT in aq. 0.5 M NaOH + 1 M CH_3OH at – 0.1 V.

In steady state current - time analysis, the current density for methanol oxidation at these nanocomposite electrodes were maximum when the wt ratio of Pd and MWCNT is 3:5. This is in contrary to the peak current densities observed for methanol oxidation in CV studies, where nanocomposites of 2:5 wt ratio gave maximum values. Furthermore, the steady-state current densities observed at Pd-MWCNT-CS electrode of 3:5 ratio is 20.8 A g^{-1}_{pd} at 4000 s. This value is very much high compared to that observed 4.1 A g^{-1}_{Pd} at the Nafion-based electrode (Pd-MWCNT-Nf 3:5). The results reveal that the Pd-MWCNT-CS modified electrodes were highly efficient electrocatalysts for methanol oxidation in alkaline medium compared to that of Pd-MWCNT-Nf modified electrodes. Further, CO stripping studies were also performed to study the stability and reactivity of the electrodes toward CO poisoning.

2.3.5. CO-stripping voltammograms

CO stripping voltammograms of the Pd-MWCNT-CS and Pd-MWCNT-Nf modified electrodes of different wt ratios of Pd and MWCNT are shown in Fig. 2.6 (A, B). CO species are the main poisoning species formed during the methanol electro-oxidation. To obtain an efficient electrocatalyst for methanol oxidation, it should possess excellent CO electrooxidation and as well

as tolerance ability, which can be evaluated by CO stripping voltammetry [190,194,212,213]. In all the CVs obtained, the oxidation peak observed in the first cycle can be associated with the oxidation of the CO species adsorbed on the catalyst. In the second cycle, the oxidation peak observed during the first cycle totally disappeared, indicating that the adsorbed CO was completely oxidized during the first forward scan itself. The peak potentials and the coulombic charges obtained from CO stripping studies were presented in Table 2.2. The CO oxidation peaks were observed at ~ -0.2 V for all the electrodes. The coulombic charge (Q_{CO}) observed for the oxidation of the adsorbed CO species is very much high for Pd-MWCNT-CS electrodes compared to Pd-MWCNT-Nf electrodes. Furthermore, the Pd-MWCNT-CS (3:5) electrode exhibited maximum steady state current for methanol oxidation. All the results suggest that the Pd-MWCNT-CS (3:5) modified electrode acquired better CO electro-oxidation ability, and it reveals that it has less opportunity of being poisoned by CO_{ads} species during methanol oxidation.
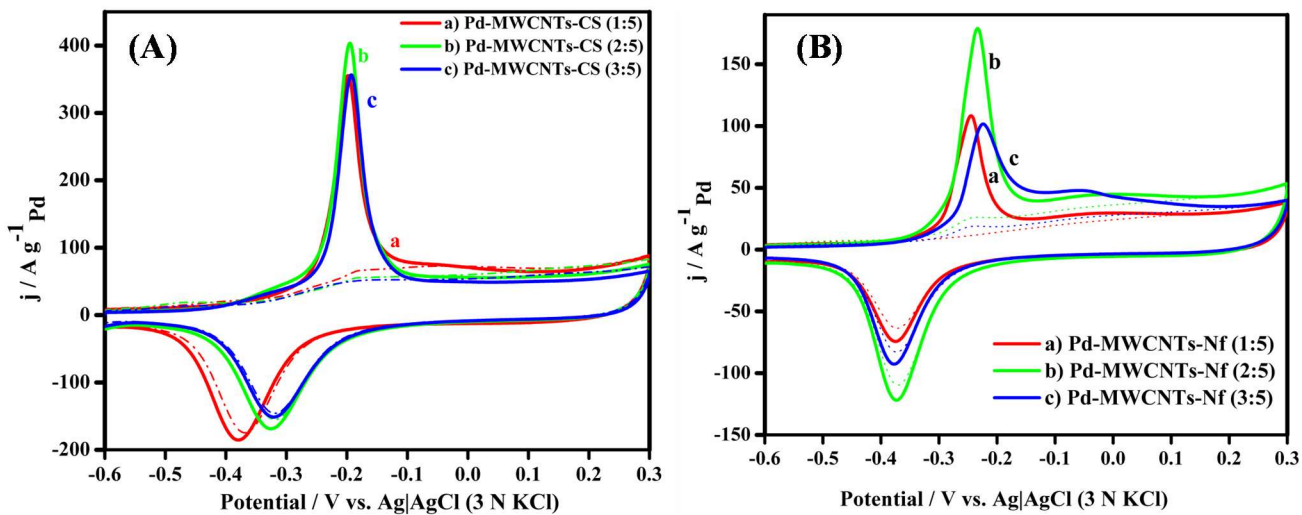
**Fig. 2.6.** CO stripping voltammograms (A) Pd-MWCNT-CS and (B) Pd-MWCNT-Nf modified electrodes of different wt ratios of Pd and MWCNT in aq. 0.5 M NaOH at the scan rate of 50 mV s^{-1}. (_____ full lines: first scan; - - - - dotted lines: second scan).

Table 2.2. Anodic peak potentials and coulombic charges of oxidative CO stripping studies with CV analyses in aq. 0.5 M NaOH.

Electrode	E (V)	Q_{CO} (C g$^{-1}_{Pd}$)
Pd-MWCNT-CS (1:5)	-0.19	233.5
Pd-MWCNT-CS (2:5)	-0.19	280.1
Pd-MWCNT-CS (3:5)	-0.19	227.5
Pd-MWCNT-Nf (1:5)	-0.24	73.5
Pd-MWCNT-Nf (2:5)	-0.23	126.8
Pd-MWCNT-Nf (3:5)	-0.22	78.2

2.4. Conclusions

In summary, Pd nanoparticles of finite and uniform size of 8-9 nm embedded MWCNT electrocatalysts were synthesized by sodium borohydride reduction method. TEM, XRD and XPS analyses revealed that the metallic state Pd nanoparticles were of finite crystalline nature and contained both Pd^0 and Pd^{II} oxidation states. Among the dispersants, nanocomposite electrodes fabricated with chitosan dispersant exhibited high electroactive area and high current density for methanol oxidation. A dramatic increase in the steady-state catalytic current for methanol oxidation was observed at Pd-MWCNT-CS (3:5) electrodes (20.8 A g$^{-1}_{pd}$) compared to Pd-MWCNT-Nf electrode (4.1 A g$^{-1}_{pd}$). These observations emphasize the importance of a suitable dispersant for the fabrication of an efficient electrocatalyst. The CO stripping oxidation potentials are very much less positive compared to the methanol oxidation peak potentials. Electrocatalytic methanol oxidation and CO stripping measurements reveal that the application of chitosan as a dispersion medium for Pd-MWCNT catalysts significantly improved the electrocatalytic activity, stability and durability of the catalyst for methanol oxidation. By emphasizing these results, it revealed that the Pd-MWCNT-CS would be promising catalysts for DMFC applications.

Chapter 3

Pd Nanoparticles Supported on Nitrobenzene (NB)-Functionalized Multiwalled Carbon Nanotube as Efficient Electrocatalysts Toward Methanol Oxidation

3. Pd Nanoparticles Supported on Nitrobenzene (NB)-Functionalized Multiwalled Carbon Nanotube as Efficient Electrocatalysts Toward Methanol Oxidation

3.1. Introduction

Direct methanol fuel cells (DMFCs) are the promising power sources among all the other type of fuel cells in terms of making portable power devices and electronic vehicles, space shuttles, etc. [178,188]. They have several advantages like relatively quick startup, rapid response to varying loading, low operating temperature and low pollutant emission [181]. However, there are difficulties in commercialization and development of fuel cells due to its kinetic constraints in methanol oxidation reaction (MOR), cost of the catalysts and limited supply of platinum [184]. Pt based catalysts and their alloys are the widely employed electrocatalysts for the methanol oxidation preferably in acidic medium. In recent years, many non-platinum electrocatalysts have been explored for the alkaline systems.

Among non-platinum electrocatalysts, Pd is the most promising, low cost transition metal and five times more abundant on the earth. Recent studies have revealed that Pd based electrocatalysts show good electrocatalytic activity toward methanol oxidation in alkaline medium [214,215] However, the activity, loading level, dispersivity and stability of the Pd based electrocatalysts need be improved. Carbon supports, Vulcan XC and activated carbon black, have been studied extensively for Pt loading in DMFCs [199]. But the drawbacks are due to poor conductivity, easy corrosivity and also effects of loading of metal nanoparticles with agglomeration due to the lack of proper active sites to bind. Among the different carbon supports employed for developing the electrocatalysts, mutliwalled carbon nanotubes (CNTs) have attracted great importance in different applications such as supercapacitors, energy storage, sensing, heterogeneous catalysis, etc. by the researchers worldwide [216]. CNTs have unique properties like high electronic conductivity, high surface area to volume ratio and good thermal stability, which make them ideal support materials for energy applications. But the practical applications have been stuck by the processing complications. In principle, anchoring of the metal nanoparticles always takes place at the defect sites but not on the sidewalls of nanotubes, which are being created by the covalent functionalization of CNTs [217]. Functionalization and surface treatment of carbon nanotubes are essential to improve dispersivity of CNTs, wettability, loading levels of catalysts and uniform distribution of catalytic nanoparticles. For this purpose, chemical oxidation to

incorporate hydrophilic moieties -OH, -COOH, etc. on the surface, ionic liquids, adsorption of surfactants, heteroatom doping, thin-film formation of ionic polymers on the surface, treatment with biopolymers like chitosan, etc. have been investigated. Predominantly, most of the surface modification protocols decrease either the graphitic nature of CNTs or the interaction with immobilized nanoparticles, and thus ultimately decreasing the electrical conductivity and electronic transport at the interface. Hence, in this investigation, the surface of the nanotubes is investigated with a simple non-covalent binding method for functionalization and immobilization of metallic nanoparticles onto CNTs [218].

We have proposed the nitrobenzene (NB)-functionalized CNTs as the non-covalent bonding strategy for the support of Pd nanoparticles on CNTs as part of our continuing efforts in making low cost, highly stable and efficient anodic electrocatalysts for DMFC applications in alkaline medium [219]. The synthesized non-covalent NB-functionalized CNT based nanoPd electrocatalysts have been investigated in enhancing the catalytic activity and stability for electrocatalytic methanol oxidation compared to covalently functionalized CNT based electrocatalysts. Performance, characteristics and stability of the electrocatalysts were investigated for electrocatalytic methanol oxidation with surface analytical techniques, electron microscopy, electroactive area, cyclic voltammetry, CO stripping analysis and amperometric i-t analysis.

3.2. Experimental

3.2.1. Chemicals

$PdCl_2$, nitric acid, isopropanol, methanol and NaOH were procured from Merck, India. Nafion, 4-nitrobenzene diazonium tetrafluoroborate (4-NBD) were obtained from Sigma-Aldrich, USA. MWCNTs (95%, 30–50 nm outer diameter (OD) and 10–30 μm length) were purchased from Sisco Research Laboratories, India. All the chemicals and reagents used in this experiment were of analytical grade and were used as received without further purification. All aqueous solutions were prepared using double distilled water purified by ultra-high water purifier (Smart2Pure UV UF, Thermo Scientific, Hong Kong) with the output resistance of 18.2 Mohm and finally dispensed through 0.2 micron filter cartridge.

3.2.2. Acid and NB functionalization of CNT

CNTs were functionalized with –COOH groups by employing a method described in the literature [220]. Typically, MWCNT (120 mg) added to 10 mL of 3 M HNO_3 was stirred for 24 h at 60 ºC. The resulting black solid suspension was filtered and then washed several times with ultra-pure water until the filtrate solution became neutral (pH = 7). The resulting black solid product was collected in a petri dish and dried in an oven at 80 ºC for 24 h. HNO_3 oxidizes CNTs and introduces numerous –COOH groups at the ends and at the sidewall defects of the CNT structure, which could enhance the metal loading with fine distribution and could also increase the dispersion of CNT in the catalytic ink. To characterize the functionalized CNTs, the number of –COOH groups per gram of MWCNTs was analyzed by an acid-base back titration method and was observed to be 2.1 ± 0.1 mmol g^{-1} (n = 3). In order to synthesize NB-functionalized MWCNT (NBCNT), 100 mg MWCNT was dispersed in aqueous solution at 1 mg mL^{-1} concentration under constant stirring at room temperature for about 1 h. The addition of 15 mg 4-NBD was performed slowly to the above CNT dispersion for homogeneous distribution. After the reaction for 15 h, NBCNT composite was washed in the order of distilled water, acetonitrile and ethanol for about 3 times each, respectively, and finally dried in a hot air oven at 65 ºC overnight [219].

3.2.3. Syntheses of Pd/CNT and Pd/NBCNT nanocomposites

Acid fuctionalized CNT and NBCNT were used to synthesize Pd/CNT and Pd/NBCNT electrocatalysts. In brief, 30 mg of NBCNT was dispersed in 50 mL ethylene glycol, and the solution was stirred and sonicated for 1 h to obtain a homogeneous solution. Then, required amount of H_2PdCl_4 precursor solution was added to the above solution and stirred for 2 h to obtain clear disribution over NBCNT. Then, pH of the mixture was adjusted to 11 by drop wise addition of 1 M NaOH solution, and the reaction mixture was subjected to reflux at 140 ºC for 12 h. Then, the solution was finally cooled to room temparature after the reaction time, and the final product was centrifuged, washed with ultrapure water, followed by ethanol to remove impurities and finally dried in hot air oven overnight at 65 ºC to obtain Pd/NBCNT electrocatalysts. The similar procedure was followed to synthesize the Pd/CNT and Pd/C electrocatalysts with the same 20 wt % Pd metal loading. The covalent functionalization of NB onto CNT surface as molecular doping occurs through the process reported in the literature, which is illustrated in Fig. 3.1. Nitrobenzene serves as a strong electron-acceptor and could bond to the surface of CNT through covalent linking

of carbon atom. The strong electron-accepting nature of nitrobenzene group is capable of withdrawing electrons from the carbon atoms of CNT skeleton, which results in the modification of electronic properties associated with CNTs [221,222], and thus consequently alters the electrocatalytic properties of CNTs embedded with Pd nanoparticles.

3.2.4. Characterization

X-ray diffraction (XRD) spectra of Pd/C, Pd/CNT and Pd/NBCNT nanocomposites were recorded by Bruker AXS D8 diffractometer with Cu Kα source (1.5406 Å), 2 mdeg step size and scan speed of 0.5 s per step. Raman spectra were recorded by micro-Raman spectrometer (HR800-UV Horiba Jobin Yvon, France) with the excitation source of 532 nm. X-ray photoelectron spectroscopy (XPS) measurements were recorded by Physical Electronics (PHI 5000 VersaProbe III) spectrometer. Surface morphology of the nanocomposites was studied using transmission electron microscopy (TEM, Tecnai G2 20 S-TWIN microscope) at the acceleration potential of 200 kV. SEM images were recorded using a scanning electron microscope, VEGA3, Tescon, USA integrated with an energy dispersive X-ray spectrometer (EDS). For SEM recording, powder samples were sprinkled on a Cu stub covered with carbon tape, followed by sputtering a thin layer of gold to prevent charging.

3.2.5. Electrochemical analysis

Voltammetric and amperometric experiments were performed by using an Electrochemical Potentiostat/Galvanostat (Model 619d, CH Instrument, USA). A three-electrode conventional cell of 20 mL volume was used with bare or modified glassy carbon electrode (GCE) as the working electrode and spiral Pt wire as the counter electrode. All the potentials were referred against Ag|AgCl (3 N KCl) at room temperature. The catalytic ink was made in order to fabricate the working electrodes by dispersing 2.5 mg synthesized electrocatalyst in 950 µL of 1:1 (v/v) $C_2H_5OH:H_2O$ mixture, and then 50 µL of 5 wt% Nafion in ethanol was added to the above mixture. 2 µL catalytic ink was drop casted onto GCE and allowed to dry under room temperature for 12 h. Catalytic performances of the prepared catalysts were analyzed by CV in aq. 0.5 M NaOH + 1 M CH_3OH at 25 °C. Chronoamperometry tests were also carried out at − 0.1 V for 2000 s. Before performing each test, the solution was purged with ultra-high purity N_2 for 15 min to eliminate the dissolved O_2.
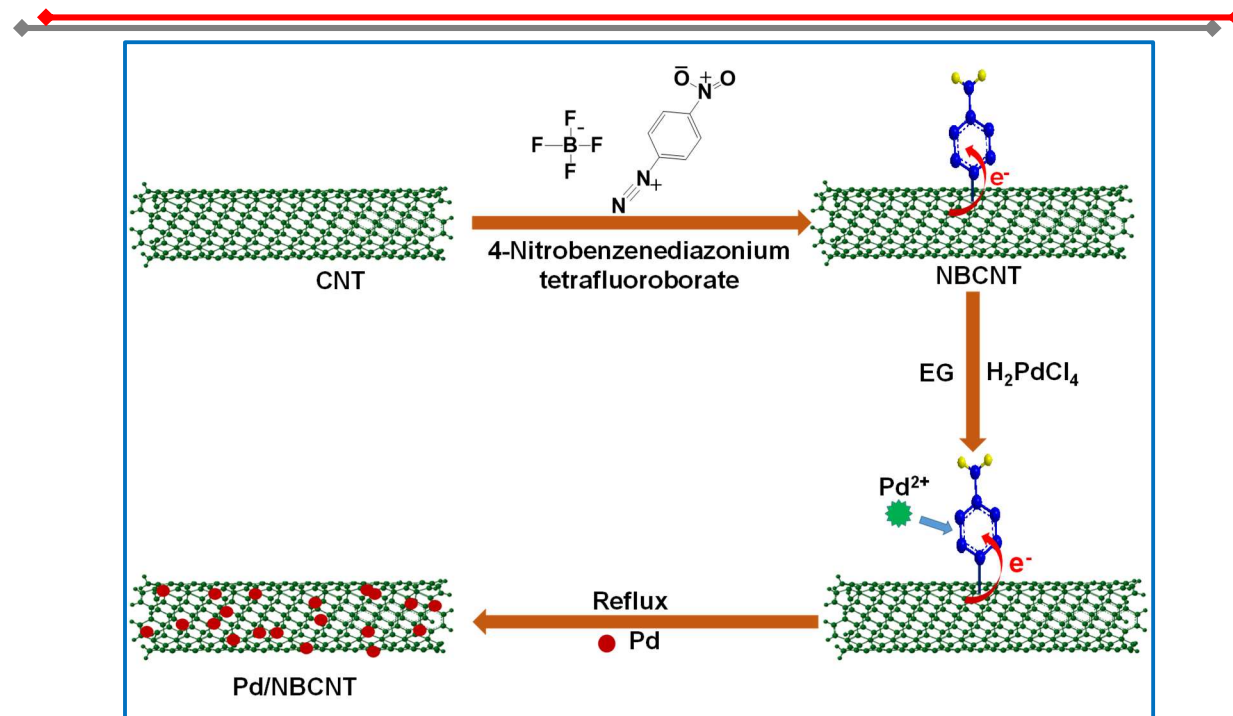
Fig. 3.1. Schematic illustration of functionalization of CNT and synthesis of Pd/NBCNT composite.

3.3. Results and discussion

3.3.1. Characterization of nanocomposites
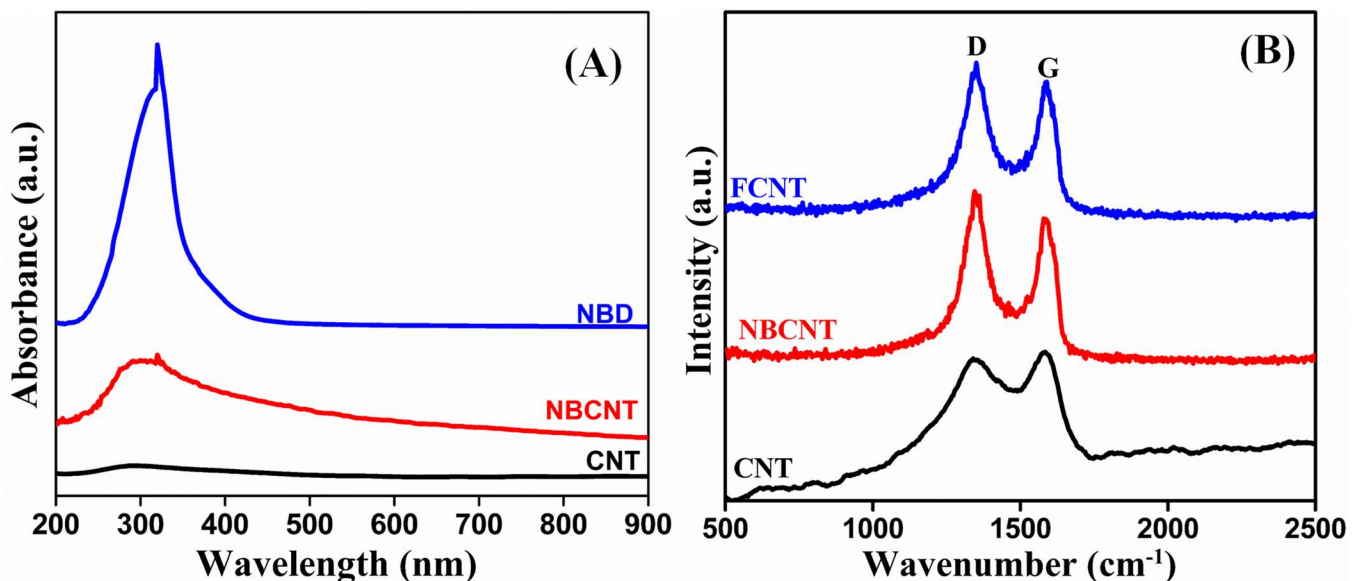
Fig. 3.2. (A) UV-Visible spectra of NBD, NBCNT, CNT composite. (B) Raman spectra of FCNT, NBCNT and CNT composite.

In order to study the functionalization of NB on the surface of CNTs to form NBCNT, UV-Visible spectra were recorded. Figure 3.2 (A) shows the UV- Visible absorption spectra of CNT, NBCNT and NBD. The UV-Visible spectrum of NBCNT in ethanol validates the binding of NB on CNT. While the pristine CNT shows an undistinguished spectrum, the absorption spectrum of NBCNT depicts the additional feature at around 325 nm that corresponds to NB [223]. The existence of strong characteristic peak of NB in NBCNT confirms the binding of NB on the surface of CNT through molecular doping. Vibrational Raman spectroscopy was also employed to study the surface structure of acid functionalized CNT (FCNT), NBCNT and pristine CNT, as shown in Fig. 3.2 (B). All the CNT samples with and without functionalization exhibit similar Raman scattering peaks. There are two distinct peaks namely D-band and G-band observed for all the CNT samples at $\sim$1340 and $\sim$1565 cm^{-1}, respectively [71,224]. It is identified that the D band represents the defects of the carbon associated with sp^3 and the G band represents the stretching frequency allied to graphitic sp^2 bonded pairs of carbon of CNT skeleton. The ratio of the intensities of D and G bands, I_D/I_G, signifies the extent of defects created in the carbon skeleton of CNT. It was observed that the I_D/I_G ratio increased from pristine CNT (0.96) to NBCNT (1.07) and increased furthermore for acid functionalized CNT (1.13). The increase in the I_D/I_G value of NBCNT compared to pristine CNT clearly confirms that there was a conversion of sp^2 carbons to sp^3 state by the molecular doping of NB molecules over the surface of CNT as described in the literature [219]. Moreover, the higher I_D/I_G value for acid functionalized CNT compared to NBCNT substantiates that the graphitic nature of CNT was retained more in NBCNT with the NB molecular doping process.
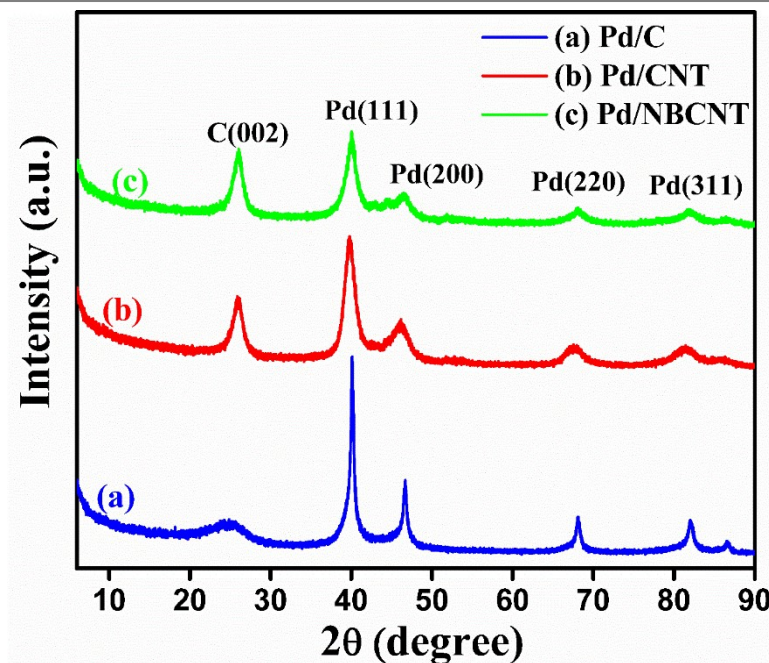
Fig. 3.3. XRD patterns of (a) Pd/C, (b) Pd/CNT and (c) Pd/NBCNT composites.

Figure 3.3 shows the X-ray diffraction (XRD) patterns of Pd/C, Pd/CNT and Pd/NBCNT electrocatalysts. The broad peak at 26.0º is ascribed to the (002) plane of the graphitic structure of CNT. The remaining four diffraction peaks are ascribed to the characteristic face centered cubic (fcc) crystalline Pd, which are corresponding to the planes (111), (200), (220) and (311) at 2θ values of about 39.9°, 46.5°, 68.3° and 81.8°, respectively [71,220]. It was observed that each of the diffraction planes of Pd/NBCNT and Pd/CNT electrocatalysts illustrate a slight negative shift with respect to that of Pd/C composite, and this observation signified that there is a slight lattice expansion of Pd when bound onto the surfaces of CNTs. The small size of nanometer levels and tubular nature of the type of CNT solid support may lead to distortions in the lattice planes, and accordingly there could be an alteration of the lattice parameters, which has also been reported in the literature previously [71]. Additionally, the average particle sizes of the synthesized electrocatalysts were calculated from XRD peaks by means of Scherrer's equation [225]. The calculated mean sizes associated to the diffraction peak of Pd (111) were found to be in the range of 6.0 nm, 8.2 nm and 12 nm for Pd/NBCNT, Pd/CNT and Pd/C electrocatalysts, respectively.
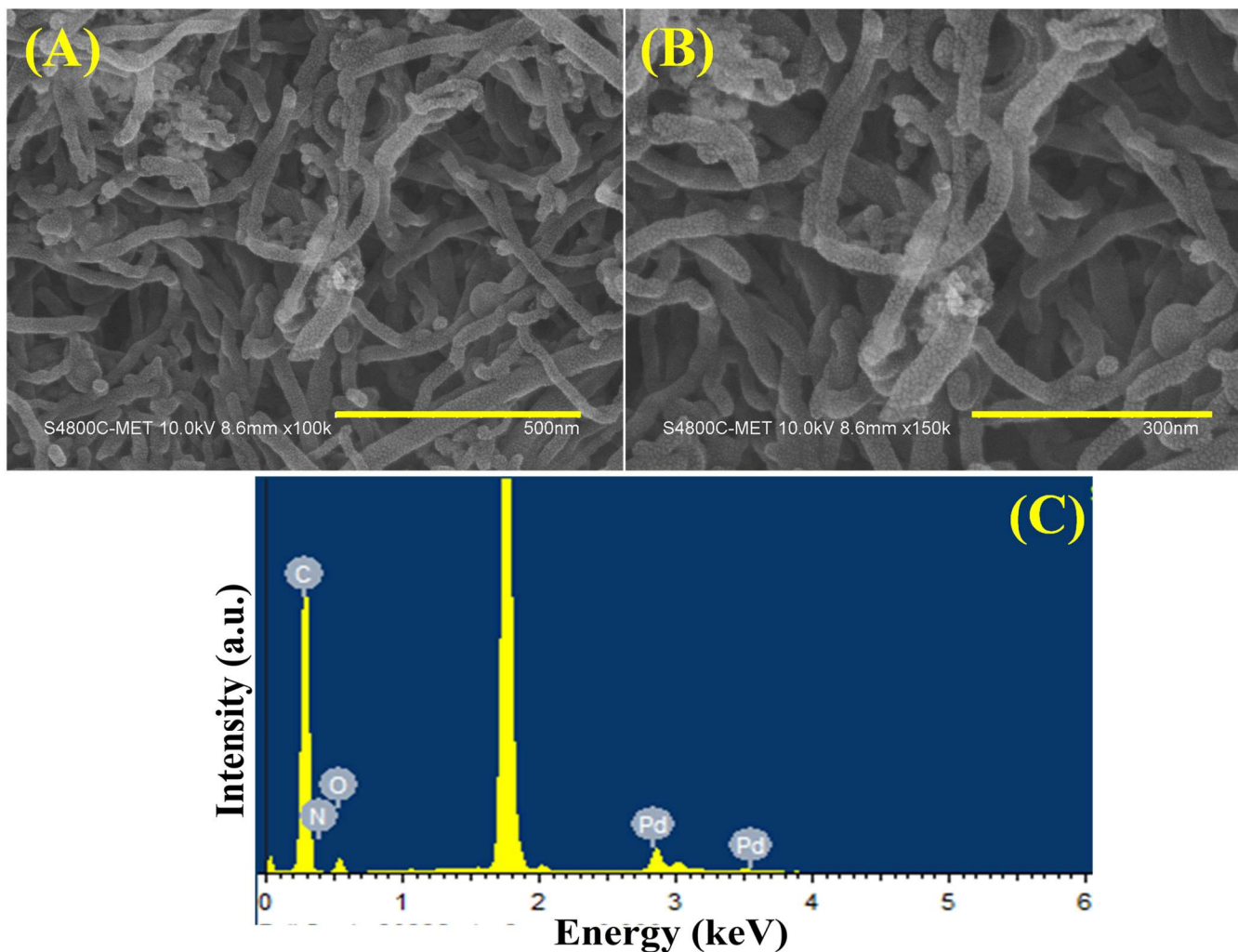
Fig. 3.4. (A and B) SEM images of Pd/NBCNT composite at different magnifications, and (C) EDS spectrum of Pd/NBCNT composite.
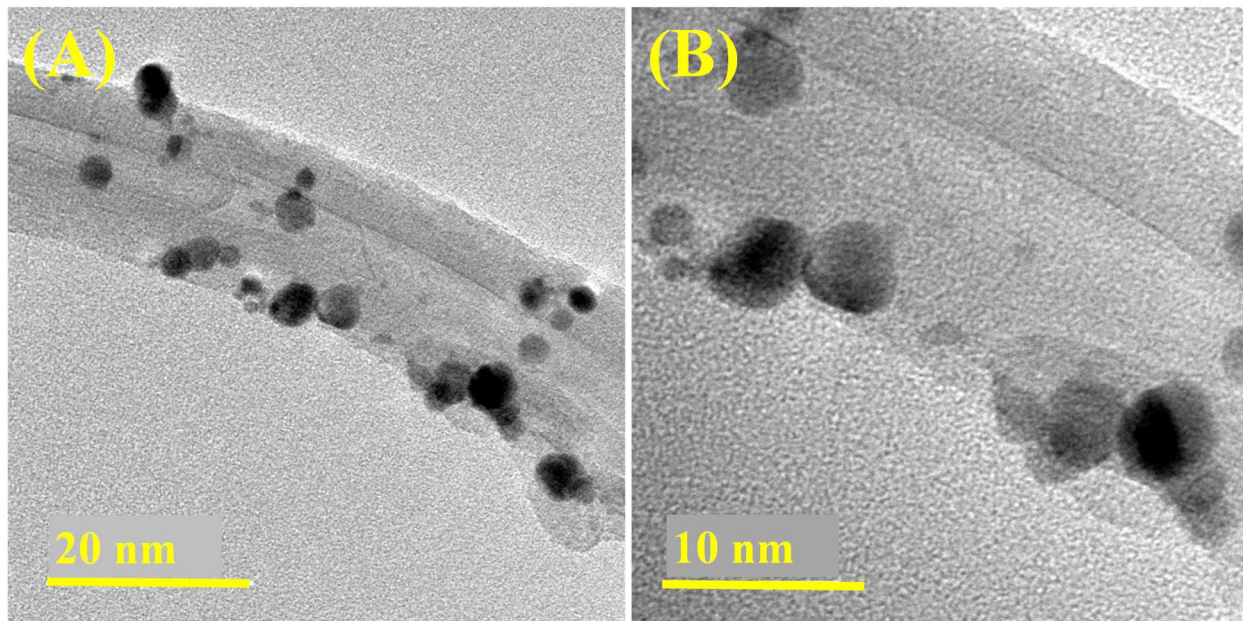
Fig. 3.5. (A and B) TEM images of Pd/NBCNT composite at different magnifications.

Figure 3.4 (A and B) shows the SEM images of Pd/NBCNT of different magnifications along with EDS elemental analysis. The SEM images depict clearly that CNTs have tangled, smooth rope like structures with Pd nanoparticles spread homogeneously on the side walls of the carbon nanotubes. Furthermore, the chemical composition of the synthesized Pd/NBCNT composite was elucidated by the help of energy-dispersive X-ray spectroscopy (EDS) analysis as shown in Fig. 3.4 (C). The peaks of Pd, C, N and O were detected, which infer that the composition of Pd/NBCNT electrocatalyst was accorded with the composition of elements present in the composite.

Figure 3.5 (A and B) shows TEM images of Pd/NBCNT electrocatalyst at different magnifications. It can be observed from the TEM images that well-dispersed, spherical particles of Pd are embedded onto the outside walls of NBCNTs. The average particle size is about 5.7 ± 0.5 nm, which is reliable with that estimated from XRD analysis. Although the Pd particles are of very small size, there were no or little aggregation of nanoparticles seen on the side walls of the CNTs. It is significantly due to the availability of large number of nucleation centers for the binding of Pd on the surface of the NB functionalized CNTs.

X-ray photoelectron spectroscopy (XPS) was employed to investigate the elemental composition of Pd/NBCNT and Pd/CNT composites (Fig. 3.6), and the deconvolution spectra of the composites were explored to evaluate the structural, chemical or electronic characteristics of the elements present in the synthesized electrocatalysts. In the survey spectra of Pd/NBCNT and Pd/CNT (Fig. 3.6(A)), it is evident that the N 1s peak was present in Pd/NBCNT whereas the same was not observed in Pd/CNT electrocatalyst. High resolution XPS spectra of C, N and Pd elements of Pd/NBCNT are shown in Fig. 3.6 (B-D), along with the deconvoluted spectrum of these elements. The deconvolution spectrum of C (Fig. 3.6 (B)) exhibited four distinct regions with the peak values of 284.44, 284.68, 285.50 and 289.21 eV, corresponding to C=C, C-C, C-N and O-C=O C atoms, respectively [219]. In Fig. 3.6(C), clearly only one peak is seen in the deconvoluted spectrum of N 1s with the peak value of 399.40 eV, and it could be straightly ascribed to the N atom of nitro group. It is clearly evident from the observation that the molecular doping had occurred on the surface of CNT with NB molecules. XPS spectrum of Pd 3d of Pd/NBCNT catalyst is shown in Fig. 3.6(D). XPS high resolution spectrum of Pd 3d along with deconvolution seen in Fig. 3.6(D) exhibits two distinct peaks associated with $3d_{5/2}$ and Pd $3d_{3/2}$, and the deconvolution has given two photoelectron peaks for each $3d_{5/2}$ and Pd $3d_{3/2}$ regions. The deconvoluted peaks of Pd $3d_{5/2}$ and Pd $3d_{3/2}$ centered at 335.26 and 340.52 eV, respectively, were ascribed to metallic Pd^0. The other two deconvoluted photoelectron peaks of Pd $3d_{5/2}$ and Pd $3d_{3/2}$ at 336.55 and 342.51 eV, respectively, could be ascribed to Pd^{II} of PdO [75,220,226]. As of the deconvoluted spectral peaks, it could be well ascertained that the photoelectron peaks of Pd^{II} was of low intensity compared to metallic Pd and that thus Pd exists in Pd^{II} oxidation state only to a very low extent. This observation signifies that the Pd metal had been reduced almost completely in Pd/NBCNT catalyst and that Pd^{II} could have occurred only to a least extent as PdO most likely in the exteriors of nanoparticles.
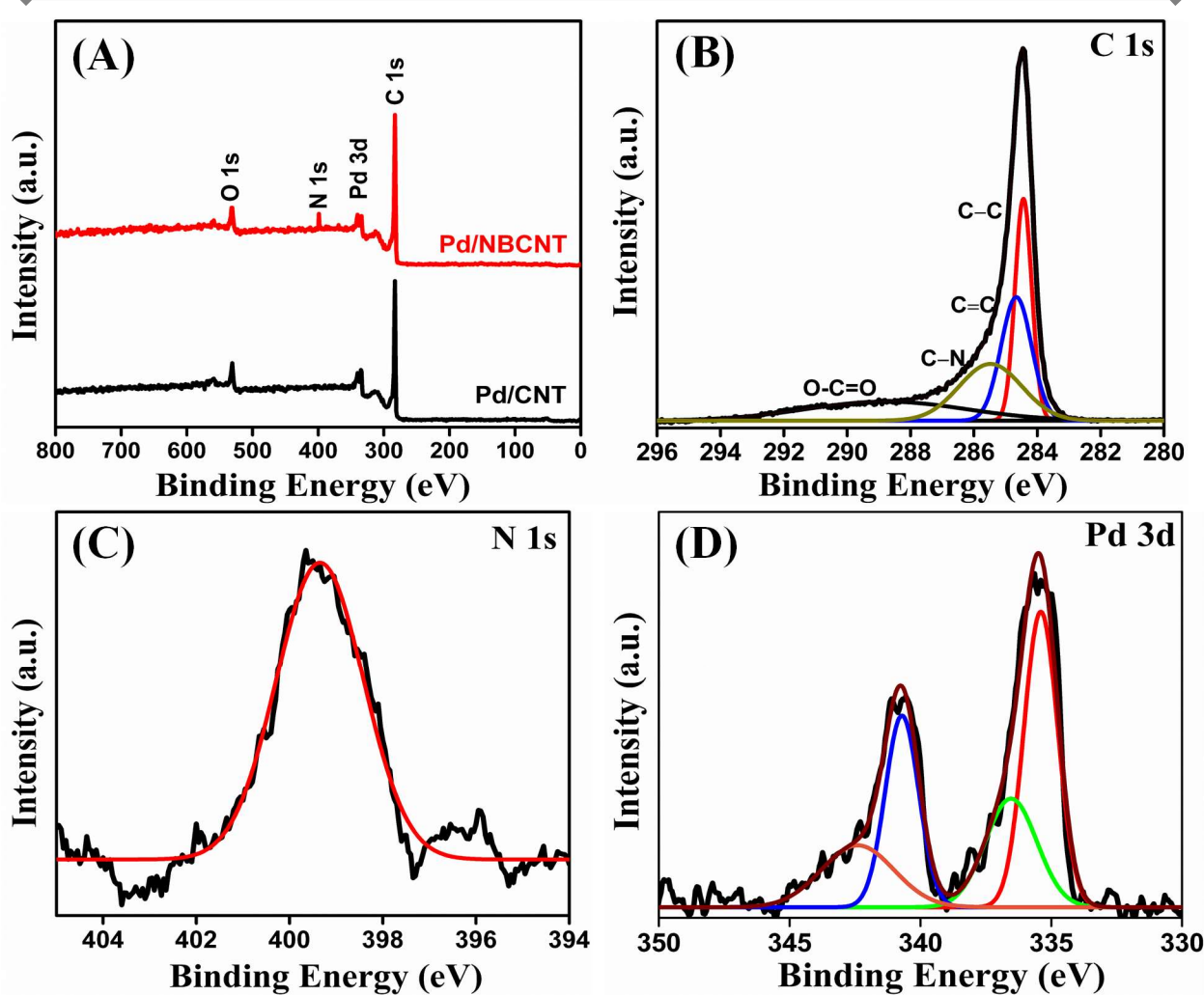
Fig. 3.6. (A) XPS survey spectrum of Pd/CNT and Pd/NBCNT composites, and (B-D) high-resolution spectra of Pd/NBCNT composite along with deconvoluted peaks in (B) C 1s, (C) N 1s and (D) Pd 3d regions.

In order to cross check the mass fraction of Pd in the synthesized Pd/NBCNT electrocatalyst, thermogravimetric analysis (TGA) was carried out for Pd/NBCNT catalyst with 10 ℃/min ramp rate in O_2 atmosphere as shown in Fig. 3.7. The TGA profile depicts the mass variation of Pd/NBCNT with the temperature increase. The weight loss resulted in the region of 300 to 750 ℃ is due to the loss of carbon support from the catalyst, Pd/NBCNT, as decomposed to carbon dioxide [227,228]. At the end of 900 ℃, the TGA profile of Pd/NBCNT retained 19.85 wt % of the catalyst correlated to the Pd content of the catalyst, which is totally equal to the actual 20 wt % Pd loading employed in the synthesis of the electrocatalyst.
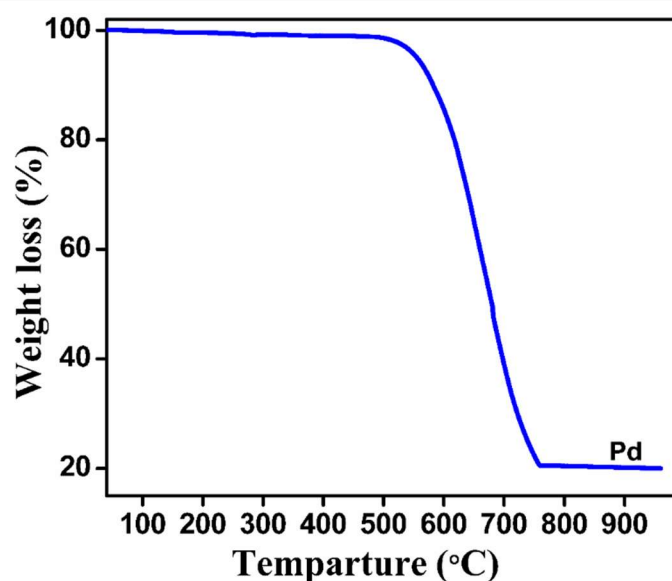
Fig. 3.7. Thermogravimetry (TGA) contour of Pd/NBCNT nanocomposite.

3.3.2. Electrochemical active surface area (EASA) and electrocatalytic oxidation of methanol

Catalytic performance of the synthesized electrocatalysts would depend on the electronic as well as geometrical properties of the composites. In order to determine the EASA of the fabricated Pd/C, Pd/CNT and Pd/NBCNT electrodes, cyclic voltammograms (CVs) were recorded in 0.5 M NaOH in the absence of CH_3OH at a scan rate of 50 mV s^{-1} and were shown in Fig. 3.8 (A). EASA of the fabricated electrodes have been determined by measuring the coulombic charge (Q) absorbed for PdO reduction during the second sweep segment of the CVs. EASA values were obtained with the help of a standard equation, EASA = Q/(S.l), where 'S' denotes the proportionality constant that relates coulombic charge with active surface area and 'l' indicates the catalyst loading in 'g.' A proportionality constant of 405 μC cm^{-2} was estimated for the reduction of PdO monolayer from the literature [203,229,230]. The calculated EASA values are given in Table 1, and the results infer that the Pd/NBCNT composite electrode exhibited higher EASA value of 78.54 m^2 g^{-1}, when compared with Pd/CNT and Pd/C electrocatalysts. The higher EASA of Pd/NBCNT electrode against Pd/CNT electrode and as much as four times higher against Pd/C electrode could be attributed to both more even distribution of the Pd nanoparticles on the NB doped CNT surface with no agglomeration and the smaller size of the Pd nanoparticles in the Pd/NBCNT composite.
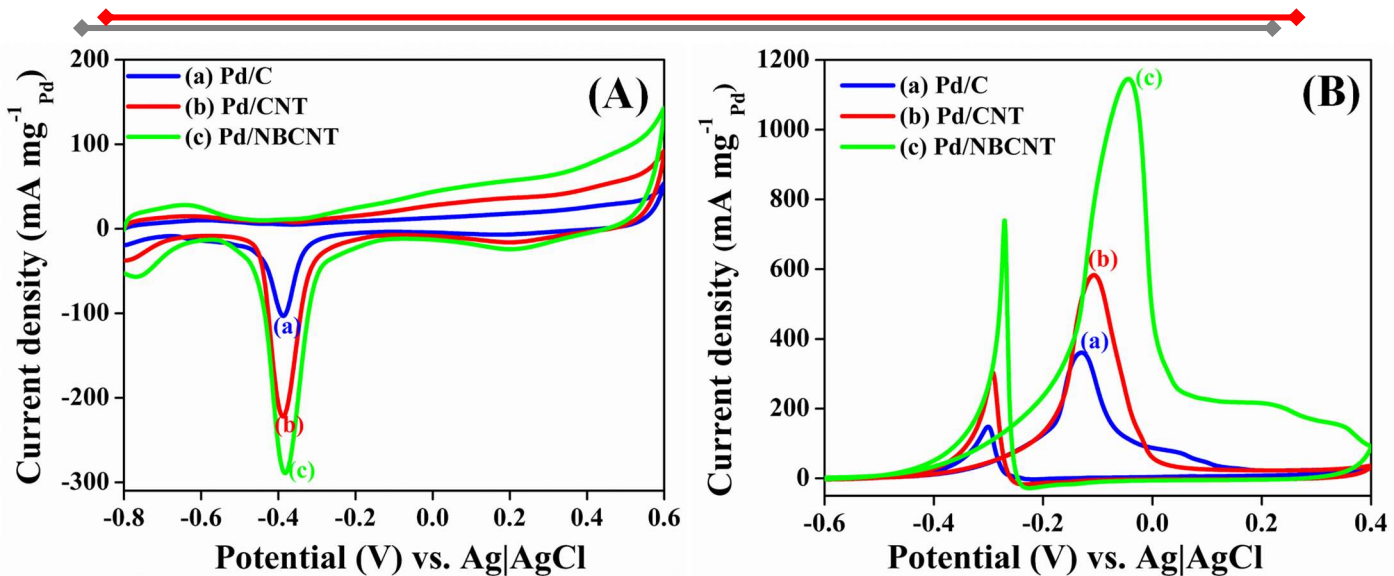
Fig. 3.8. (A) CVs of (a) Pd/C, (b) Pd/CNT and (c) Pd/NBCNT composite electrodes in 0.5 M NaOH at a scan rate of 50 mV s^{-1}. (B) CVs of (a) Pd/C, (b) Pd/CNT and (c) Pd/NBCNT composite electrodes in 0.5 M NaOH + 1 M CH$_3$OH at a scan rate of 50 mV s^{-1}.

Electrocatalytic activities of Pd/C, Pd/CNT and Pd/NBCNT electrocatalysts toward MOR were explored by CV measurements in 0.5 M NaOH + 1 M CH$_3$OH at 50 mV s^{-1} scan rate, and the resultant CVs are seen in Fig. 3.8 (B). The results have shown that all the synthesized electrocatalysts were active toward MOR in alkaline medium. Electrooxidation of CH$_3$OH at the modified electrodes exhibits two oxidation peaks, first one in the forward and the second one in the reverse scan. The peak observed during the forward scan represents the oxidation of both CH$_3$OH molecules chemisorbed and those driving to the surface of the modified electrode from solution. The anodic peak obtained in the backward scan could be ascribed to the oxidation of CH$_3$OH freshly adsorbed on the electrode surface along with the CH$_3$OH molecules diffusing to the electrode from solution [231]. It is observed that the electrocatalytic activity of Pd/NBCNT electrode was considerably higher compared to the other nanocomposite electrodes, Pd/CNT and Pd/C.

.In order to compare their relative electrocatalytic activities, two important factors play major roles, where one is the onset potential and the other one is the oxidation peak current. It is observed that the onset potential of Pd/NBCNT was relatively more negative when compared to that of Pd/CNT (Table 3.1). The specific mass current density for methanol oxidation at Pd/NBCNT (1143.9 mA mg^{-1}$_{Pd}$) is nearly two times higher than that obtained at Pd/CNT electrode

(582.8 mA mg^{-1}$_{Pd}$). In order to discuss and compare the electrocatalytic activities of different electrodic materials, it is much more suitable to compare the coulombic charge of the electrodic process rather than the peak current. The coulombic charge for methanol oxidation at Pd/NBCNT electrode, 2071.42 mC mg^{-1}$_{Pd}$, is nearly more than 2.5 times higher than that at Pd/CNT electrode, 804.62 mC mg^{-1}$_{Pd}$. The electrocatalytic methanol oxidation with Pd nanoparticles supported on NBCNT showed enhanced electrocatalytic activity due to the molecular doping of NB on to the surface of CNT. In overall, NB doping proved an advantageous technique to enhance the overall performance of Pd electrocatalysts supported on CNTs.

Table 3.1. EASA and electrocatalytic activities of the synthesized composites.

Catalyst	EASA (m^2 g^{-1}$_{Pd}$)	Peak potential E$_p$ (V)	Onset potential E$_{op}$ (V)	Specific mass current density (mA mg^{-1}$_{Pd}$)	Q$_f$ (mC mg^{-1}$_{Pd}$)
Pd/C	20.80	-0.12	-0.36	360.3	384.45
Pd/CNT	57.22	-0.10	-0.42	582.8	804.62
Pd/NBCNT	78.54	-0.04	-0.53	1143.9	2071.42

3.3.3. Chronoamperometry studies of methanol oxidation

Improved durability of the electrocatalysts is one of the significant factor for real-life fuel cell applications. Long-time steady state electrocatalytic activities of Pd/NBCNT and Pd/CNT electrocatalysts were analyzed by chronoamperometry studies. Steady-state amperometric i-t analysis has been carried out at a working potential of – 0.1 V in aqueous solution of 0.5 M NaOH + 1 M CH$_3$OH at room temperature under N$_2$-saturated environment, and the results are shown in Fig. 3.9. It is observed that the steady-state current density of Pd/CNT catalyst decayed very rapidly with time and reached very minimum within a short time, while that of Pd/NBCNT electrocatalyst endured a longer time. The steady-state current density of Pd/CNT electrode was reduced to 200 mA mg^{-1}$_{Pd}$ within 25 s, while that of Pd/NBCNT electrode endured a longer time

and was above 200 mA mg^{-1}$_{Pd}$ up to 625 s. For the steady-state electrocatalytic MOR in 2000 s, the total coulombic charge passed through Pd/CNT electrode was 65.5 C mg^{-1}, while that passed through Pd/NBCNT electrode was nearly 7 times higher, 405.9 C mg^{-1}. It is also identified that the current density of Pd/NBCNT was higher than Pd/CNT composite through the entire time scale range. All the observations clearly inferred that the electrocatalytic activity of Pd/NBCNT based on NB molecular doping had been enhanced tremendously compared to the functionalized CNT based Pd/CNT electrode. Furthermore, it could be suggested that the molecular doping with the strong electron-withdrawing nitro group had well promoted the electronic interactions in Pd/NBCNT catalyst between the Pd nanoparticles and the CNT support.
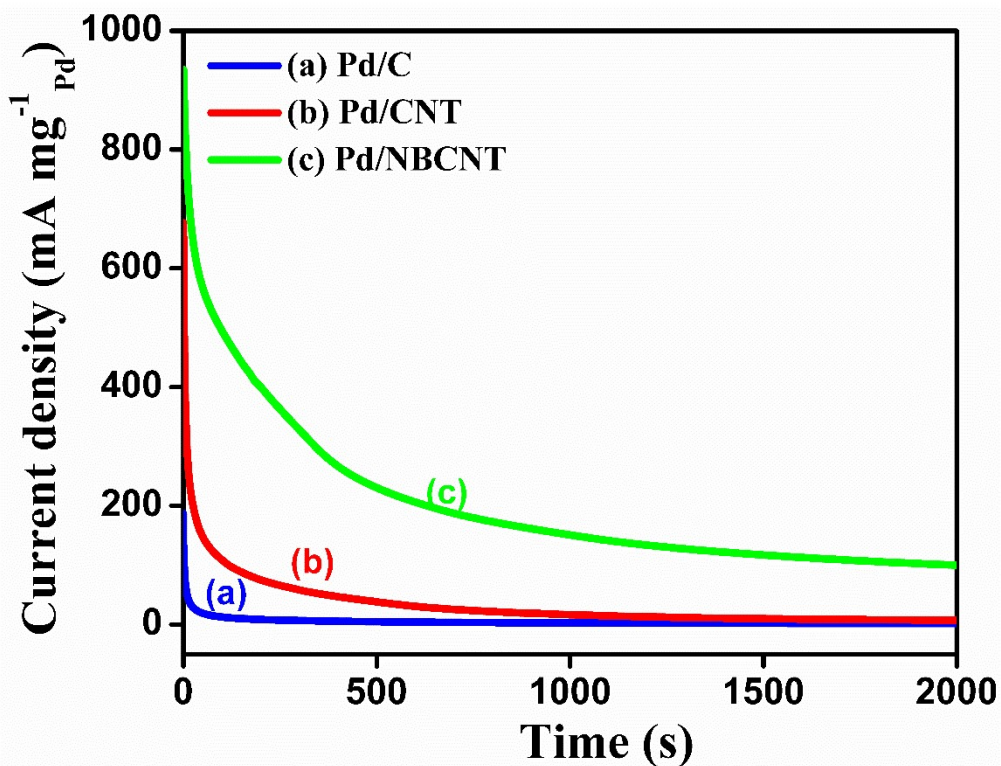
Fig. 3.9. Chronoamperometry (CA) measurements of (a) Pd/C, (b) Pd/CNT and (c) Pd/NBCNT composite electrodes in 0.5 M NaOH + 1 M CH$_3$OH at – 0.1 V.

3.4. Conclusions

In this chapter, we have described a method to prepare Pd nanoparticles supported on non-covalent functionalized CNT. The synthesis procedure is simple and could be easily carried out in lab scale and also without the use of expensive chemicals. Various instrumental methods, XRD, UV-Vis, Raman analysis, TEM and XPS, used for the characterization of the electrocatalysts revealed that the Pd nanoparticles associated with NBCNT support were very much smaller in size compared to the control catalysts, Pd/CNT and Pd/C. Electrochemical studies using cyclic voltammetry in alkaline medium revealed that Pd/NBCNT electrocatalyst possessed the largest EASA. Analysis on the electrooxidation of CH_3OH with the use of Pd/NBCNT electrocatalyst exhibited much enhanced specific mass activity, when compared to Pd nanoparticles supported on covalently functionalized CNT and carbon. Chronoamperometric investigations also revealed that Pd/NBCNT exhibited maximum initial specific mass current density and also limiting specific mass current density. From chronoamperometry investigations, the steady-state current density of Pd/CNT electrode was found to be reduced to 200 mA mg^{-1}_{Pd} within 25 s, while that of Pd/NBCNT electrode endured a longer time period of up to 625 s. All these results inferred that Pd nanoparticles supported on NBCNT (Pd/NBCNT) is highly efficient for MOR.

Chapter 4

One-pot Synthesis of $Pd_{20-x}Au_x$ Nanoparticles Embedded in Nitrogen Doped Graphene as High-Performance Electrocatalysts Toward Methanol Oxidation

4. One-pot Synthesis of $Pd_{20-x}Au_x$ Nanoparticles Embedded in Nitrogen Doped Graphene as High-Performance Electrocatalysts Toward Methanol Oxidation

4.1. Introduction

Clean energy initiatives are progressively important due to the growing global population and energy demands, overcoming the adverse effects of fossil fuels, like atmospheric pollution, greenhouse effect, global warming and adverse impact on public health [181]. Among the green technologies, direct methanol fuel cells (DMFCs) are the key for future green electrochemical energy sources to electrical automobiles and portable electronic devices, because of its unique advantages like excessive energy densities, low operational temperatures, near-zero pollutant emissions and liquid fuel feed [179,188]. From past two decades, Pt has been employed as active catalytic component for electrode material in DMFC assembly [184]. Unfortunately, poor abundance, high cost and inactivation of Pt by CO adsorption during MOR were challenging aspects for practical applications [182]. Later Pd came into action to overcome these problems even though less cost-effective but the abundance is fifty times higher than Pt, and its salient features are equivalent electrocatalytic activity and less susceptible to the reaction intermediates [232,233]. In order to further increase the electrocatalytic performances of Pt or Pd based catalysts in fuel cell applications, combinations with a secondary metal (Cu, Ni, Ru, Au, Ag, Cu, Co etc.) [95,210,229,234–236], metal oxides (CeO_2, MnO_2, SnO_2) [29,68,77,237–240], $CoWO_4$ [241] and chalcogenides ($MoSe_2$, MoS_2, Ag_2Se) [28,242–245] have been explored for cost effectiveness and synergistic interaction with Pt or Pd. These secondary metals, metal oxides or chalcogenides play a synergistic role as they attract the oxygen-containing species and eventually help in oxidizing the deactivating CO intermediate [8-26]. This phenomenon tends to increase the long-time reactivity and durability of the electrocatalyst by decreasing the poisoning effect.

Metal nanoparticles tend to aggregate and exhibit poor dispersion in the absence of solid supports, leading to a decrease in the effective surface area and electrocatalytic activity. Therefore, a series of diversified carbon materials have been employed as solid supports, like carbon nanotubes [246–248], carbon nanofibers, carbon microspheres [249–252] and graphene [92,232,253–255]. Among the carbon supports, graphene, 2-dimensional carbon nanostructure, has attracted great interest because of its high chemical stability, cost effectiveness, unusual mechanical properties and huge surface area, which all promoted its exploration in the fields of fuel cells, supercapacitors,

sensors and batteries. Doping of nitrogen into the lattices of graphene matrix would assist in intensifying the donor properties of the materials by the conjugation of carbon π electrons with the nitrogen lone pair. To embed nitrogen atoms into the matrix of graphitic materials, several methods have been explored like arc discharge [256], supramolecular aggregate with melamine [257], thermal annealing under NH_3 atmosphere [258,259] and solvothermal reactions employing $NH_3.H_2O$ [260]. These active sites would anchor the metal nanoparticles thereby increasing the uniform distribution of nanoparticles in the matrix with enhanced electron-transfer characteristics. Enhanced electrocatalytic activity was observed for N-doped graphene and graphitic carbon nitride (gC_3N_4) based metal nanocomposites over non-doped graphene composites in various types of fuel cells [261,262]. Nitrogen-doped low-defect graphene and hybrid composites of low-defect carbon nanotubes were found to enhance the electrocatalytic activity toward MOR [259,260]. Palladium nanoparticles anchored onto gC_3N_4-carbon black hybrid exhibited a highly enhanced electrocatalytic activity for MOR with a current response of 1720 mA mg^{-1} [262]. Similarly, Pd nanoparticles anchored onto gC_3N_4-rGO hybrid exhibited an enhanced peak current response of 1550 mA mg^{-1} [261]. In order to tap a synergistic effect of oxygen-interacting metal Au, a number of research investigations were explored [226,263,264]. Core-shell type catalysts like AuPd@Pd dispersed on graphene has shown a current density of 650 mA mg^{-1} [226]. Hollow and solid PdAu nanocrystals bound to electrode surface were found to exhibit peak current responses of 405 and 492 mA mg^{-1}, respectively [263,264].

In this chapter, we focused on the development of mixed $Pd_{20-x}Au_x$ (x = 0, 5, 10 and 15) bimetallic catalysts anchored onto N-doped graphene to tap the synergistic effect of Pd and Au along with enhanced electronic interactions from NG180 toward MOR. A simple hydrothermal polyol method involving simultaneous reduction of Pd and Au in presence of the solid support, N-doped graphene, without any surfactant has been employed, and it is anticipated to promote fine dispersion of metal nanoparticles, enhanced electronic interactions with the solid support and thus efficient electrocatalytic activities toward MOR. It was observed that the substitution of Pd by Au always exhibited higher electrocatalytic currents, low over potentials and low onset potentials toward MOR at all the compositions compared to Pd alone. The stability, enhanced reactivity, CO tolerance and long-time durability of the PdAu/NG180 composites for MOR were established.

4.2. Experimental

4.2.1. Chemicals

Graphite nanopowder, $NaNO_3$, $KMnO_4$, 30% H_2O_2 and hydrazine hydrate were of analytical grade obtained from SRL, India. $HAuCl_4$, ethylene glycol (Sisco Research Laboratories SRL), palladium (II) chloride were acquired from Sigma Aldrich. All other compounds employed were of high purity (> 99.5 %). Ultrapure water of high resistance (18.2 Mohm) drawn from water purifier (Smart2Pure, Thermo Scientific, Hong Kong) was used during the analyses.

4.2.2. Syntheses of NG180

Graphene oxide (GO) was synthesized from graphite nanopowder using modified Hummer's method with a set of modifications. In brief, 2 g graphite powder was added slowly to ice cold 40 mL conc. H_2SO_4 under constant stirring. Then, it was maintained in ice bath for the addition of $NaNO_3$. Further, $KMnO_4$ was slowly added and the temperature was continued at 20 ºC. Thereafter, the reaction mixture was raised to 60 ºC, and the contents were stirred vigorously for 4 h. Then the mixture was stirred at 90 ºC for 15 – 20 min with the addition of 100 mL water slowly. A change in the solution color to bright yellow with effervescence was observed on adding warm water (200mL) and 20 mL 30% H_2O_2 to the reaction mixture. The formed solid product was collected, washed multiple times with aq. 5 % HCl and water, and dried at 50 ºC for 10 h.

Synthesized GO was used for the synthesis of NG180 by hydrothermal method. In brief, 150 mg GO was dispersed in ultrapure water (100 mL) with the help of sonication for about 1 h, and the solution pH was made 11 by the addition of 25 % ammonia solution Thereafter, for simultaneous reduction and N doping, 5 mL hydrazine hydrate was added, and the contents were taken in a stainless steel autoclave having Teflon lining and were treated at 180 ºC for 4 h. Resultant N-doped graphene was washed several times with ultrapure water and dried at 70 ºC overnight. N-doped graphene is labeled as NG180, relating to the temperature that was used for the synthesis of N-doped graphene.

4.2.3. Syntheses of $Pd_{20-x}Au_x$/NG180 nanocomposites

One-pot polyol method was employed for the syntheses of PdAu/NG180 nanocomposites. In brief, 40 mg NG180 was dispersed in a mixture of 38 mL ethylene glycol and 12 mL isopropyl

alcohol (IPA) and sonicated for 2 h in order to obtain a homogeneous suspension. Simultaneously, solutions of respective metal salts containing fixed weight (wt) ratios of Pd and Au were prepared by dissolving $PdCl_2$ in dil. HCl and $HAuCl_4$ in water. $HAuCl_4$ precursor solution was added to the homogeneous NG180 suspension and sonicated for 2 h. Thereafter, solution of H_2PdCl_4 was added and sonicated for 60 min to allow the accumulation of both Pd and Au metal ions on the active sites of NG180 sheets. Then, the pH of the resultant solution was brought to 11 with the addition of 1 M NaOH and the reaction contents were heated at 140 ºC for 4 h in 100 mL Teflon lined SS autoclave. Reduction of Pd and Au metal ions would complete by the stipulated time period. Initially, Au nanoparticles tend to form as the reduction potential and temperature required for the formation of Au nanoparticles are less compared to that for Pd nanoparticle formation, as it requires 130 - 140 ºC. Ethylene glycol acts both as stabilizing and reducing agents in the formation of PdAu/NG180 nanocomposites. The black solid product was collected after allowing the autoclave to reach room temperature, washed several times with H_2O and ethanol, and dried at 60 ºC for 10 h. The total metal content was maintained to 20 wt %. PdAu/NG180 nanocomposites have been prepared by varying the Pd:Au metal wt.% ratios as 20:0, 15:5, 10:10, 5:15 and 0:20, and they were labeled as $Pd_{20-x}Au_x$/NG180 (x = 0, 5, 10, 15 and 20).

4.2.4. Characterization

X-ray diffraction (XRD) spectra of graphite, GO, NG180 and synthesized hybrid nanocomposites were recorded by Bruker AXS D8 diffractometer with Cu K_α source (1.5406 Å), 2 mdeg step size and scan speed of 0.5 s per step. Raman spectra were recorded by micro-Raman spectrometer (HR800-UV Horiba Jobin Yvon, France) with the excitation source of 532 nm. Morphology of PdAu/NG180 composites were analyzed using FESEM (FEI Apreo LoVac) equipped with an Aztec Standard Energy Dispersive X-ray Spectroscopy (EDS) system - resolution 127 eV on Mn-K_α. For FESEM analysis, specimens were sprinkled on a stub containing carbon tape, followed by sputtering a thin layer of gold on the sample to prevent charging. XPS measurements were recorded by Physical Electronics (PHI 5000 VersaProbe III) spectrometer. Surface morphology of PdAu nanocomposites was studied using transmission electron microscopy (Tecnai G2 20 S-TWIN microscope) at 200 kV. The wt. % of metals present in the nanocomposites was analyzed by inductively coupled plasmon-optical emission spectrometer (ICP-OES 725ES, Varian, USA).

4.2.5. Electrochemical analysis

Electrochemical measurements were performed in a cell with a set of three electrodes using CHI workstation (Model 6132E, USA). Pt coil of 0.25 mm diameter wire (surface area 1.6 cm^2) acts as counter electrode, 3 mm diameter glassy carbon electrode (GCE) coated with the synthesized nanocomposites as working electrode and Hg|HgO (1 M NaOH) as reference electrode. At first, bare GCE was cleaned by polishing with (0.3 and 0.05 μm) alumina slurries and thereafter washed with water, C_2H_5OH and H_2O through sonication at each step and dried. The catalytic ink was made in order to fabricate the working electrodes by dispersing 2.5 mg $Pd_{20-x}Au_x$/NG180 electrocatalyst in 450 μL of 1:1 (v/v) IPA:H_2O mixture, and then 50 μL of 5 wt% Nafion in ethanol was added to the above mixture. 2 μL catalytic ink was drop casted onto GCE and allowed to dry under room temperature for 12 h. Loading of the $Pd_{20-x}Au_x$/NG180 composite on the electrode is calculated to be 0.14 mg cm^{-2}. Electrochemical performances of the fabricated electrodes toward MOR were analyzed by using 0.5 M NaOH + 1 M CH_3OH electrolyte solution after purging with high-purity nitrogen. All the electrode potentials were represented in this chapter against Hg|HgO electrode, unless otherwise specified.

4.3. Results and Discussion

4.3.1. Characterization of Nanocomposites

Synthesized $Pd_{20-x}Au_x$/NG180 composites were analyzed systematically to study their composition, crystallinity, surface morphology, particle size and electronic nature. Figure 4.1(A) presents the XRD spectra of graphite, GO and NG180, and all have shown a prominent XRD peak corresponding to the carbon (002) plane. For graphite, the sharp peak observed at 26.45º corresponds to the graphitic nature of carbon (002) plane. In the case of GO, the peak was shifted to 12.13º with broadening, and the inter-planar distance of (002) plane increased from 3.36 Å for graphite to 7.29 Å for GO. The synthesis of GO by modified Hummer's method introduces hydroxyl, carboxyl and epoxy functional groups, which all together increased the inter-planar distance in GO. In the case of reduced N-doped graphene (NG180), the carbon (002) peak is shifted back and centered at ~25º with a broad nature from 19º to 30º, reflecting the regain of graphitic nature and the formation of few-graphene layer structure [265]. The XRD analysis confirmed the conversion of GO to reduced N-doped graphene oxide successfully, and the presence of nitrogen

in NG180 sheets is corroborated by EDX analysis and elemental mapping of the nanocomposites (*vide infra*).
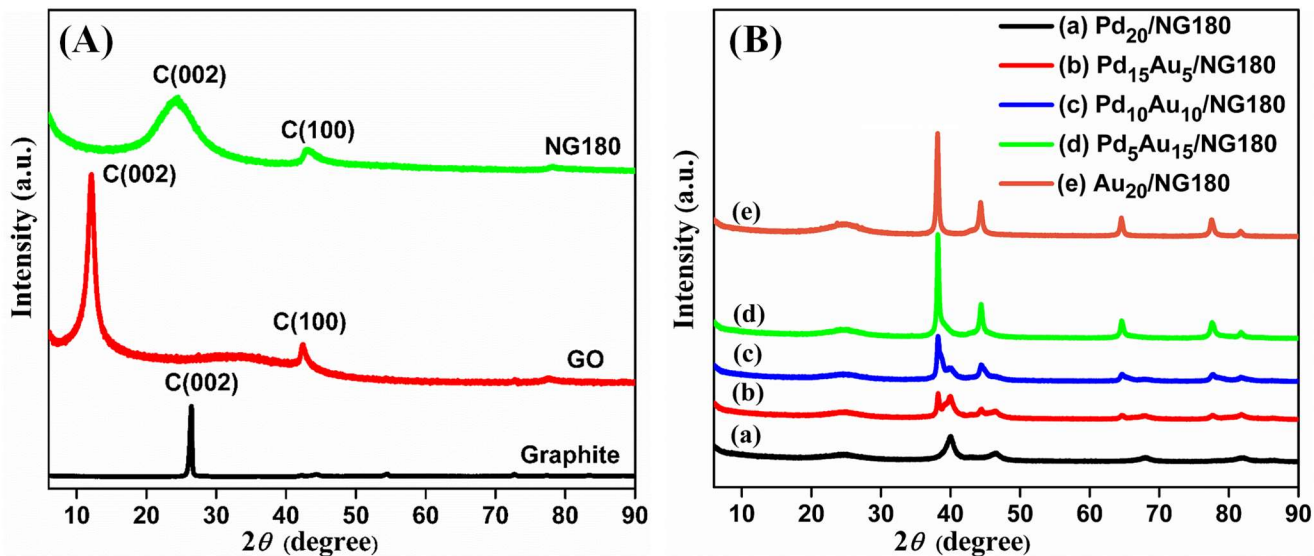
Fig. 4.1. (A) XRD patterns of graphite, GO and NG180. (B) XRD patterns of (a-e) $Pd_{20-x}Au_x$/NG180 composites (x = 0, 5, 10, 15 and 20).

XRD spectra of $Pd_{20-x}Au_x$/NG180 composites (Fig. 4.1 B) show the characteristic (111), (200), (220), (311) and (222) diffractions of face centered cubic (fcc) Pd (JCPDS No. 87-0638) [247] and Au (JCPDS No. 04-0784) [266]. The broad peak in all the spectra between 20º to 30º is due to the carbon (002) plane of NG180. In all the composites, diffraction peaks characteristic of both Pd and Au nanoparticles can be observed, illustrating the successful generation of bimetallic phases of Pd and Au at all the compositions. The prominent peaks observed at ~40.07º and ~38.20º correspond to the (111) planes of Pd and Au nanoparticles, respectively, specifying that both Pd and Au nanoparticles were oriented preferentially with (111) facet in the PdAu/NG180 nanocomposites. The average crystallite sizes are estimated by using Scherrer method. It is observed to be 20 nm and 6 nm for Au and Pd nanoparticles, respectively in Au_{20}/NG180 and Pd_{20}/NG180 nanocomposites. The weight percentage of Pd and Au in $Pd_{10}Au_{10}$/NG180 composite was determined by ICP-OES to be 9.11 and 8.05, respectively, and it is very close to the weight percentage of Pd and Au (10 wt. % each) employed for the synthesis of the composite. This observation confirmed the effective reduction of the metal ions taken completely into metallic nanoparticles of the composite and the possible attractive binding of the metal nanoparticles to the NG180 support.
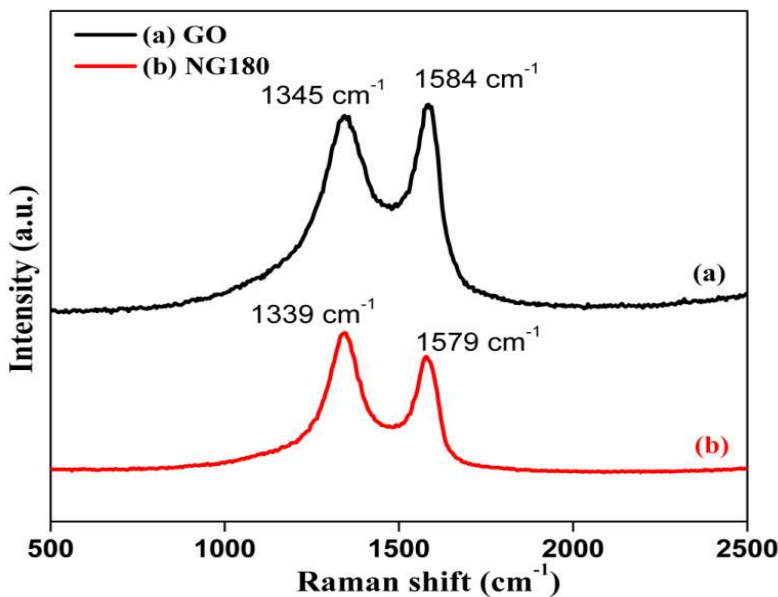
Fig. 4.2. Raman spectra of (a) GO and (b) NG180.

Raman spectroscopy is widely explored for the study of graphitic nature and defects of carbon based materials. Raman spectra of GO and NG180 are shown in Fig. 4.2 and were analyzed by identifying the two distinct peaks in GO and NG180, generally called as D-band (1345 cm^{-1}, 1339 cm^{-1}) and G-band (1584 cm^{-1}, 1579 cm^{-1}), respectively. The presence of G-band represents the first order scattering of E$_{2g}$ phonon of the respective parent precursor of graphitic carbon and explains the extent of graphitization, while the D-band represents the formation of structural defects and disorders which were confined to insertion of hetero-atoms into the NG180 planes and grain boundaries and indirectly accounts for the study of degree of oxidation. For NG180, it is noteworthy that the shift in G-band position from 1584 cm^{-1} to 1579 cm^{-1}, which is closer to the G-band position of graphite found in the literature [267]. The I$_D$/I$_G$ ratio of NG180 is identified to be 1.15 and is high compared to that of the synthesized GO, 0.97. This observation infers the successful insertion of nitrogen into the matrix of graphene sheets during the synthesis of NG180 by hydrothermal method. The presence of Pd, Au and C elements and the extent of N-doping and their distribution in the matrix of NG180 composites have been analyzed by EDX colour elemental mapping analysis, and the observed results are shown in Fig. 4.3. The distribution of all the elements together (Fig. 4.3 (a)) and individually (Fig. 4.3 (b-e)) are shown with the representation of each element with a different colour. Elemental mapping confirms the uniform distribution of Pd and Au nanoparticles, and C and N elements throughout the composite matrix.
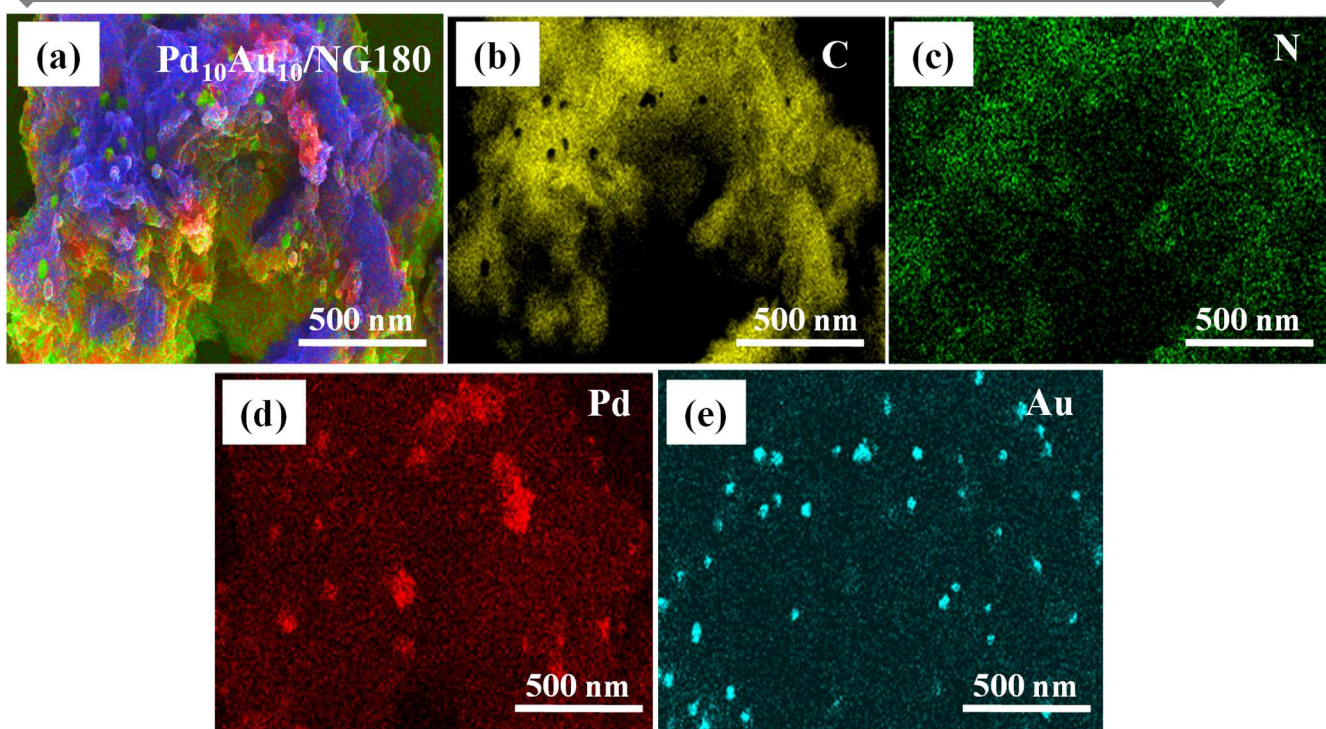
Fig. 4.3. EDX colour elemental mapping of $Pd_{10}Au_{10}$/NG180 nanocomposite, illustrating (a) the distribution of all the elements (C, N, Pd, Au) together, and distributions of individual elements (b) carbon, (c) nitrogen, (d) palladium and (e) gold.

TEM images of synthesized $Pd_{10}Au_{10}$/NG180 catalyst are shown in Fig. 4.4 (A-D). Clear sheet like structure of NG180 with the homogenous distribution of PdAu nanoparticles is firmly identified from the TEM images. The PdAu nanoparticles have been embedded uniformly onto NG180 sheets because of possible attractive interactions between the nanoparticles and N-doped sites present widely across the graphene support NG180. The average particles size was found to be ~4-6 nm from the TEM images of Fig. 4.4 (D). The uniform widespread distribution of PdAu nanoparticles onto NG180 matrices would facilitate in enhancing the electrocatalytic activity towards MOR.

Figure 4.5 shows the HRTEM image of $Pd_{10}Au_{10}$/NG180 composite and it shows the existence of different crystalline lattice fringes in close proximity to each other. The d-spacing in the nanoparticles were determined from the fringe patterns to be 0.23 and 0.20 nm [226,264] and the observed d-spacing values 0.23 and 0.20 nm are close to that of AuPd alloy, 2.30 Å [226] and (111) planes of Pd, 2.22 Å [264], respectively. The selective area electron diffraction (SAED) pattern clearly confirms the existence of fcc crystallinity (Fig. 4.5.), in accordance with the XRD results (*vide supra*).
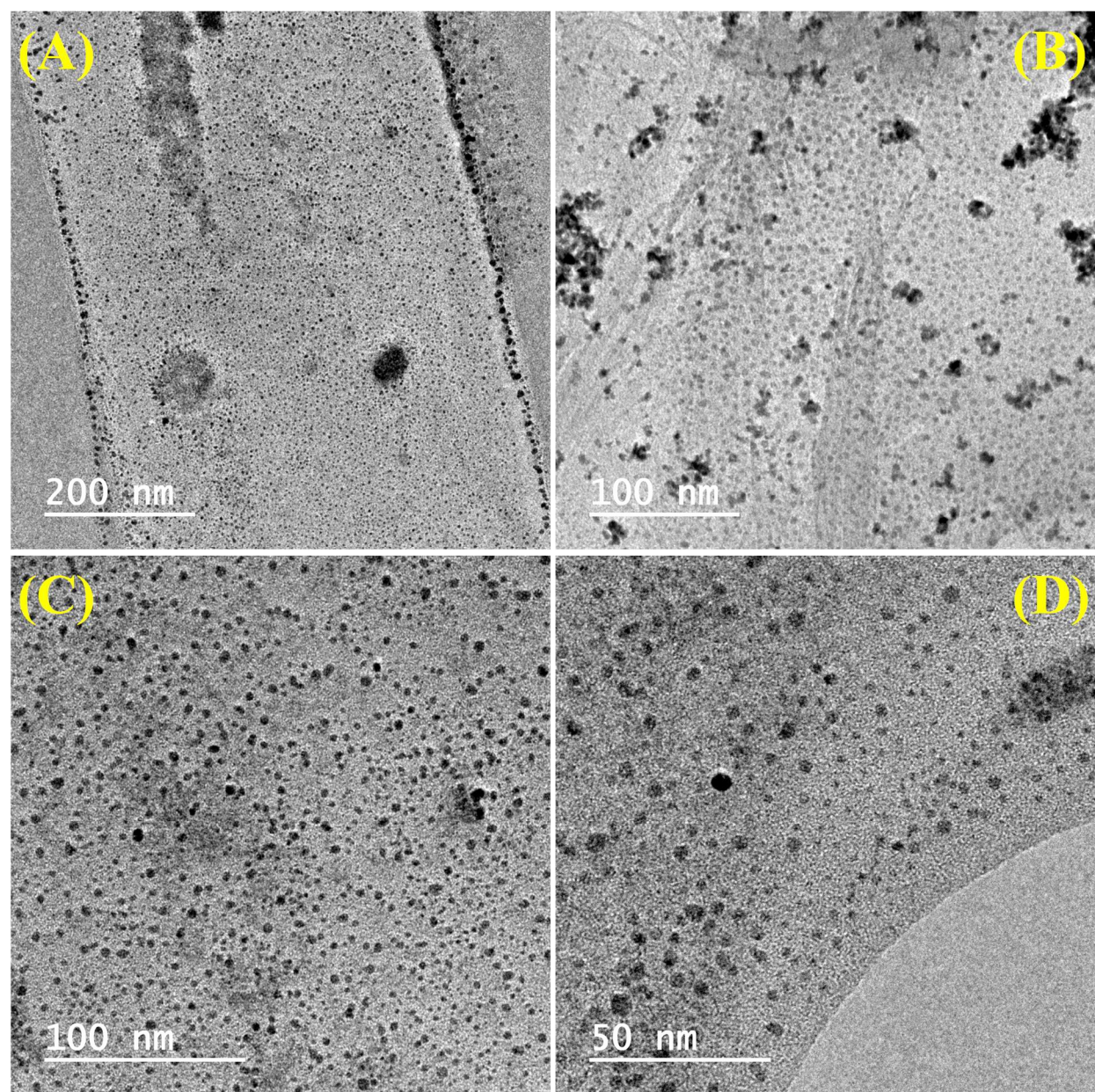
Fig. 4.4. TEM images of $Pd_{10}Au_{10}/NG180$ catalyst at different magnifications (A-D).
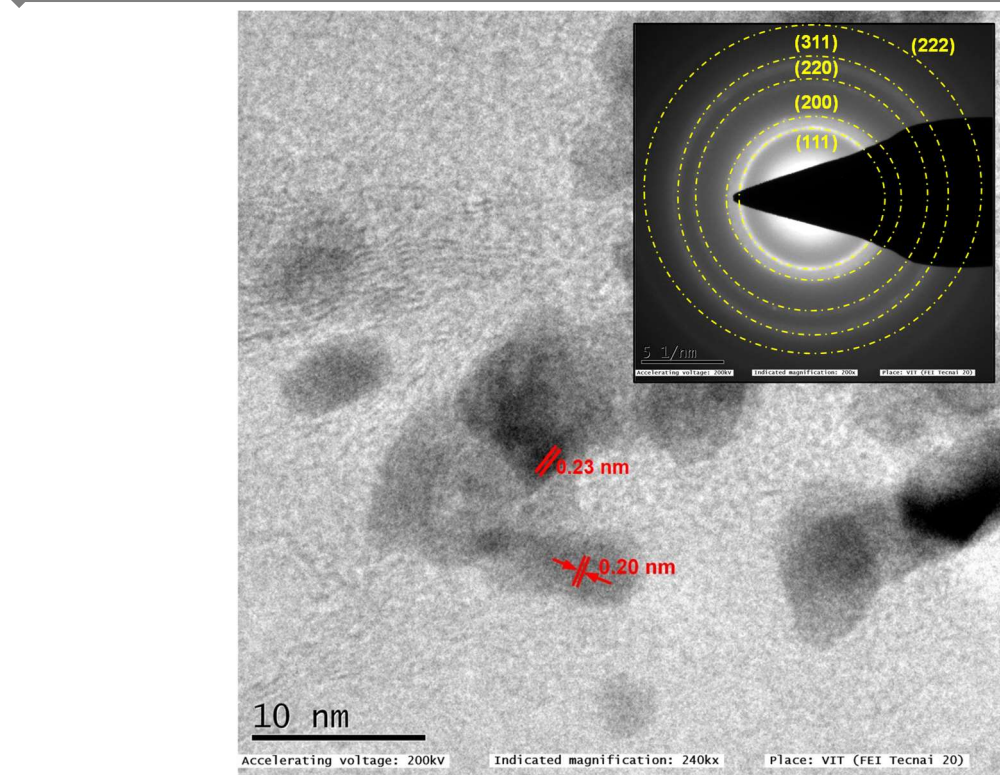
Fig. 4.5. HRTEM image of $Pd_{10}Au_{10}/NG180$ composites with inset showing the SAED pattern.

XPS studies were carried out to analyze the oxidation states and surface composition of the synthesized $Pd_{20}/NG180$ and $Pd_{10}Au_{10}/NG180$ nanocomposites. As shown in Fig. 4.6 (A), Pd, Au, C, O and N signals seen in the survey spectrum reveal the successful formation of (a) $Pd_{20}/NG180$ and (b) $Pd_{10}Au_{10}/NG180$ nanocomposites. High-resolution XPS spectra of Pd 3d and Au 4f regions of $Pd_{10}Au_{10}/NG180$ are shown in Fig. 4.6 (D and E). Two spin-orbit splitting peaks were observed for Pd 3d and represented as $3d_{3/2}$ and $3d_{5/2}$ [226]. The deconvoluted Pd 3d peaks of the electrocatalysts exhibits two peaks of Pd $3d_{5/2}$ and Pd $3d_{3/2}$ at 334.10 and 339.32 eV, respectively, ascribed to metallic Pd^0. The other two photoelectron peaks of Pd $3d_{5/2}$ and Pd $3d_{3/2}$ at 336.37 and 341.53 eV, respectively, could be ascribed to $Pd^{II}O$. XPS spectrum of Au 4f region of the catalyst shows two peaks at 82.36 and 86.23 eV of $4f_{7/2}$ and $4f_{5/2}$, respectively, attributed to Au^0, which confirms the successful formation of metallic Au. While Pd exists in two oxidation states Pd^0 and Pd^{II}, Au exists only as Au^0. This observation suggests the facile reduction of $AuCl_4^-$ to Au^0 occurred because of the reduction potential of $AuCl_4^-/Au$ (1.002 V), which is more positive than the reduction potential of Pd^{2+}/Pd^0 (0.591 V).
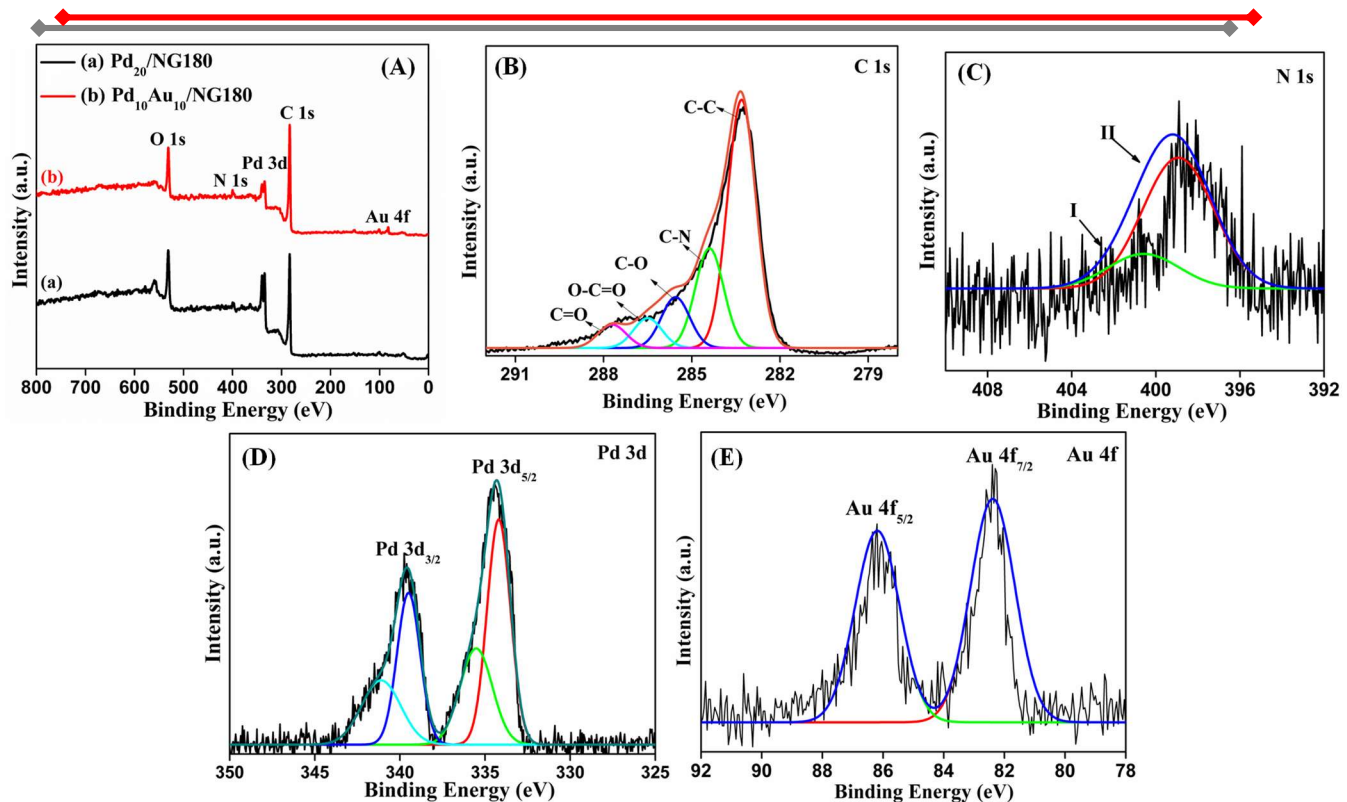
Fig. 4.6. XPS survey spectrum of (A) Pd/NG180 (a), $Pd_{10}Au_{10}$/NG180 (b), and (B-E) high-resolution spectra of $Pd_{10}Au_{10}$/NG180 in (B) C 1s, (C) N 1s, (D) Pd 3d and (E) Au 4f regions.

Figure 4.6 (B) shows the high resolution spectrum of C 1s region, which consists of the oxygen-containing functional groups such as C-N, C-C, O-C=O, C-O and C=O in NG180 nanocomposite with the corresponding deconvoluted peaks of C 1s at 284.44, 285.67, 286.66, 288.10 and 289.30 eV, respectively [268]. The C 1s peak at 285.67 eV suggests the existence of C-N bond in the matrix of the nanocomposites. The bonding nature of N in the matrix of NG180 catalyst was further analyzed by the high resolution N 1s XPS spectrum as shown in Fig. 4.6 (C) [267,269], which revealed an existence of two regions for nitrogen, labeled as region I and II. The region II at lower binding energy is pertinent to pyrrolic nitrogen, which contributes to the π system with one p electron. The other region I with a relatively higher binding energy is due to the quaternary nitrogen which was doped inside the NG180 layers. The nitrogen content in the prepared composites has been determined from XPS studies to be 1.78 at.%, equivalent to a few literature reports of N-doped graphenes [259,270] All these XPS analyses reveal the co-existence of Pd, Au in the N-doped graphene matrix (NG180) as we synthesized the $Pd_{20-x}Au_x$/NG180 composites.

4.3.2. Electrochemical active surface area (EASA)
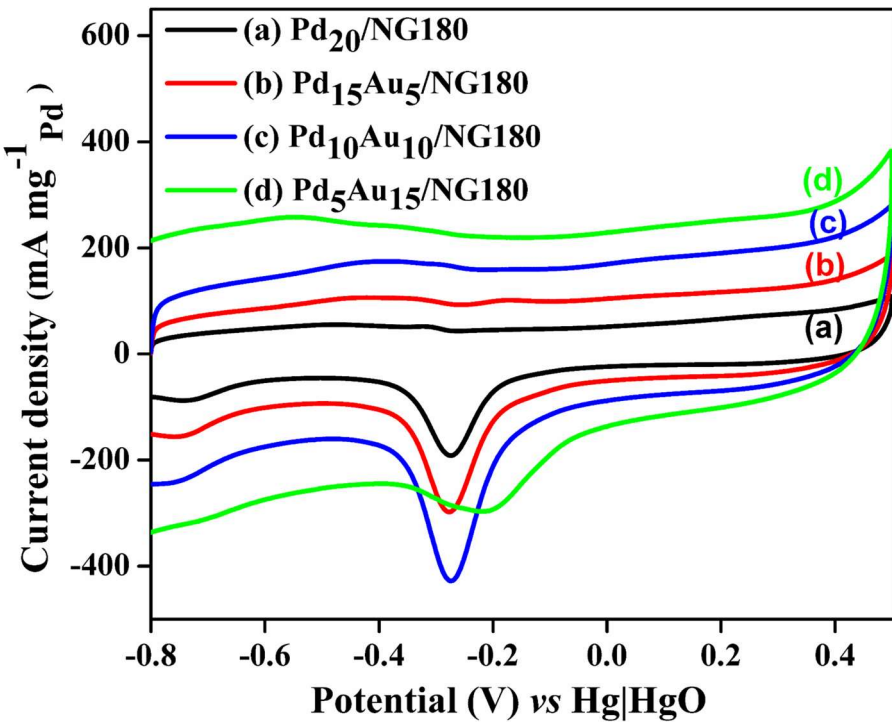
Fig. 4.7. CVs of (a) Pd20/NG180, (b) Pd15Au5/NG180, (c) Pd10Au10/NG180 and (d) Pd5Au15/NG180 modified electrodes in 0.5 M NaOH at a scan rate of 50 mV s^{-1}.

Catalytic performance of the synthesized electrocatalysts would depend on the electronic as well as geometrical properties of the composites. In order to know the electroactive surface area (EASA) of the Pd$_{20-x}$Au$_x$/NG180 electrodes, cyclic voltammograms were recorded in 0.5 M NaOH in the absence of CH$_3$OH with a scan rate of 50 mV s^{-1} and were shown in Fig. 4.7. EASA of the fabricated electrodes have been determined by measuring the coulombic charge (Q) for PdO reduction during the second sweep segment of the CVs (Fig. 4.7). EASA values were obtained with the help of an equation, EASA = $Q/(S \cdot l)$, where 'S' denotes to the proportionality constant that relates coulombic charge with active surface area and 'l' indicates the catalyst loading in 'g.' A coulombic charge of 405 μC cm^{-2} was estimated for the reduction of PdO monolayer from the literature [211,229]. The calculated EASA values are given in Table 1, and the results infer that the presence of Au along with Pd in the composite always increased the EASA of Pd. Pd10Au10/NG180 exhibited the highest EASA value of 50 m^2 g^{-1}Pd, and EASA of the electrocatalysts decreased as follows: Pd10Au10/NG180 > Pd15Au5/NG180 > Pd5Au15/NG180 > Pd20/NG180.

4.3.3. Electrocatalytic oxidation of methanol

Electrocatalytic activities of $Pd_{20-x}Au_x$/NG180 (x = 0, 5, 10 and 15) nanocomposites toward MOR were explored by CV measurements in 0.5 M NaOH + 1 M CH_3OH at 50 mV s^{-1} scan rate, and the resultant CVs are seen in Fig. 4.8. The results emphasized that all the synthesized electrocatalysts were active toward MOR in alkaline medium. Electrooxidation of methanol at $Pd_{20-x}Au_x$/NG180 electrodes exhibits two oxidation peaks, first one in the forward and the second one in the reverse scans. The peak observed during the forward scan represents the oxidation of CH_3OH molecules chemisorbed and those driving to the surface of the modified electrode from solution. The anodic peak obtained in the backward scan could be ascribed to the oxidation of CH_3OH freshly adsorbed on the electrode surface along with the CH_3OH molecules diffusing to the electrode from solution [271]. It is observed that the electrocatalytic activity of $Pd_{10}Au_{10}$/NG180 catalyst is considerably higher compared to the other nanocomposites. From Fig. 4.8 (c and d), it was observed that both $Pd_{10}Au_{10}$/NG180 and Pd_5Au_{15}/NG180 electrocatalysts exhibit the lowest onset potentials compared to Pd_{20}/NG180 and $Pd_{15}Au_5$/NG180 electrocatalysts. The specific mass current density, EASA and the onset potential (E_{op}) toward methanol oxidation of all the modified electrodes are presented in Table 1.

Table 4.1. EASA and electrocatalytic activities of $Pd_{20-x}Au_x$/NG180 composites.

Catalyst	EASA (m^2 g^{-1}_{Pd})	Onset potential E_{op}		Specific mass current density (mA mg$^{-1}_{Pd}$)
		(V vs. Hg|HgO)	(V vs. RHE)	
Pd_{20}/NG180	23	$-$ 0.58	0.369	985
$Pd_{15}Au_5$/NG180	36	$-$ 0.69	0.259	1333
$Pd_{10}Au_{10}$/NG180	50	$-$ 0.72	0.229	1510
Pd_5Au_{15}/NG180	24	$-$ 0.73	0.219	1086
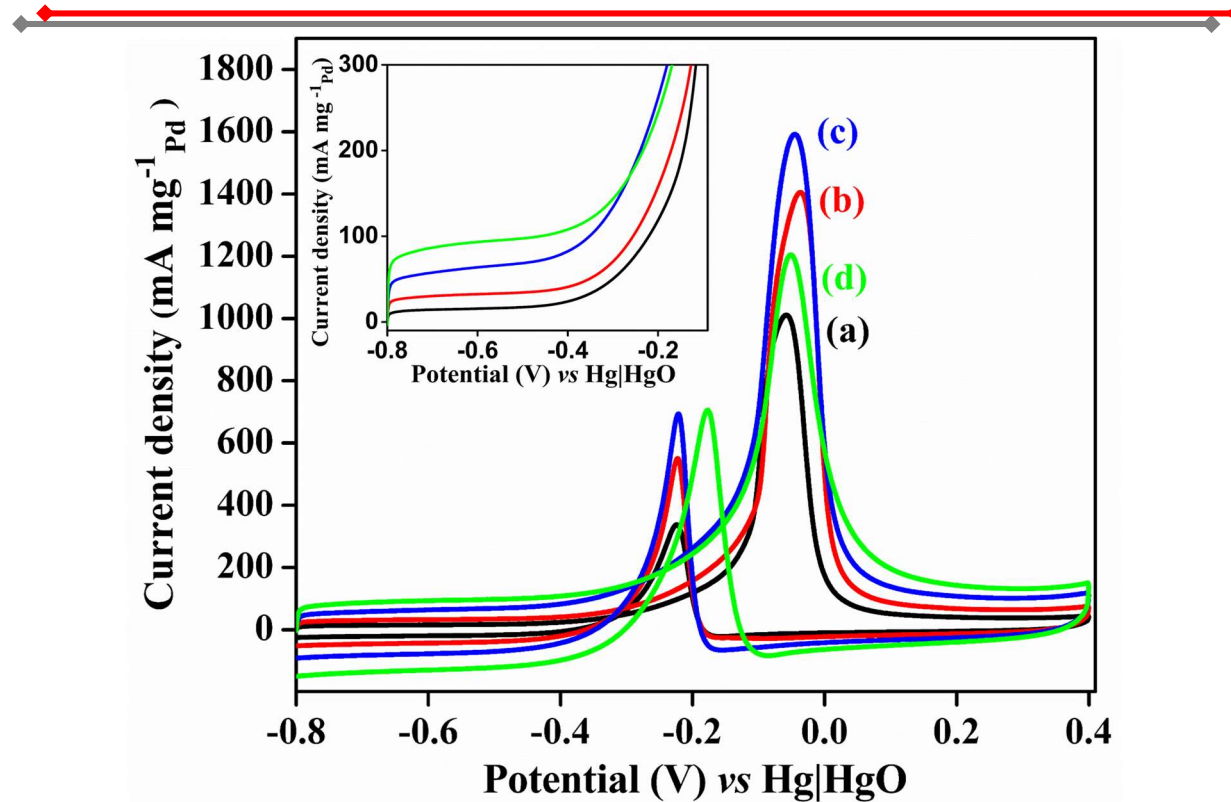
Fig. 4.8. CVs of (a) $Pd_{20}/NG180$, (b) $Pd_{15}Au_5/NG180$, (c) $Pd_{10}Au_{10}/NG180$ and (d) $Pd_5Au_{15}/NG180$ composite electrodes in 0.5 M NaOH + 1 M CH_3OH at a scan rate of 50 mV s^{-1}. Inset shows the expanded view of the forward scans to determine onset potentials.

The results clearly emphasized that the addition of Au had greatly influenced in enhancing the current densities and onset potentials of the electrocatalysts. E_{op} of $Pd_{10}Au_{10}/NG180$ and $Pd_5Au_{15}/NG180$ electrodes were observed at more negative potentials relative to the other $Pd_{20}/NG180$ and $Pd_{15}Au_5/NG180$ electrodes. The specific mass current density of $Pd_{10}Au_{10}/NG180$ is 1510 mA mg^{-1}_{Pd} and is the highest among all the composites. These results reveal that an improved electrocatalysis of MOR was achieved by introducing an optimal quantity of Au into $Pd_{20}/NG180$ nanocomposite. The optimum content of Au to replace Pd in $Pd_{20}/NG180$ composite in order to obtain an enhanced electrocatalytic activity toward MOR was observed to be 10%. The order of specific mass current densities of $Pd_{20-x}Au_x/NG180$ nanocomposites was found to be $Pd_{20}/NG180 < Pd_5Au_{15}/NG180 < Pd_{15}Au_5/NG180 < Pd_{10}Au_{10}/NG180$, which also agrees well with the EASA results obtained. The electrocatalytic activities of various Pd and bimetallic Pd-based catalysts anchored with various carbon supports are compared with the present catalyst in Table 4.2.

Table 4.2. Comparison of the specific mass current densities and onset potentials of various Pd based anode catalysts toward MOR in alkaline medium.

Catalysts	[Methanol]	Onset potential, E_{op}		Specific mass current density $(mA\ mg^{-1}_{Pd})$	Ref.
		(V vs. Hg|HgO)	(V vs. RHE)		
Pd/C	1.0 M	---	---	459	[262]
Pd/MnO$_2$/MWCNT	1.0 M	− 0.64	0.309	431	[272]
Pd$_{10}$Ag$_{10}$/CNT	0.5 M	− 0.62	0.329	731	[236]
Ni@Pd/MWCNT	1.0 M	− 0.64	0.309	771	[234]
Pd–SnO$_2$/rGO	1.0 M	− 0.41	0.539	1033	[92]
Pd-gC$_3$N$_4$-rGO	1.0 M	---	---	1550	[261]
Pd-gC$_3$N$_4$-CB-30[a]	1.0 M	− 0.46	0.489	1720	[262]
Hollow PdAu	1.0 M	---	---	405	[263]
Pd$_2$Au-180	1.0 M	− 0.53	0.419	492	[264]
Core-shell AuPd@Pd	1.0 M	---	---	650	[226]
Nanoporous –PdAu	1.0 M	− 0.65	0.299	867	[273]
Pd$_{30}$Au$_{70}$/C	1.0 M	− 0.54	0.409	951	[274]
Pd-Au-Ag/RGO	1.0 M	− 0.71	0.239	969	[275]
PdAu(Cu)(50%)/rGO -CNT	1.0 M	− 0.83	0.119	1047	[276]
PdCuCo/rGO	1.0 M	---	---	1063	[95]
Pd$_{10}$Au$_{10}$/NG180	1.0 M	− 0.72	0.229	1510	This work

[a] gC$_3$N$_4$-CB = gC$_3$N$_4$-carbon black

The specific mass current density obtained in the present study (1510 mA mg^{-1}$_{Pd}$; Pd$_{10}$Au$_{10}$/NG180) is more than three times higher compared to that (459 mA mg^{-1}$_{Pd}$) of conventional Pd/C catalyst of 20 wt.% Pd loading [262]. A Pd based trimetallic catalyst, Pd$_{72}$Cu$_{14}$Co$_{14}$, supported on rGO has exhibited a high mass current density of 1063 mA mg^{-1}$_{Pd}$ for MOR [95] . Recently, a trimetallic PdAuCu catalyst anchored onto rGO-CNT sandwich framework was synthesized and activated by electrochemical Cu depletion, and the resultant PdAu(Cu)50%/rGO-CNT catalyst comprising predominantly Pd and Au (together 97%) has exhibited a specific mass current density of 1047 mA mg^{-1}$_{Pd}$ [276]. The present Pd$_{10}$Au$_{10}$/NG180 catalyst resultant by a simple hydrothermal reduction method exploiting the combination of N-doped graphene was found to exhibit an excellent electrocatalytic performance with 1510 mA mg^{-1}$_{Pd}$ specific mass current density.

4.3.4. Chronoamperometry studies of methanol oxidation
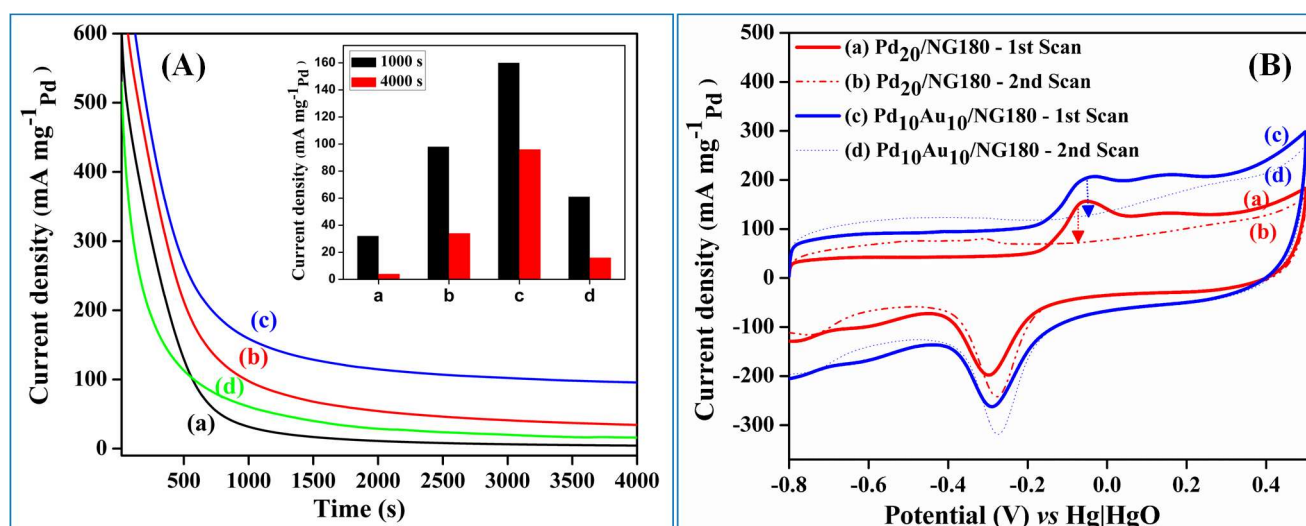
Fig. 4.9. (A) Chronoamperometry (CA) measurements of (a) Pd$_{20}$/NG180, (b) Pd$_{15}$Au$_5$/NG180, (c) Pd$_{10}$Au$_{10}$/NG180 and (d) Pd$_5$Au$_{15}$/NG180 in 0.5 M NaOH + 1 M CH$_3$OH at – 0.1 V (vs. Hg|HgO); Inset shows the bar diagram representation of the CA results at 1000 s and 4000s. (B) CO stripping measurements of (a, b) Pd$_{20}$/NG180 and (c, d) Pd$_{10}$Au$_{10}$/NG180 in 0.5 M NaOH at a scan rate of 50 mV s^{-1} (full lines: first scan; dotted lines: second scan).

Chronoamperometry (CA) measurements of Pd$_{20-x}$Au$_x$/NG180 composites have been carried out in 0.5 M NaOH + 1 M CH$_3$OH at a specified potential of - 0.1 V vs. Hg|HgO, and the results are shown in Fig. 4.9 (A). CA studies show an initial steep drop followed by a gradual drop in the mass activity with respect to the time. This drop could be attributed to the poisoning of

electrocatalysts by the adsorption of intermediates formed during methanol oxidation, particularly CO species on the surface of Pd catalysts. CA plots clearly revealed that there was a less decay tendency by replacing Pd with Au due to its synergistic interaction to promote MOR. As seen in Fig. 4.9 (A), the initial decay tendency of Pd_5Au_{15}/NG180 was high compared to that of Pd_{20}/NG180 up to ~500 s. However, after 500 s, the catalyst Pd_5Au_{15}/NG180 gets stabilized, and its current density surpassed that of Pd_{20}/NG180 by overcoming the CO poisoning due to the synergistic effect of Au in the composite. The steady-state current density of $Pd_{15}Au_5$/NG180 at the end of 1000 s (98 mA mg^{-1}_{Pd}) is ~3 times higher than that of the Pd alone catalyst (Fig. 4.9 (A) inset), Pd_{20}/NG180. $Pd_{10}Au_{10}$/NG180 exhibited the highest catalytic current compared to all the other catalyst compositions, and the steady state current density of $Pd_{10}Au_{10}$/NG180 at the end of 4000 s (98 mA mg^{-1}_{Pd}) is higher than those obtained for all the other catalysts at the end of mere 1000 s alone (97, 61 and 32 mA mg^{-1}_{Pd}). This observation establishes the long-time durability of $Pd_{10}Au_{10}$/NG180 catalyst. Contrary to the low specific mass current density of $Pd_{10}Au_{10}$/NG180 in CV experiments compared to Pd-gC_3N_4-rGO [261] and Pd-gC_3N_4-CB [262] (Table 4.2), $Pd_{10}Au_{10}$/NG180 composite outperformed in chronoamperometry MOR experiments compared to the both Pd alone catalysts. The steady state current density of $Pd_{10}Au_{10}$/NG180 at the end of 4000 s is as high as 98 mA mg^{-1}_{Pd}, which is far superior than that obtained, ~65 mA mg^{-1}_{Pd} at 3500 s and ~55 mA mg^{-1}_{Pd} at 2000 s, for Pd-gC_3N_4-rGO [261] and Pd- gC_3N_4-CB [262], respectively. When compared with Pd based bimetallic and trimetallic catalysts, the present $Pd_{10}Au_{10}$/NG180 catalyst was superior against PdCuCo/rGO (~20 mA mg^{-1}_{Pd} at 4000 s) [95] and Pd-Au-Ag/rGO (~100 mA mg^{-1}_{Pd} at 3000 s) [275] and was comparable with $Pd_{30}Au_{70}$/C (~190 mA mg^{-1}_{Pd} at 1000 s) [274]. These observations establish that Pd-based bimetallic or trimetallic catalysts could provide possibilities for the development of sustained long-time durable MOR catalysts. Long-time durability of $Pd_{10}Au_{10}$/NG180 catalyst examined from the ratio of the currents at 4000 s and 1000 s (i_{4000s}/i_{1000s}) further establishes that $Pd_{10}Au_{10}$/NG180 retained 61.3 % of the catalytic activity compared to 34.7 %, 26.3 % and 12.5 % by the other composites.

Table 4.3. Peak potentials, onset potentials and specific adsorption of CO stripping analysis.

Catalyst	E_p (V vs. RHE)	E_{op} (V vs. RHE)	Coulombic charge, (μC)	Mass adsorptivity (C g^{-1}$_{Pd}$)	EASA (m^2 g^{-1}$_{Pd}$)	Specific CO adsorption, Q_{co} (C m^{-2})
Pd$_{20}$/NG180	0.889	0.499	68.5	34.24	23	1.49
Pd$_{10}$Au$_{10}$/NG180	0.899	0.319	35.7	35.66	50	0.71

4.3.5. CO stripping analysis

In the methanol oxidation process, the by-product CO adsorbs onto the active sites of the catalyst and reduces the catalytic activity. CO stripping analysis has been formed in order to study the CO tolerance ability of the catalyst. In this experiment, with the modified electrode dipped in 0.5 M NaOH, N$_2$ gas was purged for 15 min for deaeration, and then purging with CO gas for 15 min was carried out to allow the adsorption of CO onto the electrocatalyst [190]. At last, N$_2$ gas was purged again to remove the dissolved CO from the electrolyte. For stripping studies, CVs were recorded from - 0.8 to 0.4 V at a scan rate of 50 mV s^{-1}, and two consecutive cycles have been recorded for CO stripping analysis (Fig. 4.9 (B)). The first cycle is represented with continuous line (−) which showed an anodic peak, representing the oxidation of CO adsorbed onto the electrocatalyst. The second cycle is represented with dotted line (-----), which did not show any anodic peak for CO oxidation revealing that the catalyst has fully regained its catalytic nature by the complete removal of chemisorbed CO intermediates. Results of the CO stripping experiments are given in Table 4.3. It was found that the onset potential for CO oxidation at Pd$_{10}$Au$_{10}$/NG180 (0.319 V vs. RHE) is more negative than that for Pd$_{20}$/NG180 (0.499 V vs. RHE), and it clearly infers that Pd$_{10}$Au$_{10}$/NG180 catalyst promotes CO oxidation at less over potentials and thus possess more CO tolerance ability. The specific adsorption of CO onto Pd$_{10}$Au$_{10}$/NG180 catalyst (0.71 C m^{-2}) is merely half to that onto Pd$_{20}$/NG180 (1.49 C m^{-2}). These results clearly suggested that the active surface of Pd$_{10}$Au$_{10}$/NG180 adsorbed less amounts of CO and is available more for electrocatalytic activity toward MOR with superior CO tolerance.

A plausible mechanism with the bimetallic or alloy system involving the formation of adsorbed hydroxyl groups on the secondary metal nanoparticles followed by the release of H_2O molecules electrochemically has been recommended for MOR [236]. The schematic illustration of the plausible mechanism toward methanol oxidation on the synthesized catalysts is shown in Fig. 4.10.

$$Au \; + \; H_2O \quad\quad \rightarrow \; Au\text{-}OH \; + \; H^+ + e^- \quad\quad\quad (1)$$

$$Pd \; + CH_3OH \quad\quad \rightarrow \; Pd\text{-}(CH_3OH)_{ads} \quad\quad\quad\quad (2)$$

$$Pd\text{-}(CH_3OH)_{ads} \quad \rightarrow \; Pd\text{-}(CO)_{ads} + 4\,H^+ + 4\,e^- \quad\quad (3)$$

$$Pd\text{-}(CO)_{ads} + Au\text{-}OH \; \rightarrow Pd + Au + CO_2 + H^+ + e^- \quad\quad (4)$$
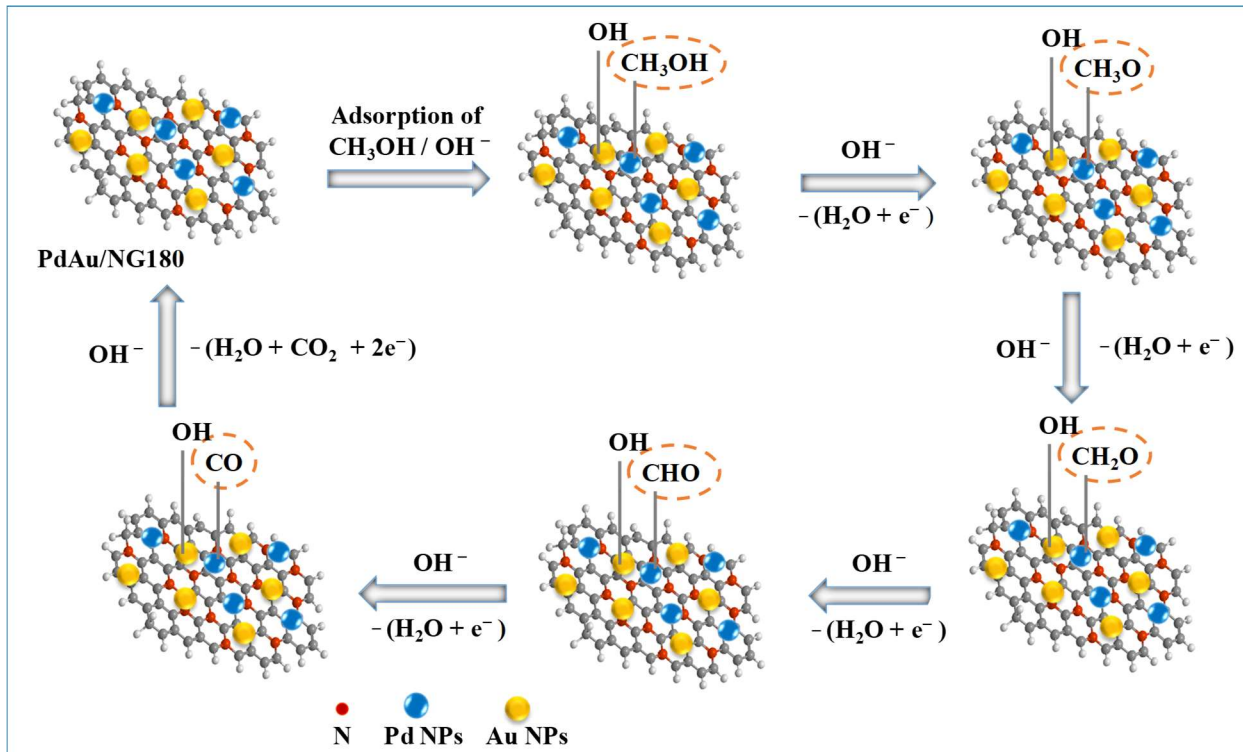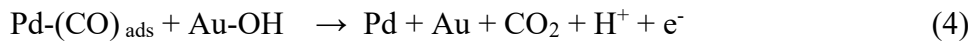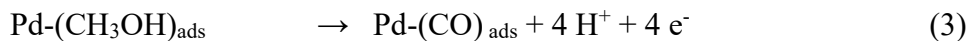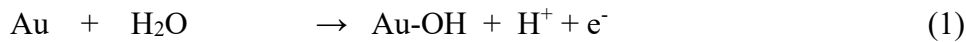
Fig. 4.10. Schematic illustration of plausible catalytic mechanism toward MOR in alkaline medium at PdAu/NG180 nanocomposites.

During the MOR electrochemically, CO species were generally produced on the surface of the catalyst due to the incomplete oxidation of CH_3OH molecules, as mentioned in Eq. 3. Thereafter, CO molecules or carbonaceous intermediates like CH_xO molecules resulted were

adsorbed by Pd nanoparticles could be oxidized by interacting with the generated M-OH species rendering to the bifunctional mechanism (Eq. 4). Therefore, with the synergistic effect of Au, the active sites of Pd would be retrieved efficiently, and eventually the E_{op} of the Au-containing composites becomes more negative than that of the catalyst without Au as shown in Table 4.1. By analyzing all the results, the enhanced electrocatalytic activity, long-time durability and high CO tolerance achieved for $Pd_{10}Au_{10}$/NG180 toward MOR could be ascribed to a combination of various salient features, such as high EASA, fine dispersion of nanoparticles in NG180 matrix, tiny crystallites of Pd of 6 nm, co-precipitation and co-existence of Pd and Au nanoparticles and synergistic effect of Au at optimum level for removal of CO species.

4.4. Conclusions

We opted a one-pot polyol method for the syntheses of $Pd_{20-x}Au_x$/NG180 (x wt % = 0, 5, 10, 15) composites, involving simultaneous reduction of both Pd and Au. N-doping has greatly influenced the electronic interaction with metal nanoparticles and helped in extended dispersion of the nanoparticles on the carbon support, and finite small crystallites of 6 nm Pd were obtained. Substitution of Pd by Au atoms necessarily increased the electrocatalytic activity of the composites at all the compositions, and $Pd_{10}Au_{10}$/NG180 exhibited the highest current density, long-time durability, high EASA, low onset potential and enhanced CO tolerance toward MOR. The steady state current-time analysis exhibited at least four times long-durable reactivity and stability by $Pd_{10}Au_{10}$/NG180 towards MOR compared to all the catalysts of other combinations, $Pd_{20-x}Au_x$/NG180 (x wt % = 0, 5, 15). The enhanced electrocatalytic performances of $Pd_{10}Au_{10}$/NG180 composite can be connected to the collective of the increase in EASA, the electronic interactions via N-doping and synergistic effect of Au in alleviating the CO poisoning. Such developments of cost-effective, high performance bimetallic $Pd_{10}Au_{10}$/NG180 catalyst by simple hydrothermal process could be explored to develop novel materials and pathways for promising high efficient anodic catalysts for MOR in DMFC applications.

Chapter 5

Design and synthesis of Pd decorated rGO-MoSe$_2$ 2D hybrid network as a high performance electrocatalyst for methanol oxidation

5. Design and synthesis of Pd decorated rGO-MoSe₂ 2D hybrid network as a high performance electrocatalyst for methanol oxidation

5.1. Introduction

Green energy production with the use of solar cells, fuel cells, etc. has been the utmost demand in order to protect the earth from environmental pollution and consequent global warming. These types of alternate energy resources would lead to revolutionary changes to meet the increasing energy demand whilst the depletion of fossil fuels and to reduce the pollution through green energy pathways. Among the various types of fuel cells, direct methanol fuel cells (DMFCs) have attracted keen interest because of its environmentally and eco-friendly power bases for transportation, portable devices and stationary devices because of its salient features like high safety and high energy densities [277]. From the past two decades, Pt based anode and cathode catalysts have been extensively in use. Nevertheless, the practical applications of these Pt based catalysts were hampered by its sluggish reaction kinetics, fuel crossover, their poisoning by the reaction intermediates. Another important factor is the high cost of the catalysts. Moreover, the inadequate Pt reserve cannot accomplish the practical and commercial applications. Alternatively, Pd based electrocatalysts have exhibited equivalent or even higher catalytic performances compared to Pt based electrocatalysts in fuel cell applications [278]. Later, improvement of the catalytic performances have been achieved by employing various carbon supports and alloy components [279]. Among the catalytic supports, 2D materials like graphene have attracted keen interest owing to their enormous electrical conductivity, high chemical stability and large surface area [280]. Moreover, some earlier studies have revealed that the catalytic performance of Pd and Pt based catalysts can be further enhanced by fabricating the nano composites by assemblage with different types of metal nanoparticles such as Ag [236], Au [281,282], Co [69], Ni [229], Cu [283], Ru [284], Sn [285], Mo[66] and also metal oxides which includes MnO_2 [286], CeO_2 [287], MoO_3 [288], V_2O_5 [289], Y_2O_3 [68], Sb_2O_3 [290] etc, with different carbon supports like carbon, carbon nanotubes (CNT) and graphene (rGO). On the other hand, transition metal chalcogenides (MoS_2, $MoSe_2$, WSe_2) have recently came in to existence as a capable alternative in the fields of fuel cells [28], supercapacitors [291], biosensors [292] and sensing applications, because of their exclusive catalytic ability in addition to its higher natural abundance. In particular, $MoSe_2$ nanosheets comprise a two-dimensional (2D) material and various attractive properties allied to energy conversion, sensing applications and energy storage systems, which have elicited a profound interest in designing and fabrication of

different kinds of electrocatalysts based on $MoSe_2$ [293]. However, the experimental and theoretical studies have revealed that the electrochemical activity and stability of $MoSe_2$ was directly interconnected with the electrical conductivity, while the intrinsic semiconducting property strictly bound to their catalytic activity. Therefore, there is a crucial requisite for optimizing the charge transfer in this type of $MoSe_2$ nanosheets, which is more advantageous in promoting the reaction kinetics. In view of the graphene-like 2D structural features, $MoSe_2$ nanosheets can syndicate with graphene and serve as co-building blocks for building a 3D hybrid framework, which facilitates effectively in lowering the charge-transfer resistances of the catalysts and thus consequently results in remarkable synergetic coupling effect. Since the catalytic productivities of the electrochemical processes like MOR were intensely depended on the nature of electrode materials, the investigation for significantly active electrocatalysts with prudently designed nano hybrid frameworks were vital for practical applications. This strategy facilitates a potential pathway for developing cost-effective and highly active catalysts for MOR in DMFCs.

In this chapter, we report a microwave assisted polyol method for the fabrication of ultrafine Pd nanoparticles embedded on 3D hybrid framework by utilizing rGO and $MoSe_2$ nano sheets [294,295]. The synthesized 3D Pd-$MoSe_2$-rGO framework possesses ultrathin hybrid walls, large surface area and also exhibits estimable electrical conductivity. These characteristic features can provide various strategies for quick diffusion of external reactants or species to the internal facades and help in electron transfer between the active sites and matrices. Consequently, the newly fabricated Pd-$MoSe_2$-rGO electrocatalyst demonstrated high catalytic activity for MOR accompanied by consistent long term stability and strong anti-poisoning capacity, enhanced electrocatalytic activity than Pd-rGO catalysts, with identical Pd loading. In this method, ethylene glycol (EG) which acts as both stabilizing as well as reducing agents with the aid of microwave irradiation in the syntheses, and eventually it could reduce the time and also production cost of the catalyst.

5.2. Experimental

5.2.1. Chemicals

Palladium (II) chloride ($PdCl_2$, Sigma Aldrich, 99.9 %), ethylene glycol ($C_2H_6O_2$, Finar, 99%), $KMnO_4$, H_2SO_4 (Finar, 99%), $NaNO_3$ (SDFL, 99.9%), H_2O_2 (RANKEM), molybdenum

(IV) selenide powder (MoSe$_2$, Alfa Aesar, 99.9%), graphite powder (Loba, 99%), NaOH (Finar), methanol (Merck, 99.7%). All aqueous solutions were prepared by using double-distilled deionized water of high resistance (18.2 Mohm), which was finally passed through 0.2 micron water filter cartridge.

5.2.2. Synthesis of GO and rGO

GO was prepared by the modified Hummer's method based on the report found in the literature [267]. In brief, 2 g of graphite powder and 1.5 g NaNO$_3$ were added to 70 mL of ice cooled conc. H$_2$SO$_4$, which was kept in 500 mL round-bottomed flask and stirred for uniform mixing for about 10 min. Then, 6 g KMnO$_4$ was added to the above mixture slowly and stirred for 2 h in ice bath. Then the reaction mixture was stirred for 4 h at 50 °C. After the stipulated time period, 90 mL warm water was added which leads to an increase in temperature to 90 °C and stirred for 15 min. Followed by the addition of 20 mL H$_2$O$_2$ (30 % w/w) with stirring for about 15 min, the final black suspension was collected by washing several times with aq. 5 % HCl and water and dried in an oven for 12 h at 80 °C. GO was further employed for the synthesis of rGO by using ascorbic acid (AA) reduction method [296]. In brief, 200 mg GO was dispersed in 200 mL water, and then required amount of ascorbic acid i.e 10 mM was added to the GO suspension. The solution pH was adjusted to 10 by adding aqueous NH$_3$ solution. Then this reaction mixture was refluxed at 90° C for 12 h. After cooling the reaction mixture to room temperature, the solid black product was washed several times with water and ethanol. It was collected and dried in an oven at 80° C for 12 h.

5.2.3. Synthesis of Pd-MoSe$_2$-rGO hybrid nanocomposite

The Pd-MoSe$_2$-rGO hybrid nanocomposite was prepared by microwave-assisted ethylene glycol (EG) reduction method. Briefly, 10 mg MoSe$_2$ and 40 mg rGO were mixed thoroughly in 50 mL (4:1 v/v) EG and isopropanol mixture via rigorous stirring and ultrasonic treatment. Then, H$_2$PdCl$_4$ solution was added drop-wise into the mixture under extreme stirring. The solution was placed in an ultrasonic bath for 4 h, and the pH value was adjusted to 10.0 using 1.0 M NaOH. Nitrogen gas was bubbled into the mixture for 30 min to remove the dissolved oxygen, and the mixture was then heated in a microwave oven (2450 MHz, 900 W) for 90 s with 30 s time intervals in order to reduce PdCl$_2$ into Pd nanoparticles as well as for intercalation of rGO sheets with MoSe$_2$

sheets. After cooling the composite solution down to room temperature, the pH value of the solution was adjusted to 4.0 by 0.1 M HNO_3 to assist the deposition of Pd nanoparticles onto the $MoSe_2$-rGO support. Finally, the Pd-$MoSe_2$-rGO hybrid nanocomposite was centrifuged and washed several times with water and ethanol. Then the catalyst was dried at 80 ℃ in a hot air oven for 10 h. Pd-rGO catalyst with 20 wt % Pd loading were also prepared through the same procedure.

5.2.4. Characterization

X-ray diffraction (XRD) measurements were performed using PAN Analytical Advance X-ray diffractometer using Ni-filtered Cu Kα (λ = 1.5406 Å) radiation in a 2θ scan range between 6° and 90°, with a step of 0.002° and scan speed of 0.5 s per step. Thermogravimetric analysis (TGA, Netzsch thermal analyser, STA 449 F1 Jupiter, Germany) was employed in order to verify the noble metal content in the catalyst. Raman spectra were recorded by micro-Raman spectrometer (HR800-UV Horiba Jobin Yvon, France) with the excitation source of 532 nm. Morphology of synthesized composites were analyzed using FESEM (FEI Apreo LoVac) equipped with an Aztec Standard energy dispersive X-ray spectroscopy (EDS) system. Surface morphology of the synthesized electrocatalysts was studied using transmission electron microscopy (TEM, Tecnai G2 20 S-TWIN microscope) at 200 kV. The surface elemental analysis was carried out by X-ray photoelectron spectroscopy (XPS) using Physical Electronics (PHI 5000 VersaProbe III) spectrometer with an Al Kα (1486.7 eV) radiation source at room temperature under ultrahigh vacuum (10^{-8} Pa).

5.2.5. Electrochemical analysis

Electrochemical measurements were performed by electrochemical workstation CHI (Model 619d, USA) in a three-electrode cell, employing 3 mm glassy carbon electrode (GCE) coated with the synthesized nanocomposites as working electrode, platinum wire as a counter electrode and Hg|HgO as a reference electrode. At first, GCE was polished with alumina slurries of 0.3 and 0.05 μm, rinsed with water, followed by successive sonication in ethanol and water, and allowed to dry. The catalytic ink was prepared by dispersing 2.5 mg catalyst in 450 μL 1:1 (v/v) IPA:H_2O mixture, and then 50 μL 5 wt% Nafion in ethanol was mixed to the above mixture. 2 μL catalytic ink was drop casted onto GCE and left to dry at room temperature. Electrocatalytic activities toward methanol oxidation were analyzed by using 0.5 M NaOH + 1 M CH_3OH test

solution after purging with high-purity nitrogen. All the electrode potentials presented in this manuscript were referred against Hg|HgO electrode.
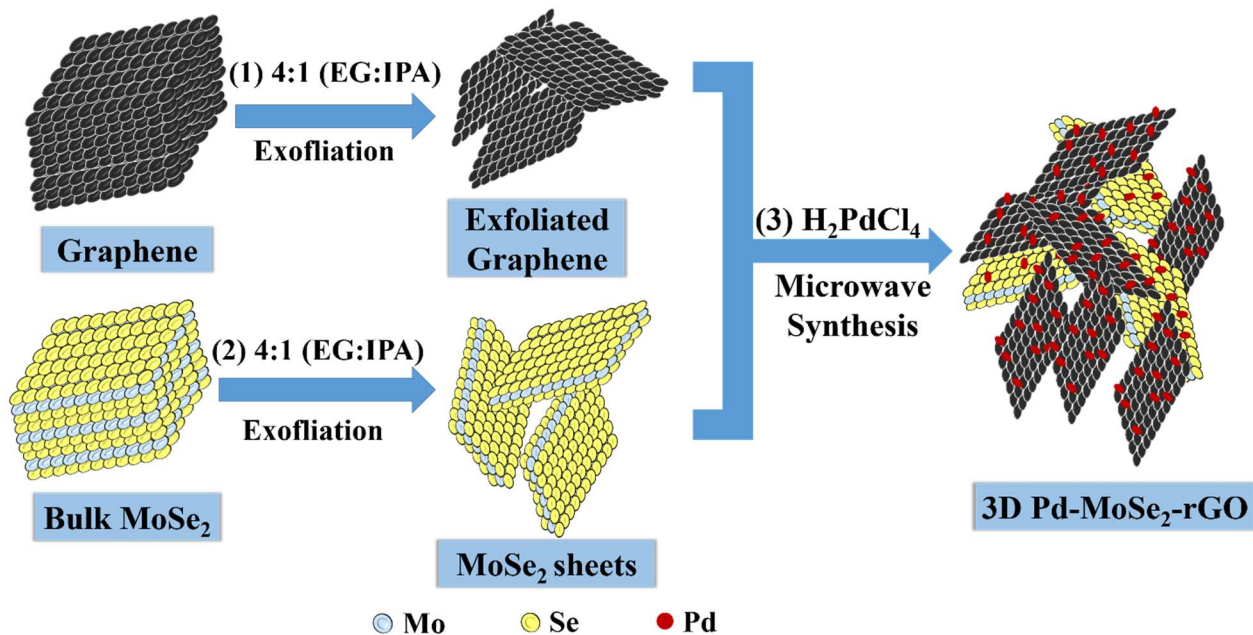
Fig. 5.1. Illustration of the synthesis of 3D hybrid Pd-MoSe$_2$-rGO catalyst: (1) Exfoliation of graphene (rGO); (2) Exfoliation of bulk MoSe$_2$ into few layer MoSe$_2$ nanosheets; (3) Fabrication of 3D MoSe$_2$ - graphene hybrid network via a microwave assisted synthesis and controlled deposition of Pd nanoparticles on to the MoSe$_2$-rGO matrix.

5.3. Results and discussion

5.3.1. Characterization of nanocomposites
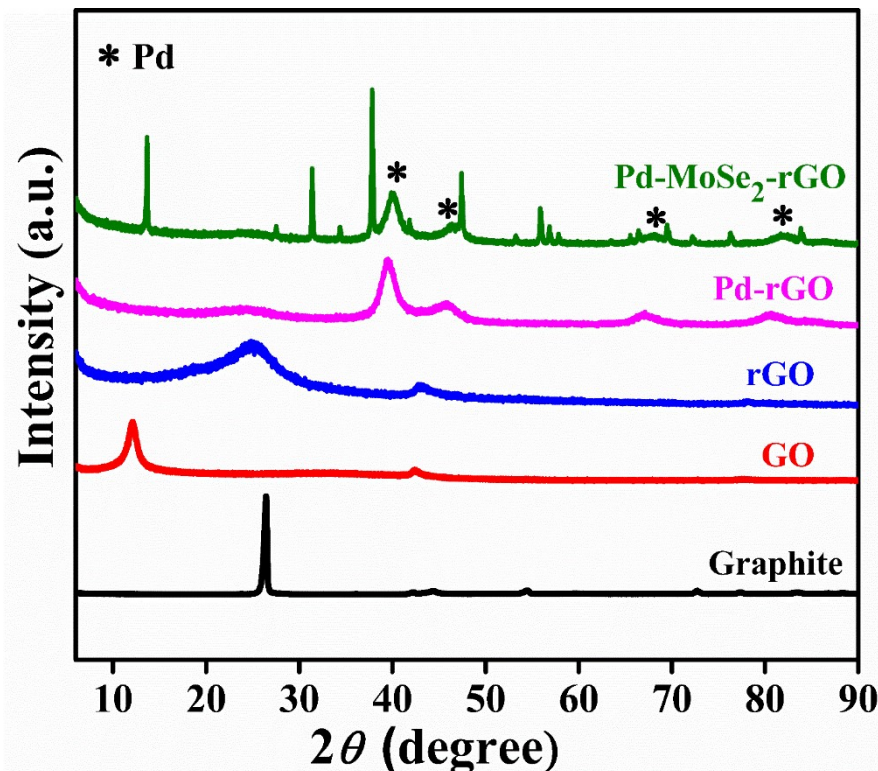
Fig. 5.2. XRD patterns of graphite, GO, rGO, Pd-rGO and Pd-MoSe$_2$-rGO nanocomposites.

XRD patterns of graphite, GO, rGO, Pd-rGO and Pd-MoSe$_2$-rGO nanocomposites are shown in Fig. 5.2. XRD patterns of graphite, GO and rGO have shown a prominent XRD peak corresponding to the carbon (002) plane. For graphite, the sharp peak observed at 26.45° corresponds to the graphitic nature of carbon (002) plane. In the case of GO, the peak was shifted to 12.13° with broadening, and it reveals that the inter-planar distance of (002) plane increased from 3.36 Å for graphite to 7.29 Å for GO. The synthesis of GO by modified Hummer's method introduces hydroxyl, carboxyl and epoxy functional groups, which all together increased the inter-planar distance in GO. In the case of reduced graphene oxide (rGO), the carbon (002) peak is shifted back and centered at ~ 25° with a broad nature from 19° to 30°, reflecting the regain of graphitic nature and the formation of a few graphene layer structure. XRD analysis confirmed both the formation of GO and the conversion of GO to rGO successfully. XRD patterns of Pd-rGO show the characteristic (111), (200), (220) and (311) diffractions of face centered cubic (fcc) Pd

(JCPDS No. 87-0638) [247,285]. XRD pattern of Pd-MoSe$_2$-rGO nanocomposites shows the characteristic diffractions of face centered cubic (fcc) Pd along with the diffraction peaks of crystalline MoSe$_2$ at 13.58º, 27.53º, 31.38º, 37.83º, 41.82º, 47.41º, 56.86º, 66.74º, 69.48º, 72.23º and 76.35º assigned to the crystal planes of (002), (004), (100), (103), (006), (105), (008), (108), (203), (116) and (205), respectively (JCPDS No. 29–0914) [35,297]. The broad peak in Pd-rGO and Pd-MoSe$_2$-rGO electrocatalysts at ca. 26° is due to the carbon (002) plane of rGO. In Pd-MoSe$_2$-rGO composites, diffraction peaks characteristic for both Pd metal and MoSe$_2$ were observed, illustrating the successful formation of the hybrid nanocomposite. The average crystallite sizes are estimated by using Scherrer method. It is observed to be 7.2 nm and 5.1 nm for Pd nanoparticles in Pd-rGO and Pd-MoSe$_2$-rGO nanocomposites, respectively.
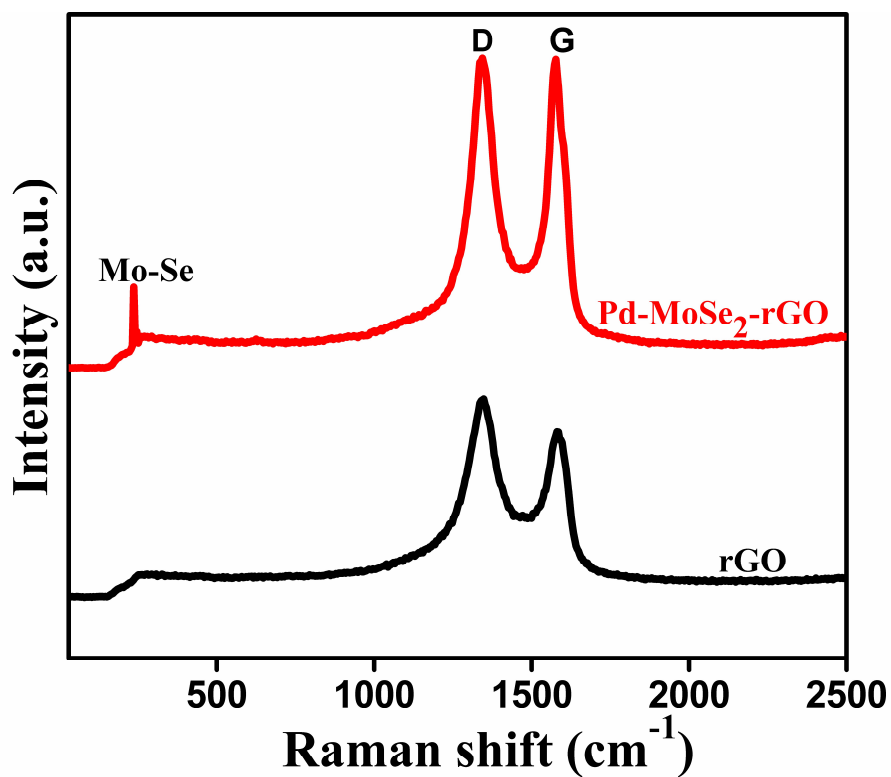
Fig. 5.3. Raman spectra of rGO and Pd-MoSe$_2$-rGO nanocomposites

In order to further identify the strong interaction between the components of the composite electrocatalyst, Raman spectroscopy analysis was employed. Figure 5.3 shows the Raman spectrum of pure rGO, which displays a broad peak at 1344 cm^{-1} for D band and a peak at 1587 cm^{-1} for G band [267]. Raman spectra of the synthesized nanocomposite additionally displays a

signal of Mo–Se band at ~ 240 cm^{-1} from Pd-rGO-MoSe$_2$[297]. These observations were conducive for the stability and strong interactions between the components of the composite electrocatalyst.
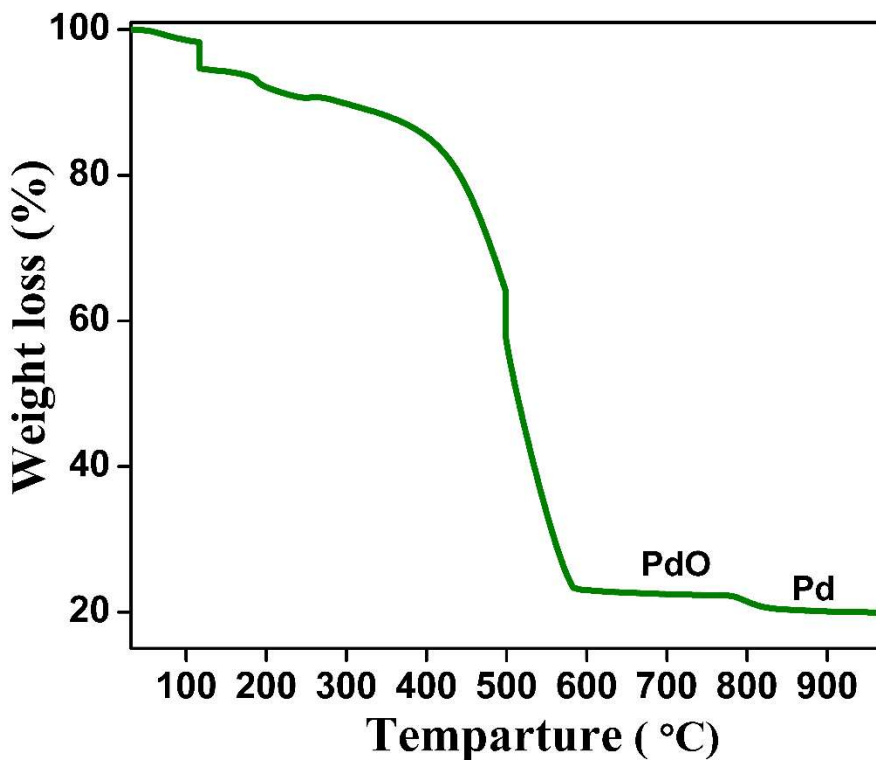
Fig. 5.4. Thermogravimetry (TGA) of the synthesized Pd-rGO catalyst.

Figure 5.4 shows the thermogram of the synthesized Pd-rGO electrocatalyst. In order to determine the Pd metal content of Pd-rGO catalyst, thermogravimetric analysis was employed. The temperature range was set up to 1000 ºC with a ramp of 10 ºC/min in air. From the resulting thermogram, a rapid weight loss has been identified at 340-400 ºC, which is ascribed to the degradation of the graphene (rGO) support, and it is extended up to ~580 ºC. A plateau observed in the range of ~ 585 - 780 ºC specifies that it was due to the generation of the residual palladium as Pd^{II}O. At further higher temperatures, a slight weight loss was identified at ~820 ºC, which could be attributed to the generation of metallic Pd [267]. The ultimate residual mass of Pd was observed to be approximately 19.83 %, which is very much equivalent to the Pd content used for the synthesis of the catalyst. From the TGA analysis, it can be emphasized that the prepared nanocomposite were loaded with the expected theoretical 20 wt % Pd loading without any loss in the Pd starting material.
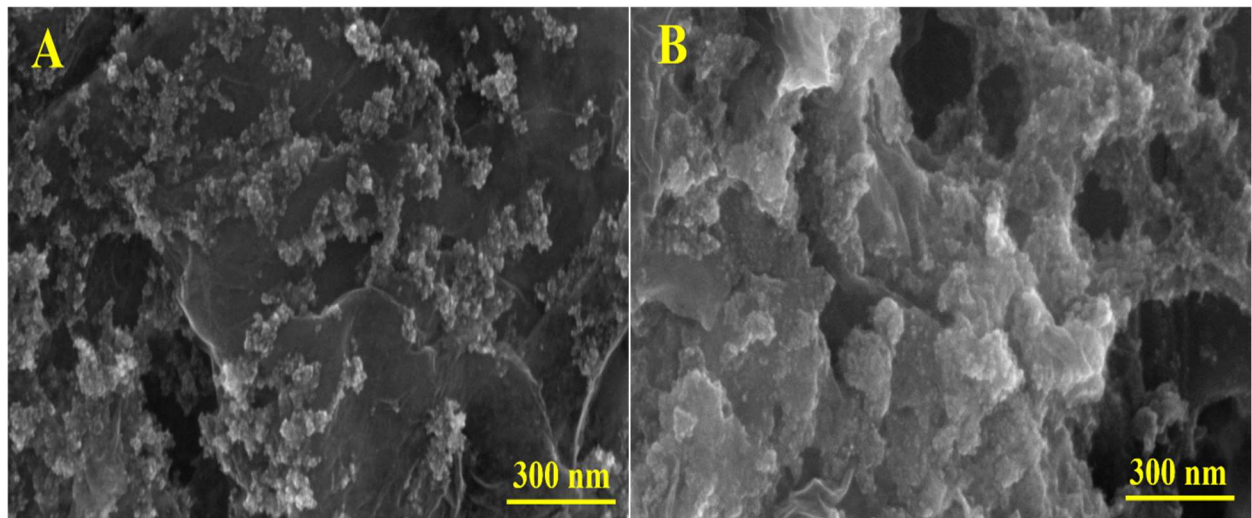
Fig. 5.5. FESEM images of (A) Pd-rGO and (B) Pd-MoSe$_2$-rGO nanocomposites.
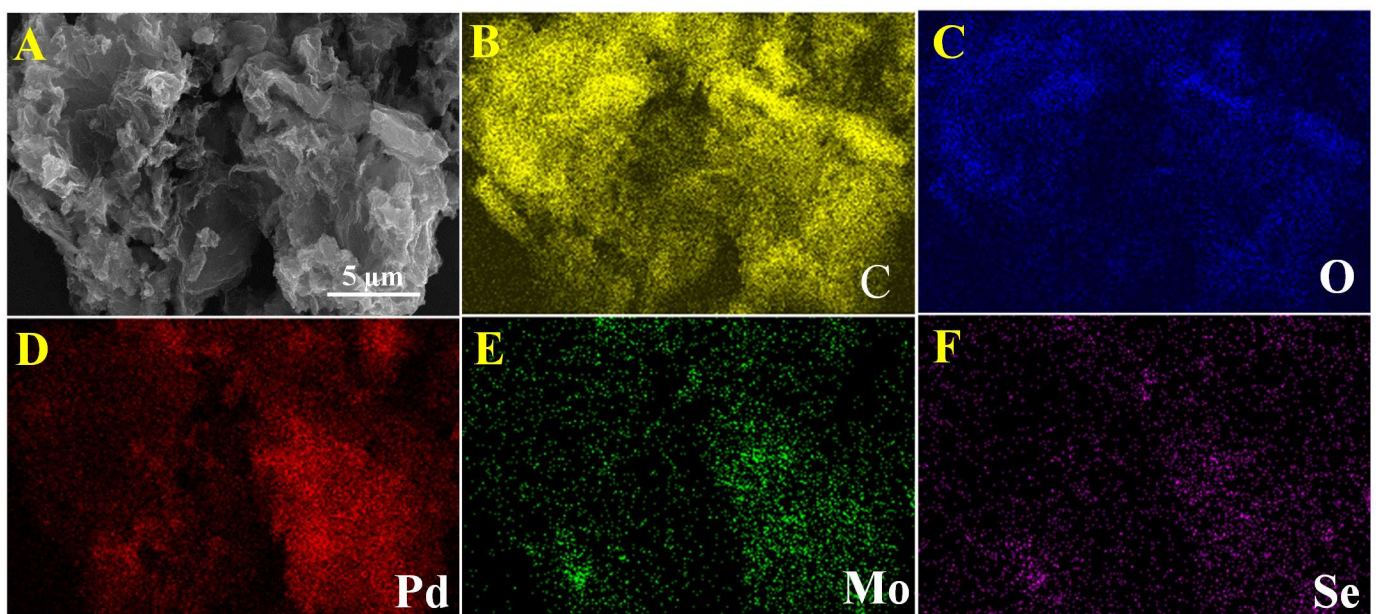
Fig. 5.6. (A) FESEM image of Pd-MoSe$_2$-rGO nanocomposite, and (B-F) its EDS mappings of the elements C, O, Pd, Mo and Se distribution.

FESEM analysis of the synthesized Pd-rGO and Pd-MoSe$_2$-rGO nanocomposites was carried out to know the distribution of the nanoparticles over the catalytic support, and the results are shown in Fig. 5.5. From these studies, it was identified that there is agglomeration of Pd nanoparticles over the graphene sheets in Pd-rGO. But, in the case of Pd-MoSe$_2$-rGO, the Pd

nanoparticles were dispersed on to the MoSe$_2$-rGO layers all throughout uniformly. These observations confirm that the Pd nanoparticles were evenly distributed onto the composite of Pd-MoSe$_2$-rGO and that the rGO and MoSe$_2$ layers had intercalated well to lead effective even distribution of Pd nanoparticles therein.

In order to further emphasize the distribution of the elements in Pd-MoSe$_2$-rGO composites, FESEM-EDS mapping was carried out and the results are shown in Fig. 5.6 (A-F). The distribution of Pd, Mo, Se, O and C has been visualized with different colours. The results depict that there is uniform distribution of graphene and MoSe$_2$ sheets along with the embedded Pd nanoparticles in to the hybrid nanocomposite.
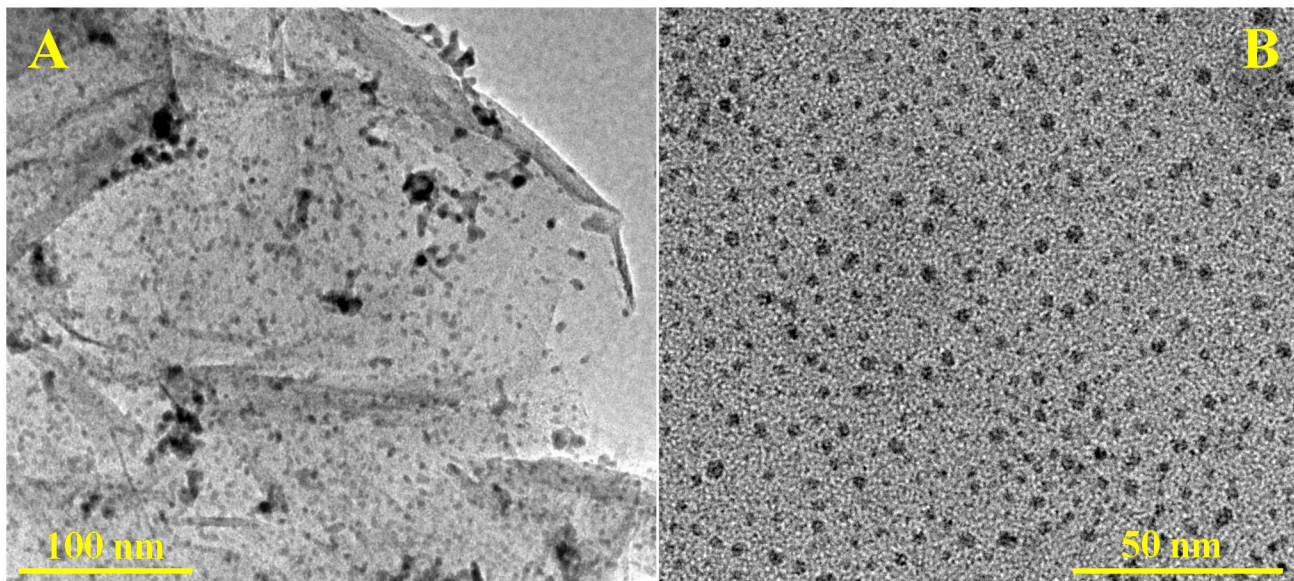
Fig. 5.7. TEM images of Pd-MoSe$_2$-rGO nanocomposite at different magnifications.

Figure 5.7 shows the TEM images of Pd-MoSe$_2$-rGO nanocomposite at different magnifications. From Fig. 5.7 (A), it is confirmed that Pd nanoparticles were uniformly distributed on the thin layers of MoSe$_2$-rGO. It is correlated with the FESEM-EDS analysis that MoSe$_2$ and rGO nanosheets were intercalated with each other, which facilitated the widespread uniform distribution of Pd nanoparticles in the composite. The average particles size was found to be in the range of 3-5 nm, as perceived from Fig. 5.7 (B). In overall, Pd nanoparticles of finite nano sizes in the range of 3-5 nm were embedded uniformly on to the MoSe$_2$-rGO hybrid nanocomposite without any agglomeration by employing the microwave assisted synthesis.
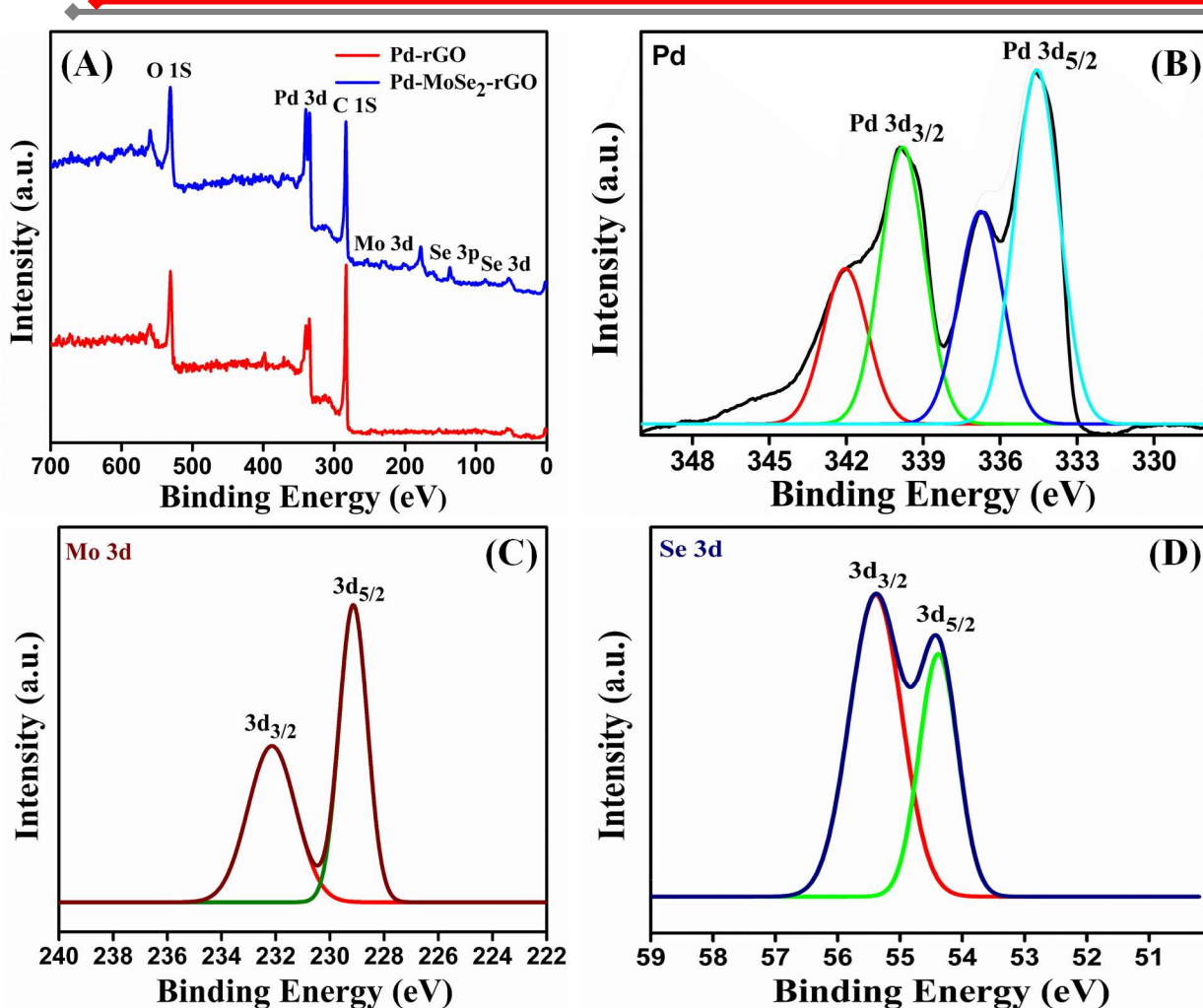
Fig. 5.8. (A) XPS survey spectrum of Pd-rGO and Pd-MoSe$_2$-rGO composites. High resolution spectrum of (B) Pd 3d, (C) Mo 3d and (D) Se 3d along with the deconvoluted peaks.

The surface elemental composition and binding energies (B.E) of the as-synthesized Pd-rGO and Pd-MoSe$_2$-rGO nanosheets were further examined by XPS analysis. Figure 5.8 (A) shows the survey spectrum of the catalysts. Distinct peaks corresponding to C 1S, O 1S, Pd 3d were observed in the case of Pd-rGO, and additional peaks corresponding to Mo 3d and Se 3d were also observed in the case of Pd-MoSe$_2$-rGO catalyst (Fig. 5.8(A)) [298]. High resolution spectra of Pd 3d, Mo 3d and Se 3d along with the deconvoluted peaks are shown in Fig. 5.8 (B-D). Pd 3d spectrum shows deconvoluted peaks at the binding energies (BEs) of 334.61 eV and 339.92 eV corresponding to Pd 3d$_{5/2}$ and Pd 3d$_{3/2}$, respectively, of metallic Pd [247,267,298]. The other two shoulder peaks observed at the BEs of 336.71 eV and 342.07 eV correspond to Pd 3d$_{5/2}$ and Pd 3d$_{3/2}$, respectively, of +2 oxidation state, inferring the existence of feeble Pd^{II}O in the

composite. In the high resolution spectrum of Mo, two characteristic peaks at the BEs of 232.25 and 229.10 eV attributed to Mo $3d_{3/2}$ and $3d_{5/2}$, respectively, were observed with the significance that Mo is present in the +4 oxidation state [298,299]. Additionally, the characteristic peaks arising from Se $3d_{5/2}$ and $3d_{3/2}$ orbitals are identified at the BEs of 55.33 and 54.58 eV, respectively, which could reveal the -2 oxidation state of Se in the $MoSe_2$ sheets [298,299].

5.3.2. Cyclic voltammetry studies
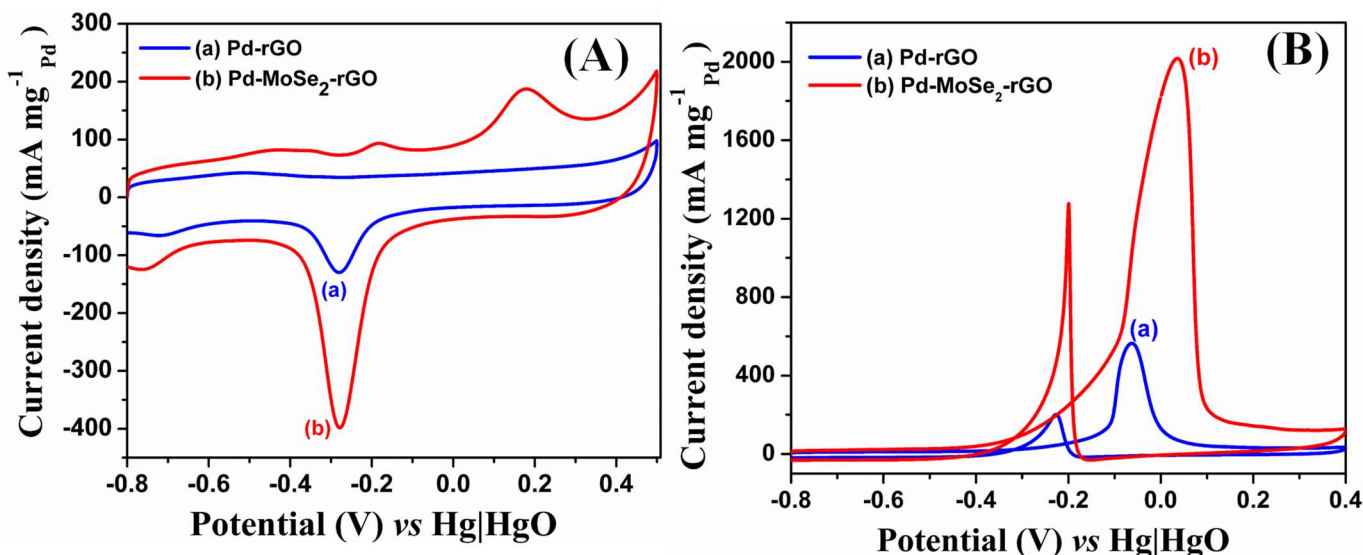
Fig. 5.9. (A) CV curves of Pd-rGO and Pd-MoSe₂-rGO catalysts in aq. 0.5 M NaOH. Scan rate is 50 mV s⁻¹. (B) CV curves of Pd-rGO and Pd-MoSe₂-rGO catalysts in aq. 0.5 M NaOH + 1 M CH₃OH. Scan rate is 50 mV s⁻¹.

Electrocatalytic performances of Pd-rGO and Pd-MoSe₂-rGO catalysts were evaluated by cyclic voltammetry (CV) studies. In order to determine the electrochemically active surface area (EASA), CV experiments have been carried out in 0.5 M NaOH with a scan rate of 50 mV s⁻¹, as shown in Fig. 5.9 (A). Electrocatalytic activity of the synthesized electrocatalysts was not only influenced by the catalytic properties but also the surface area. EASA of the fabricated electrodes has been measured by determining the coulombic charge of the PdO reduction peak [229] identified in the reverse scan, as shown in Fig. 5.9 (A). This oxide reduction peak appeared at E = -276 ± 32 mV in the CVs of the modified electrodes in 0.5 M NaOH. It is identified that the EASA of the Pd-MoSe₂-rGO electrode (51.81 m² g⁻¹$_{Pd}$) is nearly 3.5 times higher than that of Pd-rGO (15.30 m² g⁻¹$_{Pd}$). This result shows that the construction of the nanocomposite with a firm intercalation

between the two different 2D networks of MoSe$_2$ and rGO had prompted in the firm distribution of Pd nanoparticles on the composite surface and also the formation of much more finer nanoparticles of Pd with an enhanced surface area.

Table. 5.1. EASA and electrocatalytic activities of the synthesized electrocatalysts.

Catalyst	EASA (m^2 g^{-1}$_{Pd}$)	Onset potentials, E_{op} (V vs. Hg\|HgO)	Specific mass Current density (mA mg^{-1}$_{Pd}$)
Pd-rGO	15.30	-0.404	545
Pd-MoSe$_2$-rGO	51.81	-0.696	2000

Figure 5.9 (B) demonstrates the methanol oxidation reaction at the modified electrodes by CV investigation, and the CV profiles are well characterized by identifying two anodic current peaks, one in the forward scan (under anodic condition) and the other one in the backward scan (under cathodic condition). In the forward scan, the oxidation peak is produced due to the oxidation of both the molecules diffusing to the electrode and those freshly chemisorbed methanol molecules during the reaction process. The oxidation peak in the backward scan is principally allied with the elimination of carbonaceous species formed due to incomplete oxidation of the species, coming from CH$_3$OH adsorption rather than produced by freshly chemisorbed species [229,236]. The main carbonaceous species which is related to the MOR and the deactivation of catalyst is CO. Several research works have been carried out in order to improve the CO tolerance of Pt and Pd based catalysts by employing the noble and non-noble metals like Au, Ag, Ni, Co, Mo, Sn and also metal oxides. Several mechanisms have been proposed for the methanol oxidation reaction. The most widely accepted is an initial adsorption of methanol on the Pd or Pt surface, with subsequent dehydrogenation [236,300]. CO is an intermediate species generated during methanol oxidation reaction. In order to convert CO directly to CO$_2$, the catalyst surface should have adsorbed OH species. The net result of the oxidation of methanol at active Pd surfaces is the rapid surface coverage by the strongly adsorbing CO species, and as a result auto-inhibition of the catalytic process occurs. In the case of the Pd-MoSe$_2$-rGO electrodes, the density of –OH species would be

high leading to the possible conversion CO to CO_2. The actual mechanism feasible for the enhanced catalytic activity is illustrated.

The methanol dehydrogenation reaction mechanism on the Pd surface can be given as follows:

$$Pd\text{-}(CH_3OH)_{sol} \longleftrightarrow Pd\text{-}(CH_3OH)_{ads} \tag{1}$$

$$Pd\text{-}(CH_3OH)_{ads} + 4OH^- \longrightarrow Pd\text{-}(CO)_{ads} + 4\,H_2O + 4\,e^- \tag{2}$$
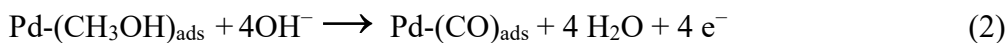
The oxygen-containing species formation and transfer process can be represented as follows:

$$MoSe_2 + H_2O \longrightarrow MoSe_2\text{-}OH_{ads} + H^+ + e^- \tag{3}$$

$$Pd\text{-}(CO)_{ads} + MoSe_2\text{-}OH_{ads} \longrightarrow Pd + MoSe_2 + CO_2 + H^+ + e^- \tag{4}$$
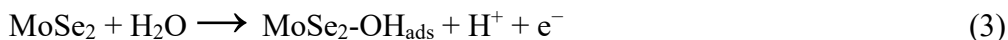
CV curves were analyzed with the help of peak current density (i_p) and onset potential (E_{op}) for the MOR, and their values are shown in Table 5.1. The current density (2000 mA mg^{-1}$_{Pd}$) obtained for the Pd-MoSe$_2$-rGO modified electrode was nearly four times high compared to that for Pd-rGO electrode (545 mA mg^{-1}$_{Pd}$) during methanol oxidation process. The Pd-MoSe$_2$-rGO catalyst shows more feasible lowest onset potential (-0.696 V), when compared with the Pd-rGO catalyst (-0.404 V). It implies that the CH_3OH molecules could be electrocatalytically oxidized at a more feasible negative onset potential at the hybrid Pd-MoSe$_2$-rGO nanocomposite with the aid of coordinated reactivities between MoSe$_2$ and rGO. All of the results suggest the remarkable MOR activity of the hybrid nanocomposite catalyst Pd-MoSe$_2$-rGO. The observed enormous catalytic performance of Pd-MoSe$_2$-rGO can conceivably explained by the more even dispersion and much more finer nanoparticles of Pd in the MoSe$_2$-rGO matrix. This excessive fine dispersion of Pd favors the optimal methanol adsorption necessary to start the oxidation. Furthermore, the methanol oxidation current at Pd-MoSe$_2$-rGO did not decay as quickly compared with the Pd-rGO electrode. In case of Pd-MoSe$_2$-rGO, a larger current persisted after the first oxidation peak, until the potential is reversed towards negative values. This indicates that it is not necessary to wait for hydroxide formation on the Pd surface to promote CO to CO_2. This promotion had occurred according to the mechanism illustrated. This is further evaluated by the long time reactivity studies and CO stripping studies. Comparison of the specific mass current densities and onset potentials of various Pd based anode electrocatalysts with different catalytic supports toward MOR in alkaline medium are shown in Table 5.2. Electrocatalytic performances of various Pd-based bimetallic and

trimetallic nanocomposites comprising other metals and metal oxides such as Au, Ag, Cu, Co, SnO_2, MnO_2, MoS_2, CeO_2, etc. and consisting of hollow and nanoporous structures with various backbone supports of rGO, CNT, graphitic carbon nitride, carbon black, etc. were compiled and compared in Table 5.2. Specific mass current density of Pd-MoSe$_2$-rGO composite electrode is very much superior than most of the composite materials discussed in Table 1, and additionally the onset potential of Pd-MoSe$_2$-rGO electrode is superior and more negative compared to almost all of the other composites discussed.

Table 5.2. Comparison of the specific mass current densities and onset potentials of various Pd based anode electrocatalysts toward MOR in alkaline medium.

S.No.	Catalysts	[Methanol]	Onset potentials, Eop (V vs. Hg|HgO)	Specific mass Current density (mA mg^{-1}$_{Pd}$)	Ref
1	Pd-MnO$_2$/MWCNT	1.0 M	− 0.64	431	[286]
2	Hollow PdAu	1.0 M	---	405	[263]
3	Pd$_{10}$Ag$_{10}$/CNT	0.5 M	− 0.62	731	[236]
4	Nanoporous -PdAu	1.0 M	− 0.65	867	[273]
5	Pd-Au-Ag/RGO	1.0 M	− 0.71	969	[275]
6	Pd-SnO$_2$/rGO	1.0 M	− 0.41	1033	[92]
7	PdAu(Cu)(50%)/rGO-CNT	1.0 M	− 0.83	1047	[301]
8	PdCuCo/rGO	1.0 M	---	1063	[95]
9	Pd-gC$_3$N$_4$-rGO	1.0 M	---	1550	[302]
10	Pd-gC$_3$N$_4$-CB-30^a	1.0 M	− 0.46	1720	[262]
11	Pd/Co-CeO$_2$	0.5 M	− 0.50	2418	[69]
12	Pd-MoS$_2$	1.0 M	---	433.5	[28]
13	Pd/SiO$_2$@RGO	1.0 M	-0.47	1533	[303]
14	Pd-MoSe$_2$-rGO	1.0 M	− 0.69	2000	This work

$_a$ gC$_3$N$_4$-CB = gC$_3$N$_4$-carbon black

5.3.3. Chronoamperometry and CO stripping studies
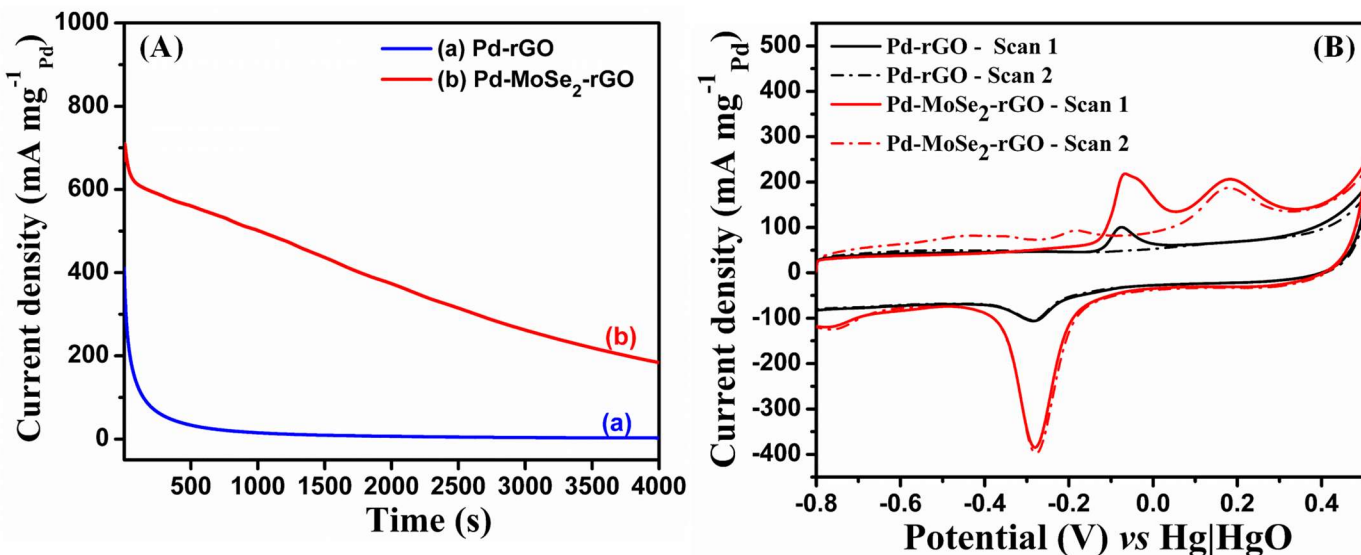
Fig. 5.10. (A) Chronoamperometry profiles of Pd-rGO and Pd-MoSe$_2$-rGO catalysts in 0.5 M NaOH + 1 M CH$_3$OH recorded at the applied potential of −0.1 V. (B) CV curves of Pd-rGO and Pd-MoSe$_2$-rGO catalysts for CO stripping analysis in 0.5 M NaOH at 50 mV s^{-1} scan rate (full lines: first scan; dotted lines: second scan).

In order to study the durability of the electrocatalyst for methanol oxidation, chronoamperometry experiments were performed at −0.1 V (Fig. 5.10 (A)) for 4000s. The specific mass activity of the electrocatalysts decayed quickly in the initial start of the experiment due to the absorbed CH$_3$OH molecules, which is rapidly undergoing oxidation on the surface of the catalysts and due to mass transport limiting layer formation by the methanol molecules. The CO like intermediate species along with the other carbonaceous species gradually occupy the active sites and thus deactivate the electrocatalysts during MOR. At the end of continuous 4000 s (> 1 h) testing, Pd-MoSe$_2$-rGO catalyst exhibited a sustained activity of 186.37 mA mg^{-1}$_{Pd}$, which was nearly 50 times higher than that of Pd-rGO (3.84 mA mg^{-1}$_{Pd}$) catalyst, specifying the excellent durability of Pd-MoSe$_2$-rGO because of the MoSe$_2$-rGO hybrid matrix, as explained in the mechanism of action.

CO stripping experiments have been carried out in order to study the CO tolerance ability of the synthesized Pd-rGO and Pd-MoSe$_2$-rGO catalysts. In this experiment, the modified electrode was dipped in 0.5 M NaOH and N$_2$ gas was purged for 15 min for deaeration; then

purging with CO gas for 15 min was carried out to allow the adsorption of CO onto the electrocatalyst [49]. At last, N_2 gas was purged again to remove the dissolved CO from the electrolyte. For stripping studies, CVs were recorded from - 0.8 to 0.4 V with a scan rate of 50 mV s^{-1}, and two consecutive cycles have been recorded for CO stripping analysis (Fig. 5.10 (B)). The first cycle is represented with continuous line (−) which showed an anodic peak, representing the oxidation of CO adsorbed onto the electrocatalyst. The second cycle is represented with dotted line (-----), which did not show any anodic peak for CO oxidation revealing that the catalyst has fully regained its catalytic nature by the complete removal of chemisorbed CO intermediates. From Fig. 5.9 (B), it is observed that Pd-MoSe$_2$-rGO catalyst had a more negative onset potential for CO electrooxidation (−0.621 V) when compared with Pd-rGO electrocatlyst (−0.545 V). This observation represents that the adsorbed CO molecules on the surface of Pd-MoSe$_2$-rGO would be oxidized more feasibly than that on Pd-rGO catalyst. It is therefore illustrated that the MoSe$_2$-rGO 3D matrix had promoted the oxidization of CO like poisoning molecules on the surface of Pd. It is noteworthy that the oxidation peak which corresponds to CO in the forward scan on Pd-MoSe$_2$-rGO is split into two peaks at −0.062 V and −0.037 V. It is most likely corresponding to the oxidation of CO$_{ads}$ on different active sites. This infers that some active surface sites on the Pd surface were promoted by MoSe$_2$-rGO 3D matrix and consequently the onset potential of CO oxidation shifted to a more negative feasible onset potential. The Pd-rGO catalyst displays an unaltered CO oxidation ability, which could be related to the conventional Pd based electrocatalyst.

5.4. Conclusions

In this chapter, the Pd nanoparticles with an average diameter around 3-5 nm were grown on the 3D hybrid matrix of MoSe$_2$ and graphene nanosheets. This was achieved by a simple co-assembly methodology with the help of microwave strategy. The fabricated Pd-MoSe$_2$-rGO hybrid matrix owns a set of noticeable structural features, comprising 3D interconnected framework, homogeneous distribution of Pd nanoparticles, good electron conductivity, thin walls and large specific surface area. All these features combined together makes a unique contribution for their enhanced electrocatalytic performance, which results in to more negative or feasible onset potentials, long lifespan and as well as high current densities and enhanced poison tolerance toward methanol oxidation in alkaline medium. It is expected that this bottom-up synthetic stratagem can be certainly employed in building various carbon based composites or electrocatlysts along with

transition metal chalcogenide, co-built 3D hybrid matrices with metal and metal oxide nanoparticles. ~~As a result, it makes a great potential for a wide range of applications such as sensors, photochemical catalysts, electrochemical capacitors and batteries.~~

Chapter 6

Summary and conclusions

6. Summary and Conclusions

The present thesis consists of six chapters. Chapter 1 provides the general introduction, need and objectives of the present work. Chapters 2 to 5 deal with the research and development of various Pd based electrocatalysts with different carbon supports along with other metal or metal chalcogenide nanoparticles in order to improve the electrocatalytic activity and durability of the catalysts toward methanol oxidation in DMFC applications. Finally, this chapter provides Summary and Conclusions arrived at in the present work.

In Chapter 2, Pd nanoparticles of finite and uniform size of 8-9 nm were embedded into the MWCNT matrix by sodium borohydride reduction method. TEM, XRD and XPS analyses revealed that the metallic state Pd nanoparticles were of finite FCC crystalline nature and contained both Pd^0 and Pd^{II} oxidation states. Among the dispersants, nanocomposite electrodes fabricated with chitosan dispersant exhibited high electroactive area and high current density for methanol oxidation. A dramatically very high steady-state catalytic current for methanol oxidation was observed at Pd-MWCNT-CS electrode (20.8 A g^{-1}_{pd}) compared to Pd-MWCNT-Nf electrode (4.1 A g^{-1}_{pd}). These observations emphasize the importance of a suitable dispersant for the fabrication of an efficient electrocatalyst. The CO stripping oxidation potentials were very much less positive compared to the methanol oxidation peak potentials. Electrocatalytic methanol oxidation and CO stripping measurements revealed that the application of chitosan as a dispersion medium for Pd-MWCNT catalysts significantly improved the electrocatalytic activity, stability and durability of the catalyst for methanol oxidation.

In Chapter 3, we have reported a method to prepare Pd nanoparticles with more uniform distribution on CNT supports. The synthesis process is simple and without the use of expensive chemicals. Cyclic voltammetry studies exhibited that Pd/NBCNT electrocatalysts had very high EASA. Analysis on the electrooxidation of CH_3OH using Pd/NBCNT electrocatalysts exhibited much higher specific activity than that of Pd nanoparticles supported on covalently functionalized CNT (Pd/CNT) and carbon (Pd/C). The electrochemical durability studies with steady-state current-time analysis also revealed that Pd/NBCNT exhibited high current density all throughout the investigation during extended long-time electrolysis of methanol. These results inferred that Pd nanoparticles supported on NBCNT were favourable for portable fields of applications in DMFCs.

In Chapter 4, we opted a one-pot polyol method for the syntheses of $Pd_{20-x}Au_x$/NG180 (x wt % = 0, 5, 10, 15) composites involving simultaneous reduction of both Pd and Au. N-doping has greatly influenced the electronic interaction with metal nanoparticles and also helped in extended dispersion of the nanoparticles on the carbon support, and eventually finite small crystallites of 6 nm Pd were resulted. Substitution of Pd by Au atoms inevitably increased the electrocatalytic activity of the composites at all the compositions, and $Pd_{10}Au_{10}$/NG180 exhibited the highest current density, long-time durability, high EASA, low onset potential and enhanced CO tolerance toward MOR. The steady state current-time analysis exhibited at least four times long-durable reactivity and stability by $Pd_{10}Au_{10}$/NG180 towards MOR compared to all the catalysts of other combinations, $Pd_{20-x}Au_x$/NG180 (x wt % = 0, 5, 15). The enhanced electrocatalytic performances of $Pd_{10}Au_{10}$/NG180 composite can be connected to the collective of the increase in EASA, the electronic interactions via N-doping and synergistic effect of Au in alleviating the CO poisoning. Such developments of cost-effective, high performance bimetallic $Pd_{10}Au_{10}$/NG180 catalyst by simple hydrothermal process would lead to novel materials and pathways for promising high efficient anodic catalysts for MOR in DMFC applications.

In Chapter 5, Pd nanoparticles with an average diameter around 3-4 nm were grown on the 3D hybrid matrix made from $MoSe_2$ and graphene nanosheets. This was achieved by a simple co-assembly methodology with the help of microwave strategy. The fabricated Pd-$MoSe_2$-rGO

Table 6.1. Collection of the electrocatalytic performances of various Pd-based hybrid nanocomposites toward MOR.

Nanocomposite	Method	Size of Pd nanoparticulate	Specific mass current density (mA mg$^{-1}_{Pd}$)	Steady-state mass current density at 2000 s (mA mg$^{-1}_{Pd}$)
Pd-MWCNT	Borohydride reduction	8-9 nm	2541	37
Pd/NBCNT	Non-covalent bonding	5.7 nm	1144	100
$Pd_{10}Au_{10}$/NG180	Hydrothermal	4-6 nm	1510	115
Pd-$MoSe_2$-rGO	Microwave	3-4 nm	2000	380

hybrid matrix owns a set of noticeable structural features, comprising 3D interconnected framework, homogeneous distribution of Pd nanoparticles, thin walls and large specific surface area. All these features combined together made a unique contribution for their combined electrocatalytic performance towards MOR, which thus was complimented with more negative onset potentials, long lifespan, and high current densities as well as an enhanced poison tolerance toward methanol oxidation in alkaline medium. It is thus concluded that this bottom-up synthetic stratagem could be certainly employed in building various carbon based composites or electrocatalysts along with transition metal chalcogenides, co-built 3D hybrid matrices with metal or metal oxide nanoparticles. Electrocatalytic performances of the various fabricated hybrid nanocomposite materials were compiled in Table 6.1.

- The present work provides new insights into the design and development of novel and advanced electrocatalytic materials for energy applications.

- Components, composite nature and synthetic methodology of the hybrid nanocomposites were strategically changed with the use of Pd along with other noble and non-noble metals or metal derivatives.

- The investigations categorically emphasized the importance of the use of other noble or non-noble metal or metal derivatives for the development of Pd-based nanocomposites in enhancing the electrocatalytic performances toward MOR.

- Electrocatalytic activity of the fabricated nanoPd materials toward MOR enhanced gradually with the decrease in the size of the nanoPd particles. Both the specific mass current density and the steady-state mass current density increased with the decrease in the size of the nanoPd particles.

- The average size of nanoPd particles decreased with the use of graphene or N-doped graphene matrices compared to the use of CNT matrices.

- Among the graphene-based electrocatalytic nanocomposite materials, Pd-MoSe$_2$-rGO possessed smaller nanoPd particles (3-4 nm) compared to Pd$_{10}$Au$_{10}$/NG180 (4-6 nm). Consequently, Pd-MoSe$_2$-rGO exhibited enhanced electrocatalytic acitivities, both the specific mass current density and the steady-state mass current density. While the specific mass current density of Pd-MoSe$_2$-rGO (2000 mA mg^{-1}$_{Pd}$) was moderately high compared to that of Pd$_{10}$Au$_{10}$/NG180 (1510 mA mg^{-1}$_{Pd}$), the steady-state mass current density of Pd-

MoSe$_2$-rGO (380 mA mg^{-1}$_{Pd}$) was exhorbitantly high compared to that of Pd$_{10}$Au$_{10}$/NG180 (115 mA mg^{-1}$_{Pd}$).

- Electrocatalytic performances of these hybrid nanocomposite Pd materials clearly reveal that the presense of reactive sites that promote the formation of oxygen-containing species like MoSe$_2$ are immensely helpful in enhancing the long-time reactivity and durability towards electrocatalytic MOR.

- Through these conscientious systematic investigations, the non-noble metal chalcogenide based Pd catalyst, Pd-MoSe$_2$-rGO, was observed to exhibit the most efficient electrocatalytic performances.

- Such developments of high performance and long-enduring bimetallic Pd catalysts comprising non-noble metal derivatives by simple hydrothermal process would lead to novel materials and pathways for promising high efficient, cost-effective anodic catalysts for MOR towards commercial DMFC applications.

- The strategies used in the present study for the development of the efficient anode catalysts for MOR can be effectively explored in the synthesis of many electrocatalysts, finding wide range of applications in sensors, photochemical catalysts, electrochemical capacitors and batteries.

References

[1]   B. Cook, *Eng. Sci. Educ. J.* **2002**, *11*, 205.

[2]   B. G. Pollet, I. Staffell, J. L. Shang, *Electrochim. Acta* **2012**, *84*, 235.

[3]   Y. Wang, K. S. Chen, J. Mishler, S. C. Cho, X. C. Adroher, *Appl. Energy* **2011**, *88*, 981.

[4]   F. Barbir, S. Yazici, *Int. J. Energy Res.* **2008**, *32*, 369.

[5]   S. J. Peighambardoust, S. Rowshanzamir, M. Amjadi, *Int. J. Hydrogen Energy* **2010**, *35*, 9349.

[6]   O. Z. Sharaf, M. F. Orhan, *Renew. Sustain. Energy Rev.* **2014**, *32*, 810.

[7]   B. C. Ong, S. K. Kamarudin, S. Basri, *Int. J. Hydrogen Energy* **2017**, *42*, 10142.

[8]   C. M. Miesse, W. S. Jung, K.-J. Jeong, J. K. Lee, J. Lee, J. Han, S. P. Yoon, S. W. Nam, T.-H. Lim, S.-A. Hong, *J. Power Sources* **2006**, *162*, 532.

[9]   H. G. Narayanan S, Surampudi S, Direct liquid-feed fuel cell with membrane electrolyte and manufacturing thereof. Google Patents; **1999**.

[10]   M. Nacef, A. M. Affoune, *Int. J. Hydrogen Energy* **2011**, *36*, 4208.

[11]   J.-H. Wee, *J. Power Sources* **2007**, *173*, 424.

[12]   G. L. Soloveichik, *Beilstein J. Nanotechnol.* **2014**, *5*, 1399.

[13]   U. B. Demirci, *Environ. Int.* **2009**, *35*, 626.

[14]   C. Lamy, A. Lima, V. LeRhun, F. Delime, C. Coutanceau, J.-M. Léger, *J. Power Sources* **2002**, *105*, 283.

[15]   A. M. Zainoodin, S. K. Kamarudin, M. S. Masdar, W. R. W. Daud, A. B. Mohamad, J. Sahari, *Appl. Energy* **2014**, *135*, 364.

[16]   S. K. N. Kumar, *Essentials in nanoscience and nanotechnology, book chapter, chapter 4-nanomaterials*; 2016.

[17]   A. Boudghene Stambouli, E. Traversa, *Renew. Sustain. Energy Rev.* **2002**, *6*, 295.

[18]   G. Sharma, A. Kumar, S. Sharma, M. Naushad, R. Prakash Dwivedi, Z. A. ALOthman, G. T. Mola, *J. King Saud Univ. - Sci.* **2019**, *31*, 257.

[19]   C. Ray, T. Pal, *J. Mater. Chem. A* **2017**, *5*, 9465.

[20]   Y. Liu, G. Zhao, D. Wang, Y. Li, *Natl. Sci. Rev.* **2015**, *2*, 150.

[21]   M. S. Saha, V. Neburchilov, D. Ghosh, J. Zhang, *Wiley Interdiscip. Rev. Energy Environ.* **2013**, *2*, 31.

[22]   C. M. Lieber, *MRS Bull.* **2003**, *28*, 486.

[23] M. Liu, R. Zhang, W. Chen, *Chem. Rev.* **2014**, *114*, 5117.

[24] V. Georgakilas, J. N. Tiwari, K. C. Kemp, J. A. Perman, A. B. Bourlinos, K. S. Kim, R. Zboril, *Chem. Rev.* **2016**, *116*, 5464.

[25] S. Sharma, B. G. Pollet, *J. Power Sources* **2012**, *208*, 96.

[26] K. Mohammad, A. Forouzan, Z. Hamid Reza Lotfi Zadeh, S. Omid, N. Ezzatollah, *J. Fuel Chem. Technol.* **2013**, *41*, 91.

[27] J. Ji, P. Dong, Y. Lin, X. Zeng, X. Li, X. Yang, Q. He, Y. Zhang, M. Xu, *J. Nanoparticle Res.* **2018**, *20*, 192.

[28] L. Yuwen, F. Xu, B. Xue, Z. Luo, Q. Zhang, B. Bao, S. Su, L. Weng, W. Huang, L. Wang, *Nanoscale* **2014**, *6*, 5762.

[29] K.-H. Ye, S.-A. Zhou, X.-C. Zhu, C.-W. Xu, P. K. Shen, *Electrochim. Acta* **2013**, *90*, 108.

[30] M. Wang, D. Guo, H. Li, *J. Solid State Chem.* **2005**, *178*, 1996.

[31] H. Huang, X. Wang, *Phys. Chem. Chem. Phys.* **2013**, *15*, 10367.

[32] S. Jana, G. Mondal, B. C. Mitra, P. Bera, A. Mondal, *Chem. Phys.* **2014**, *439*, 44.

[33] Y. Hao, X. Wang, Y. Zheng, J. Shen, J. Yuan, A. Wang, L. Niu, S. Huang, *Electrochim. Acta* **2016**, *198*, 127.

[34] T. MAIYALAGAN, F. KHAN, *Catal. Commun.* **2009**, *10*, 433.

[35] B. Kirubasankar, S. Vijayan, S. Angaiah, *Sustain. Energy Fuels* **2019**, *3*, 467.

[36] X. Wang, Q. Wu, K. Jiang, C. Wang, C. Zhang, *Sensors Actuators B Chem.* **2017**, *252*, 183.

[37] N. Toropov, T. Vartanyan, In *Comprehensive Nanoscience and Nanotechnology*; Elsevier, 2019; pp. 61–88.

[38] J. Zeng, *J. Mater. Chem.* **2012**, *22*, 3170.

[39] Y. Mu, H. Liang, J. Hu, L. Jiang, L. Wan, *J. Phys. Chem. B* **2005**, *109*, 22212.

[40] H. Huang, D. Sun, X. Wang, *J. Phys. Chem. C* **2011**, *115*, 19405.

[41] Y. Li, L. Tang, J. Li, *Electrochem. commun.* **2009**, *11*, 846.

[42] S. M. Choi, M. H. Seo, H. J. Kim, W. B. Kim, *Carbon N. Y.* **2011**, *49*, 904.

[43] Q.-L. Naidoo, S. Naidoo, L. Petrik, A. Nechaev, P. Ndungu, *Int. J. Hydrogen Energy* **2012**, *37*, 9459.

[44] H. Huang, Y. Fan, X. Wang, *Electrochim. Acta* **2012**, *80*, 118.

[45] S. Sun, G. Zhang, D. Geng, Y. Chen, M. N. Banis, R. Li, M. Cai, X. Sun, *Chem. - A Eur. J.* **2010**, *16*, 829.

[46]   R. Ahmadi, M. K. Amini, J. C. Bennett, *J. Catal.* **2012**, *292*, 81.

[47]   J. Yuan, B. He, L. Hong, J. Lu, J. Miao, L. Niu, *J. Mater. Chem.* **2012**, *22*, 19658.

[48]   J. Zhao, L. Zhang, H. Xue, Z. Wang, H. Hu, *RSC Adv.* **2012**, *2*, 9651.

[49]   Y. Lu, Y. Jiang, H. Wu, W. Chen, *J. Phys. Chem. C* **2013**, *117*, 2926.

[50]   Y. Hu, H. Zhang, P. Wu, H. Zhang, B. Zhou, C. Cai, *Phys. Chem. Chem. Phys.* **2011**, *13*, 4083.

[51]   H. Huang, D. Sun, X. Wang, *Chinese Sci. Bull.* **2012**, *57*, 3071.

[52]   G. Yang, Y. Li, R. K. Rana, J. Zhu, *J. Mater. Chem. A* **2013**, *1*, 1754.

[53]   S. Yu, Q. Liu, W. Yang, K. Han, Z. Wang, H. Zhu, *Electrochim. Acta* **2013**, *94*, 245.

[54]   H. Huang, Q. Chen, M. He, X. Sun, X. Wang, *J. Power Sources* **2013**, *239*, 189.

[55]   Y. Ito, T. Takeuchi, T. Tsujiguchi, M. A. Abdelkareem, N. Nakagawa, *J. Power Sources* **2013**, *242*, 280.

[56]   X. Yang, X. Wang, G. Zhang, J. Zheng, T. Wang, X. Liu, C. Shu, L. Jiang, C. Wang, *Int. J. Hydrogen Energy* **2012**, *37*, 11167.

[57]   Q. Jiang, L. Jiang, H. Hou, J. Qi, S. Wang, G. Sun, *J. Phys. Chem. C* **2010**, *114*, 19714.

[58]   F.-B. Zhang, H.-L. Li, *Carbon N. Y.* **2006**, *44*, 3195.

[59]   C. Hu, X. Wang, *Int. J. Hydrogen Energy* **2015**, *40*, 12382.

[60]   Z. Liu, X. Zhang, L. Hong, *Electrochem. commun.* **2009**, *11*, 925.

[61]   Y. Wang, X. Wang, C. M. Li, *Appl. Catal. B Environ.* **2010**, *99*, 229.

[62]   Z. Yin, Y. Zhang, K. Chen, J. Li, W. Li, P. Tang, H. Zhao, Q. Zhu, X. Bao, D. Ma, *Sci. Rep.* **2015**, *4*, 4288.

[63]   K. Mandal, D. Bhattacharjee, P. S. Roy, S. K. Bhattacharya, S. Dasgupta, *Appl. Catal. A Gen.* **2015**, *492*, 100.

[64]   T. Jurzinsky, R. Bär, C. Cremers, J. Tübke, P. Elsner, *Electrochim. Acta* **2015**, *176*, 1191.

[65]   Z. Yin, M. Chi, Q. Zhu, D. Ma, J. Sun, X. Bao, *J. Mater. Chem. A* **2013**, *1*, 9157.

[66]   F. Fathirad, A. Mostafavi, D. Afzali, *Int. J. Hydrogen Energy* **2017**, *42*, 3215.

[67]   J. E. Solis-Tobías, J. A. Díaz-Guillén, R. Pérez-Hernández, J. C. Carrillo-Rodríguez, I. L. Alonso-Lemus, F. J. Rodríguez-Varela, *Int. J. Hydrogen Energy* **2019**, *44*, 12415.

[68]   J. Li, S. Wang, B. Zhang, W. Wang, L. Feng, *Int. J. Hydrogen Energy* **2017**, *42*, 12236.

[69]   Q. Tan, H. Zhu, S. Guo, Y. Chen, T. Jiang, C. Shu, S. Chong, B. Hultman, Y. Liu, G. Wu,

Nanoscale **2017**, *9*, 12565.

[70]   Z.-P. Sun, X.-G. Zhang, R.-L. Liu, Y.-Y. Liang, H.-L. Li, *J. Power Sources* **2008**, *185*, 801.

[71]   Y. Zhao, X. Yang, J. Tian, F. Wang, L. Zhan, *Mater. Sci. Eng. B* **2010**, *171*, 109.

[72]   L. Abolghasemi Fard, R. Ojani, J. B. Raoof, *Int. J. Hydrogen Energy* **2016**, *41*, 17987.

[73]   Y. Zhao, X. Yang, J. Tian, F. Wang, L. Zhan, *Int. J. Hydrogen Energy* **2010**, *35*, 3249.

[74]   N. Kakati, J. Maiti, S. H. Lee, Y. S. Yoon, *Int. J. Hydrogen Energy* **2012**, *37*, 19055.

[75]   M. Satyanarayana, G. Rajeshkhanna, M. K. Sahoo, G. R. Rao, *ACS Appl. Energy Mater.* **2018**, *1*, 3763.

[76]   Y. Zhao, L. Zhan, J. Tian, S. Nie, Z. Ning, *Int. J. Hydrogen Energy* **2010**, *35*, 10522.

[77]   Y. Ren, S. Zhang, H. Li, *Int. J. Hydrogen Energy* **2014**, *39*, 288.

[78]   Y. Xie, W. Yu, J. Wang, Y. Wu, S. Niu, W. Guo, T. Lin, L. Shao, *Phys. Chem. Chem. Phys.* **2017**, *19*, 25214.

[79]   F. Zhu, G. Ma, Z. Bai, R. Hang, B. Tang, Z. Zhang, X. Wang, *J. Power Sources* **2013**, *242*, 610.

[80]   Y. Zhao, L. Zhan, J. Tian, S. Nie, Z. Ning, *Electrochim. Acta* **2011**, *56*, 1967.

[81]   H. Huang, X. Wang, *J. Mater. Chem.* **2012**, *22*, 22533.

[82]   J. C. Ng, C. Y. Tan, B. H. Ong, A. Matsuda, W. J. Basirun, W. K. Tan, R. Singh, B. K. Yap, *Mater. Res. Bull.* **2019**, *112*, 213.

[83]   L. Li, M. Chen, G. Huang, N. Yang, L. Zhang, H. Wang, Y. Liu, W. Wang, J. Gao, *J. Power Sources* **2014**, *263*, 13.

[84]   J.-N. Zheng, S.-S. Li, X. Ma, F.-Y. Chen, A.-J. Wang, J.-R. Chen, J.-J. Feng, *J. Power Sources* **2014**, *262*, 270.

[85]   R. Awasthi, R. N. Singh, *Carbon N. Y.* **2013**, *51*, 282.

[86]   Y. Wang, Y. Zhao, J. Yin, M. Liu, Q. Dong, Y. Su, *Int. J. Hydrogen Energy* **2014**, *39*, 1325.

[87]   H. Na, L. Zhang, H. Qiu, T. Wu, M. Chen, N. Yang, L. Li, F. Xing, J. Gao, *J. Power Sources* **2015**, *288*, 160.

[88]   M. Zhang, Z. Yan, Q. Sun, J. Xie, J. Jing, *New J. Chem.* **2012**, *36*, 2533.

[89]   C.-T. Hsieh, P.-Y. Yu, D.-Y. Tzou, J.-P. Hsu, Y.-R. Chiu, *J. Electroanal. Chem.* **2016**, *761*, 28.

[90]   X. Cui, X. Wang, X. Xu, S. Yang, Y. Wang, *Electrochim. Acta* **2018**, *260*, 47.

[91]   J. Ji, P. Dong, Y. Lin, X. Zeng, X. Li, X. Yang, Q. He, Y. Zhang, M. Xu, *J. Nanoparticle*

Res. **2018**, *20*, 192.

[92]   Y. Hu, T. Mei, J. Li, J. Wang, X. Wang, *RSC Adv.* **2017**, *7*, 29909.

[93]   A. Kumar, N. Kumari, V. K. V. P. Srirapu, R. N. Singh, *Int. J. Hydrogen Energy* **2018**, *43*, 9677.

[94]   F. Yang, B. Zhang, S. Dong, Y. Tang, L. Hou, Z. Chen, Z. Li, W. Yang, C. Xu, M. Wang, Y. Li, Y. Li, *Appl. Surf. Sci.* **2018**, *452*, 11.

[95]   F. Yang, B. Zhang, S. Dong, C. Wang, A. Feng, X. Fan, Y. Li, *J. Energy Chem.* **2019**, *29*, 72.

[96]   M. Singh, S. Manikandan, A. K. Kumaraguru, *Res. J. Nanosci. Nanotechnol.* **2011**, *1*, 1.

[97]   S. J. C. Daraio, **2011**, 27.

[98]   V. M. Arole, S. V Munde, *JAASTMaterial Sci. (Special Issue* **2014**, *1*, 2.

[99]   Y. Wang, Y. Xia, *Nano Lett.* **2004**, *4*, 2047.

[100] P. Garrigue, M.-H. Delville, C. Labrugère, E. Cloutet, P. J. Kulesza, J. P. Morand, A. Kuhn, *Chem. Mater.* **2004**, *16*, 2984.

[101] L. Rafael, V. R. S, R. S. Varma, C. J. H, G. a. Kraus, *Sustainable Preparation of Metal Nanoparticles: Methods and Applications*; 2012.

[102] J. M. Campelo, D. Luna, R. Luque, J. M. Marinas, A. A. Romero, *ChemSusChem* **2009**, *2*, 18.

[103] S. Horikoshi, N. Serpone, In *Microwaves in Nanoparticle Synthesis*; Wiley-VCH Verlag GmbH & Co. KGaA: Weinheim, Germany, 2013; pp. 1–24.

[104] X. Liu, D. Wang, Y. Li, *Nano Today* **2012**, *7*, 448.

[105] A. Dehghan Banadaki, A. Kajbafvala, *J. Nanomater.* **2014**, *2014*, 1.

[106] K. An, G. A. Somorjai, *Catal. Letters* **2015**, *145*, 233.

[107] M. Blosi, S. Ortelli, A. Costa, M. Dondi, A. Lolli, S. Andreoli, P. Benito, S. Albonetti, *Materials (Basel).* **2016**, *9*, 550.

[108] A. Gentile, F. Ruffino, M. Grimaldi, *Nanomaterials* **2016**, *6*, 110.

[109] D. Wang, P. Zhao, Y. Li, *Sci. Rep.* **2011**, *1*, 37.

[110] Y.-W. Lee, S. Cha, K.-W. Park, J. I. Sohn, J. M. Kim, *J. Nanomater.* **2015**, *2015*, 1.

[111] R. Wang, H. Wang, F. Luo, S. Liao, *Electrochem. Energy Rev.* **2018**, *1*, 324.

[112] Y.-J. Wang, N. Zhao, B. Fang, H. Li, X. T. Bi, H. Wang, *Chem. Rev.* **2015**, *115*, 3433.

[113] A. Chen, P. Holt-Hindle, *Chem. Rev.* **2010**, *110*, 3767.

[114] J. Wang, B. Li, T. Yersak, D. Yang, Q. Xiao, J. Zhang, C. Zhang, *J. Mater. Chem. A* **2016**, *4*, 11559.

[115] E. Antolini, J. R. C. Salgado, E. R. Gonzalez, *J. Power Sources* **2006**, *160*, 957.

[116] T. Walbert, M. Antoni, F. Muench, T. Späth, W. Ensinger, *ChemElectroChem* **2018**, *5*, 1087.

[117] P. K. Chu, G. S. Wu, In *Surface Modification of Magnesium and its Alloys for Biomedical Applications*; Elsevier, 2015; Vol. 1, pp. 89–119.

[118] Y. Holade, N. Sahin, K. Servat, T. Napporn, K. Kokoh, *Catalysts* **2015**, *5*, 310.

[119] J. Zhang, X. Wang, C. Wu, H. Wang, B. Yi, H. Zhang, *React. Kinet. Catal. Lett.* **2004**, *83*, 229.

[120] C. Dhand, N. Dwivedi, X. J. Loh, A. N. Jie Ying, N. K. Verma, R. W. Beuerman, R. Lakshminarayanan, S. Ramakrishna, *RSC Adv.* **2015**, *5*, 105003.

[121] S. Ahmed, M. Ahmad, B. L. Swami, S. Ikram, *J. Adv. Res.* **2016**, *7*, 17.

[122] J. Y. Kim, Z. G. Yang, C.-C. Chang, T. I. Valdez, S. R. Narayanan, P. N. Kumta, *J. Electrochem. Soc.* **2003**, *150*, A1421.

[123] A. Ali, H. Zafar, M. Zia, I. ul Haq, A. R. Phull, J. S. Ali, A. Hussain, *Nanotechnol. Sci. Appl.* **2016**, *Volume 9*, 49.

[124] E. Lebègue, S. Baranton, C. Coutanceau, *J. Power Sources* **2011**, *196*, 920.

[125] C. Grolleau, C. Coutanceau, F. Pierre, J.-M. Leger, *J. Power Sources* **2010**, *195*, 1569.

[126] W.-D. Lee, D.-H. Lim, H.-J. Chun, H.-I. Lee, *Int. J. Hydrogen Energy* **2012**, *37*, 12629.

[127] C. Venkateswara Rao, B. Viswanathan, *J. Phys. Chem. C* **2009**, *113*, 18907.

[128] M. A. Malik, M. Y. Wani, M. A. Hashim, *Arab. J. Chem.* **2012**, *5*, 397.

[129] R. A. Martínez-Rodríguez, F. J. Vidal-Iglesias, J. Solla-Gullón, C. R. Cabrera, J. M. Feliu, *J. Am. Chem. Soc.* **2014**, *136*, 1280.

[130] A. Pal, S. Shah, S. Belochapkine, D. Tanner, E. Magner, S. Devi, *Colloids Surfaces A Physicochem. Eng. Asp.* **2009**, *337*, 205.

[131] J. W. Jianlin Li, Qingliu Wu, *Handbook of Nanoparticles*; Aliofkhazraei, M., Ed.; Springer International Publishing: Cham, 2016.

[132] C. Gumeci, A. Marathe, R. L. Behrens, J. Chaudhuri, C. Korzeniewski, *J. Phys. Chem. C* **2014**, *118*, 14433.

[133] W. Ji, W. Qi, S. Tang, H. Peng, S. Li, *Nanomaterials* **2015**, *5*, 2203.

[134] H. Kim, N. J. Jeong, S. J. Lee, K. S. Song, *Korean J. Chem. Eng.* **2008**, *25*, 443.

[135] S.-I. Pyun, H.-C. Shin, J.-W. Lee, J.-Y. Go, *Electrochemistry of Insertion Materials for Hydrogen and Lithium*; Monographs in Electrochemistry; Springer Berlin Heidelberg: Berlin, Heidelberg, 2012.

[136] F. Nasirpouri, *Electrodeposition of Nanostructured Materials*; Springer Series in Surface Sciences; Springer International Publishing: Cham, 2017; Vol. 62.

[137] K. Mehdi, E. Abolfath, *Iran. J. Hydrog. Fuel Cell* **2015**, *1*, 7.

[138] D. Sobha Jayakrishnan, In *Corrosion Protection and Control Using Nanomaterials*; Elsevier, 2012; pp. 86–125.

[139] S. Paul, *Nanomater. Energy* **2015**, *4*, 80.

[140] C. Huang, C. Bunmi Odetola, M. Rodgers, *Appl. Catal. A Gen.* **2015**, *499*, 55.

[141] S. Domínguez-Domínguez, J. Arias-Pardilla, Á. Berenguer-Murcia, E. Morallón, D. Cazorla-Amorós, *J. Appl. Electrochem.* **2008**, *38*, 259.

[142] Y. Zhao, L. Fan, H. Zhong, Y. Li, S. Yang, *Adv. Funct. Mater.* **2007**, *17*, 1537.

[143] M. Yaldagard, N. Seghatoleslami, M. Jahanshahi, *Appl. Surf. Sci.* **2014**, *315*, 222.

[144] C. Paoletti, A. Cemmi, L. Giorgi, R. Giorgi, L. Pilloni, E. Serra, M. Pasquali, *J. Power Sources* **2008**, *183*, 84.

[145] X. Hu, O. Takai, N. Saito, *Jpn. J. Appl. Phys.* **2013**, *52*, 01AN05.

[146] H.-T. Kim, J.-K. Lee, J. Kim, *J. Power Sources* **2008**, *180*, 191.

[147] M. Kim, S. Osone, T. Kim, H. Higashi, T. Seto, *KONA Powder Part. J.* **2017**, *34*, 80.

[148] T. B. Nguyen, T. D. Nguyen, Q. D. Nguyen, T. T. Nguyen, *Adv. Nat. Sci. Nanosci. Nanotechnol.* **2014**, *5*, 035011.

[149] A. Abedini, A. R. Daud, M. A. Abdul Hamid, N. Kamil Othman, E. Saion, *Nanoscale Res. Lett.* **2013**, *8*, 474.

[150] J. L. H. Chau, C.-Y. Chen, C.-C. Yang, *Arab. J. Chem.* **2017**, *10*, S1395.

[151] M. Chandra, P. K. Das, *Int. J. Green Nanotechnol. Phys. Chem.* **2009**, *1*, P10.

[152] N. Dahal, S. García, J. Zhou, S. M. Humphrey, *ACS Nano* **2012**, *6*, 9433.

[153] W. X. Chen, J. Y. Lee, Z. Liu, *Chem. Commun.* **2002**, *8*, 2588.

[154] J. J. Hinman, K. S. Suslick, *Top. Curr. Chem.* **2017**, *375*, 12.

[155] H.-U. Park, E. Lee, Y.-U. Kwon, *Int. J. Hydrogen Energy* **2017**, *42*, 19885.

[156] D. S. Choi, A. W. Robertson, J. H. Warner, S. O. Kim, H. Kim, *Adv. Mater.* **2016**, *28*, 7115.

[157] K. Miyatake, Y. Shimizu, *ACS Omega* **2017**, *2*, 2085.

[158] X. Lu, X. Song, C. Gu, H. Ren, Y. Sun, J. Huang, *J. Phys. Chem. Solids* **2018**, *116*, 324.

[159] H. Chen, D. Wang, Y. Yu, K. A. Newton, D. A. Muller, H. Abruña, F. J. DiSalvo, *J. Am. Chem. Soc.* **2012**, *134*, 18453.

[160] J. Wu, J. Zhang, Z. Peng, S. Yang, F. T. Wagner, H. Yang, *J. Am. Chem. Soc.* **2010**, *132*, 4984.

[161] C. Jiang, G. Huang, S.-J. Ding, H. Dong, C. Men, Y. Mei, *Nanoscale Res. Lett.* **2016**, *11*, 289.

[162] S. Prabhudev, M. Bugnet, G.-Z. Zhu, C. Bock, G. A. Botton, *ChemCatChem* **2015**, *7*, 3655.

[163] M. Hiramatsu, M. Hori, *Materials (Basel).* **2010**, *3*, 1559.

[164] T. Machino, W. Takeuchi, H. Kano, M. Hiramatsu, M. Hori, *Appl. Phys. Express* **2009**, *2*, 025001.

[165] E. Favry, D. Wang, D. Fantauzzi, J. Anton, D. S. Su, T. Jacob, N. Alonso-Vante, *Phys. Chem. Chem. Phys.* **2011**, *13*, 9201.

[166] A. J. Moreira, N. Ordonez, R. D. Mansano, *Nanomater. Nanotechnol.* **2013**, *3*, 15.

[167] L. S. Birks, H. Friedman, *J. Appl. Phys.* **1946**, *17*, 687.

[168] L. S. Birks, H. Friedman, *J. Appl. Phys.* **1946**, *17*, 687.

[169] A. L. Patterson, *Phys. Rev.* **1939**, *56*, 978.

[170] M. Zhang, R. Wang, X. Wu, J. Wang, *Sci. China Physics, Mech. Astron.* **2012**, *55*, 1335.

[171] R. Brunner, F. E. Talke, *Tribol. Lett.* **2010**, *40*, 23.

[172] a. Levasseur, P. Vinatier, D. Gonbeau, *Bull. Mater. Sci.* **1999**, *22*, 607.

[173] D. N. Leonard, G. W. Chandler, S. Seraphin, In *Characterization of Materials*; John Wiley & Sons, Inc.: Hoboken, NJ, USA, NJ, USA, 2012; pp. 1721–1734.

[174] D. H. Anjum, *IOP Conf. Ser. Mater. Sci. Eng.* **2016**, *146*, 012001.

[175] M. Scimeca, S. Bischetti, H. K. Lamsira, R. Bonfiglio, E. Bonanno, *Eur. J. Histochem.* **2018**, *62*, 89.

[176] B. Tang, Y. Lv, J. Du, Y. Dai, S. Pan, Y. Xie, J. Zou, *ACS Sustain. Chem. Eng.* **2019**, *7*, 11101.

[177] L. Mendes, J. L. de Medeiros, R. M. B. Alves, O. Q. F. Araújo, *Clean Technol. Environ. Policy* **2014**, *16*, 1095.

[178] Y. S. H. Najjar, *Clean Technol. Environ. Policy* **2008**, *10*, 269.

[179] R. Rashidi, I. Dincer, G. F. Naterer, P. Berg, *J. Power Sources* **2009**, *187*, 509.

[180] R. Dillon, S. Srinivasan, A. S. Aricò, V. Antonucci, *J. Power Sources* **2004**, *127*, 112.

[181] T. Elmer, M. Worall, S. Wu, S. B. Riffat, *Renew. Sustain. Energy Rev.* **2015**, *42*, 913.

[182] A. Heinzel, V. M. Barragán, *J. Power Sources* **1999**, *84*, 70.

[183] E. Drioli, A. Basile, A. Criscuoli, *Clean Prod. Process.* **2000**, *2*, 0179.

[184] H. Liu, C. Song, L. Zhang, J. Zhang, H. Wang, D. P. Wilkinson, *J. Power Sources* **2006**, *155*, 95.

[185] C. Li, Y. Yamauchi, *Phys. Chem. Chem. Phys.* **2013**, *15*, 3490.

[186] J. N. Tiwari, R. N. Tiwari, G. Singh, K. S. Kim, *Nano Energy* **2013**, *2*, 553.

[187] S. Wasmus, A. Küver, *J. Electroanal. Chem.* **1999**, *461*, 14.

[188] A. S. Aricò, S. Srinivasan, V. Antonucci, *Fuel Cells* **2001**, *1*, 133.

[189] Z. Cui, C. M. Li, S. P. Jiang, *Phys. Chem. Chem. Phys.* **2011**, *13*, 16349.

[190] Y. Lu, Y. Jiang, H. Wu, W. Chen, *J. Phys. Chem. C* **2013**, *117*, 2926.

[191] L. Shi, R.-P. Liang, J.-D. Qiu, *J. Mater. Chem.* **2012**, *22*, 17196.

[192] W. Chen, J. Wang, C. Hsu, J. Jhan, H. Teng, P. Kuo, *J. Phys. Chem. C* **2010**, *114*, 6976.

[193] Y. Meng, L. Aldous, B. S. Pilgrim, T. J. Donohoe, R. G. Compton, *New J. Chem.* **2011**, *35*, 1369.

[194] Y. Zhao, L. Zhan, J. Tian, S. Nie, Z. Ning, *Electrochim. Acta* **2011**, *56*, 1967.

[195] Z.-Y. Shih, C.-W. Wang, G. Xu, H.-T. Chang, *J. Mater. Chem. A* **2013**, *1*, 4773.

[196] H. Huang, X. Wang, *J. Mater. Chem.* **2012**, *22*, 22533.

[197] J. Zeng, J. Y. Lee, W. Zhou, *J. Power Sources* **2006**, *159*, 509.

[198] H. Zhao, L. Li, J. Yang, Y. Zhang, H. Li, *Electrochem. commun.* **2008**, *10*, 876.

[199] M. Carmo, A. R. dos Santos, J. G. R. Poco, M. Linardi, *J. Power Sources* **2007**, *173*, 860.

[200] B. Wu, D. Hu, Y. Yu, Y. Kuang, X. Zhang, J. Chen, *Chem. Commun.* **2010**, *46*, 7954.

[201] S. Wang, X. Wang, S. P. Jiang, *Langmuir* **2008**, *24*, 10505.

[202] Y. Wang, Q. He, J. Guo, H. Wei, K. Ding, H. Lin, S. Bhana, X. Huang, Z. Luo, T. D. Shen, S. Wei, Z. Guo, *ChemElectroChem* **2015**, *2*, 559.

[203] Y.-H. Qin, H.-H. Yang, X.-S. Zhang, P. Li, C.-A. Ma, *Int. J. Hydrogen Energy* **2010**, *35*, 7667.

[204] Y. Li, W. Gao, L. Ci, C. Wang, P. M. Ajayan, *Carbon N. Y.* **2010**, *48*, 1124.

[205] C. Nethravathi, E. A. Anumol, M. Rajamathi, N. Ravishankar, *Nanoscale* **2011**, *3*, 569.

[206] M. Satyanarayana, K. Y. Goud, K. K. Reddy, K. V. Gobi, *Electrochim. Acta* **2015**, *178*, 608.

[207] M. Satyanarayana, K. Koteshwara Reddy, K. Vengatajalabathy Gobi, *Electroanalysis* **2014**, *26*, 2365.

[208] M. Satyanarayana, K. K. Reddy, K. V. Gobi, *Anal. Methods* **2014**, *6*, 3772.

[209] H. An, L. Pan, H. Cui, D. Zhou, B. Wang, J. Zhai, Q. Li, Y. Pan, *J. Electroanal. Chem.* **2015**, *741*, 56.

[210] R. Awasthi, R. N. Singh, *Int. J. Hydrogen Energy* **2012**, *37*, 2103.

[211] R. N. Singh, A. Singh, Anindita, *Int. J. Hydrogen Energy* **2009**, *34*, 2052.

[212] Y. Liu, Y. Huang, Y. Xie, Z. Yang, H. Huang, Q. Zhou, *Chem. Eng. J.* **2012**, *197*, 80.

[213] K. Wu, Q. Zhang, D. Sun, X. Zhu, Y. Chen, T. Lu, Y. Tang, *Int. J. Hydrogen Energy* **2015**, *40*, 6530.

[214] C. Bianchini, P. K. Shen, *Chem. Rev.* **2009**, *109*, 4183.

[215] A. Chen, C. Ostrom, *Chem. Rev.* **2015**, *115*, 11999.

[216] Y. Yan, J. Miao, Z. Yang, F.-X. Xiao, H. Bin Yang, B. Liu, Y. Yang, *Chem. Soc. Rev.* **2015**, *44*, 3295.

[217] W. Li, C. Liang, W. Zhou, J. Qiu, Zhou, G. Sun, Q. Xin, *J. Phys. Chem. B* **2003**, *107*, 6292.

[218] W. Yuan, S. Lu, Y. Xiang, S. P. Jiang, *RSC Adv.* **2014**, *4*, 46265.

[219] L. Tao, S. Dou, Z. Ma, S. Wang, *Electrochim. Acta* **2015**, *157*, 46.

[220] V. S. Kumar, M. Satyanarayana, K. Y. Goud, K. V. Gobi, *Clean Technol. Environ. Policy* **2018**, *20*, 759.

[221] R. Sharma, J. H. Baik, C. J. Perera, M. S. Strano, *Nano Lett.* **2010**, *10*, 398.

[222] G. G. Wildgoose, C. E. Banks, R. G. Compton, *Small* **2006**, *2*, 182.

[223] M. Busson, A. Berisha, C. Combellas, F. Kanoufi, J. Pinson, *Chem. Commun.* **2011**, *47*, 12631.

[224] M. Satyanarayana, K. Y. Goud, K. K. Reddy, V. S. Kumar, K. V. Gobi, *Mater. Sci. Eng. C* **2019**, *101*, 103.

[225] A. Kalaiselvi, S. M. Roopan, G. Madhumitha, C. Ramalingam, G. Elango, *Spectrochim. Acta Part A Mol. Biomol. Spectrosc.* **2015**, *135*, 116.

[226] J.-N. Zheng, S.-S. Li, X. Ma, F.-Y. Chen, A.-J. Wang, J.-R. Chen, J.-J. Feng, *J. Power*

Sources **2014**, *262*, 270.

[227] A. B. A. A. Nassr, A. Quetschke, E. Koslowski, M. Bron, *Electrochim. Acta* **2013**, *102*, 202.

[228] C.-C. Chen, C.-L. Lin, L.-C. Chen, *Electrochim. Acta* **2015**, *152*, 408.

[229] R. N. Singh, A. Singh, Anindita, *Int. J. Hydrogen Energy* **2009**, *34*, 2052.

[230] R. Pattabiraman, *Appl. Catal. A Gen.* **1997**, *153*, 9.

[231] V. Sunil Kumar, S. Kummari, K. Yugender Goud, M. Satyanarayana, K. Vengatajalabathy Gobi, *Int. J. Hydrogen Energy* **2020**, *45*, 1018.

[232] S. Guo, S. Li, T. Hu, G. Gou, R. Ren, J. Huang, M. Xie, J. Jin, J. Ma, *Electrochim. Acta* **2013**, *109*, 276.

[233] B. Choi, W. Nam, D. Young, I. Park, S. Jong, *Electrochim. Acta* **2015**, *164*, 235.

[234] Y. Zhao, X. Yang, J. Tian, F. Wang, L. Zhan, *Int. J. Hydrogen Energy* **2010**, *35*, 3249.

[235] S. Jiang, L. Zhu, Y. Ma, X. Wang, J. Liu, J. Zhu, Y. Fan, Z. Zou, Z. Hu, *J. Power Sources* **2010**, *195*, 7578.

[236] M. Satyanarayana, G. Rajeshkhanna, M. K. Sahoo, G. R. Rao, *ACS Appl. Energy Mater.* **2018**, *1*, 3763.

[237] M. Sedighi, A. A. Rostami, E. Alizadeh, *Int. J. Hydrogen Energy* **2017**, *42*, 4998.

[238] H. Huang, X. Wang, *Phys. Chem. Chem. Phys.* **2013**, *15*, 10367.

[239] Y. Zhang, Y. Wang, J. Jia, J. Wang, *Int. J. Hydrogen Energy* **2012**, *37*, 17947.

[240] P. Justin, P. Hari Krishna Charan, G. Ranga Rao, *Appl. Catal. B Environ.* **2010**, *100*, 510.

[241] A. Kumar, N. Kumari, V. K. V. P. Srirapu, R. N. Singh, *Int. J. Hydrogen Energy* **2018**, *43*, 9677.

[242] C. Zhai, M. Sun, M. Zhu, K. Zhang, Y. Du, *Int. J. Hydrogen Energy* **2017**, *42*, 5006.

[243] S. H. Patil, B. Anothumakkool, S. D. Sathaye, K. R. Patil, *Phys. Chem. Chem. Phys.* **2015**, *17*, 26101.

[244] P. Cui, H. He, H. Liu, S. Zhang, J. Yang, *J. Power Sources* **2016**, *327*, 432.

[245] H. Bolivar, S. Izquierdo, R. Tremont, C. R. Cabrera, *J. Appl. Electrochem.* **2003**, *33*, 1191.

[246] M. Satyanarayana, K. Y. Goud, K. K. Reddy, K. V. Gobi, *Electrochim. Acta* **2015**, *178*, 608.

[247] V. S. Kumar, M. Satyanarayana, K. Y. Goud, K. V. Gobi, *Clean Technol. Environ. Policy* **2018**, *20*, 759.

[248] D. Rajesh, C. Mahendiran, C. Suresh, A. Pandurangan, T. Maiyalagan, *Int. J. Hydrogen Energy* **2019**, *44*, 4962.

[249] C. Xu, L. Cheng, P. Shen, Y. Liu, *Electrochem. commun.* **2007**, *9*, 997.

[250] R. Kiyani, M. J. Parnian, S. Rowshanzamir, *Int. J. Hydrogen Energy* **2017**, *42*, 23070.

[251] Z. Li, L. Zhang, C. Yang, J. Chen, Z. Wang, L. Bao, F. Wu, P. Shen, *Int. J. Hydrogen Energy* **2019**, *44*, 6172.

[252] X. Yu, F. Luo, Q. Zhang, L. Guo, H. Hu, Z. Yang, S. A. Grigoriev, H. Cheng, *Int. J. Hydrogen Energy* **2019**, 1.

[253] Y. Zhu, S. Murali, W. Cai, X. Li, J. W. Suk, J. R. Potts, R. S. Ruoff, *Adv. Mater.* **2010**, *22*, 3906.

[254] S. Esabattina, V. R. Posa, H. Zhanglian, S. kumar Godlaveeti, R. R. Nagi Reddy, A. R. Somala, *Int. J. Hydrogen Energy* **2018**, *43*, 4115.

[255] K. Zhang, X. Chen, L. Wang, D. Zhang, Z. Xue, X. Zhou, X. Lu, *Int. J. Hydrogen Energy* **2018**, *43*, 15931.

[256] N. Li, Z. Wang, K. Zhao, Z. Shi, Z. Gu, S. Xu, *Carbon N. Y.* **2010**, *48*, 255.

[257] L. Zhao, X. L. Sui, Q. Y. Zhou, J. Z. Li, J. J. Zhang, G. S. Huang, Z. B. Wang, *J. Mater. Chem. A* **2018**, *6*, 6212.

[258] X. Li, H. Wang, J. T. Robinson, H. Sanchez, G. Diankov, H. Dai, *J. Am. Chem. Soc.* **2009**, *131*, 15939.

[259] H. Huang, L. Ma, C. S. Tiwary, Q. Jiang, K. Yin, W. Zhou, P. M. Ajayan, *Small* **2017**, *13*, 1603013.

[260] M. Yan, Q. Jiang, T. Zhang, J. Wang, L. Yang, Z. Lu, H. He, Y. Fu, X. Wang, H. Huang, *J. Mater. Chem. A* **2018**, *6*, 18165.

[261] W. Zhang, H. Huang, F. Li, K. Deng, X. Wang, *J. Mater. Chem. A* **2014**, *2*, 19084.

[262] H. Qian, H. Huang, X. Wang, *J. Power Sources* **2015**, *275*, 734.

[263] L.-M. Luo, R.-H. Zhang, J.-J. Du, F. Yang, H.-M. Liu, Y. Yang, X.-W. Zhou, *Int. J. Hydrogen Energy* **2017**, *42*, 16139.

[264] L.-M. Luo, R.-H. Zhang, D. Chen, Q.-Y. Hu, X. Zhang, C.-Y. Yang, X.-W. Zhou, *Electrochim. Acta* **2018**, *259*, 284.

[265] R. I. Jafri, N. Rajalakshmi, K. S. Dhathathreyan, S. Ramaprabhu, *Int. J. Hydrogen Energy* **2015**, *40*, 4337.

[266] D. Chen, C. Li, H. Liu, F. Ye, J. Yang, *Sci. Rep.* **2015**, *5*, 11949.

[267] M. Narreddula, R. Balaji, K. Ramya, N. Rajalakshmi, A. Ramachandraiah, *Int. J. Hydrogen*

Energy **2019**, *44*, 4582.

[268] L. Zhao, Z.-B. Wang, J.-L. Li, J.-J. Zhang, X.-L. Sui, L.-M. Zhang, *J. Mater. Chem. A* **2015**, *3*, 5313.

[269] L. Zhao, X.-L. Sui, J.-L. Li, J.-J. Zhang, L.-M. Zhang, Z.-B. Wang, *ACS Appl. Mater. Interfaces* **2016**, *8*, 16026.

[270] L. S. Panchakarla, K. S. Subrahmanyam, S. K. Saha, A. Govindaraj, H. R. Krishnamurthy, U. V. Waghmare, C. N. R. Rao, *Adv. Mater.* **2009**, *21*, NA.

[271] A. M. Hofstead-Duffy, D. J. Chen, S. G. Sun, Y. J. Tong, *J. Mater. Chem.* **2012**, *22*, 5205.

[272] Y. Zhao, L. Zhan, J. Tian, S. Nie, Z. Ning, *Int. J. Hydrogen Energy* **2010**, *35*, 10522.

[273] X. Wang, B. Tang, X. Huang, Y. Ma, Z. Zhang, *J. Alloys Compd.* **2013**, *565*, 120.

[274] Z. Yin, M. Chi, Q. Zhu, D. Ma, J. Sun, X. Bao, *J. Mater. Chem. A* **2013**, *1*, 9157.

[275] L. Zhang, H. Wang, X. Li, F. Xia, Y. Liu, X. Xu, J. Gao, F. Xing, *Electrochim. Acta* **2015**, *172*, 42.

[276] M. Wang, Z. Ma, R. Li, B. Tang, X.-Q. Bao, Z. Zhang, X. Wang, *Electrochim. Acta* **2017**, *227*, 330.

[277] L. Gong, Z. Yang, K. Li, W. Xing, C. Liu, J. Ge, *J. Energy Chem.* **2018**, *27*, 1618.

[278] N. A. Karim, S. K. Kamarudin, *Appl. Energy* **2013**, *103*, 212.

[279] H. T. Zheng, Y. Li, S. Chen, P. K. Shen, *J. Power Sources* **2006**, *163*, 371.

[280] X. Huang, X. Qi, F. Boey, H. Zhang, *Chem. Soc. Rev.* **2012**, *41*, 666.

[281] S. C. Sahu, B. Satpati, L. Besra, B. K. Jena, *ChemCatChem* **2015**, *7*, 4042.

[282] A. Renjith, V. Lakshminarayanan, *J. Mater. Chem. A* **2015**, *3*, 3019.

[283] K. Mandal, D. Bhattacharjee, P. S. Roy, S. K. Bhattacharya, S. Dasgupta, *Appl. Catal. A Gen.* **2015**, *492*, 100.

[284] M. Kübler, T. Jurzinsky, D. Ziegenbalg, C. Cremers, *J. Power Sources* **2018**, *375*, 320.

[285] E. J. Lim, Y. Kim, S. M. Choi, S. Lee, Y. Noh, W. B. Kim, *J. Mater. Chem. A* **2015**, *3*, 5491.

[286] Y. Zhao, L. Zhan, J. Tian, S. Nie, Z. Ning, *Int. J. Hydrogen Energy* **2010**, *35*, 10522.

[287] Y. Chu, N. Zhang, J. Yang, H. Wang, Z. Dai, L. Wang, J. Gao, X. Tan, *J. Mater. Sci.* **2018**, *53*, 2087.

[288] P. Justin, G. Ranga Rao, *Int. J. Hydrogen Energy* **2011**, *36*, 5875.

[289] P. Justin, G. R. Rao, *Catal. Today* **2009**, *141*, 138.

[290] R. A. Gonçalves, M. R. Baldan, E. G. Ciapina, O. M. Berengue, *Appl. Surf. Sci.* **2019**, *491*, 9.

[291] C. C. Mayorga-Martinez, A. Ambrosi, A. Y. S. Eng, Z. Sofer, M. Pumera, *Electrochem. commun.* **2015**, *56*, 24.

[292] K. Selvarani, A. Prabhakaran, P. Arumugam, S. Berchmans, P. Nayak, *Microchim. Acta* **2018**, *185*, 411.

[293] A. Eftekhari, *Appl. Mater. Today* **2017**, *8*, 1.

[294] J. Li, X. Liu, L. Pan, W. Qin, T. Chen, Z. Sun, *RSC Adv.* **2014**, *4*, 9647.

[295] R. Kumar, E. T. S. G. da Silva, R. K. Singh, R. Savu, A. V. Alaferdov, L. C. Fonseca, L. C. Carossi, A. Singh, S. Khandka, K. K. Kar, O. L. Alves, L. T. Kubota, S. A. Moshkalev, *J. Colloid Interface Sci.* **2018**, *515*, 160.

[296] M. J. Fernández-Merino, L. Guardia, J. I. Paredes, S. Villar-Rodil, P. Solís-Fernández, A. Martínez-Alonso, J. M. D. Tascón, *J. Phys. Chem. C* **2010**, *114*, 6426.

[297] J. Guo, Y. Shi, X. Bai, X. Wang, T. Ma, *J. Mater. Chem. A* **2015**, *3*, 24397.

[298] M. D. Sharma, C. Mahala, M. Basu, *J. Colloid Interface Sci.* **2019**, *534*, 131.

[299] H. Tang, K. Dou, C.-C. Kaun, Q. Kuang, S. Yang, *J. Mater. Chem. A* **2014**, *2*, 360.

[300] Y. Song, X. Zhang, S. Yang, X. Wei, Z. Sun, *Fuel* **2016**, *181*, 269.

[301] M. Wang, Z. Ma, R. Li, B. Tang, X.-Q. Bao, Z. Zhang, X. Wang, *Electrochim. Acta* **2017**, *227*, 330.

[302] W. Zhang, H. Huang, F. Li, K. Deng, X. Wang, *J. Mater. Chem. A* **2014**, *2*, 19084.

[303] F. Yang, B. Zhang, S. Dong, Y. Tang, L. Hou, Z. Chen, Z. Li, W. Yang, C. Xu, M. Wang, Y. Li, Y. Li, *Appl. Surf. Sci.* **2018**, *452*, 11.

LIST OF PUBLICATIONS & BIO-DATA

Publications in Peer-Reviewed/Refereed International Journals

1. Pd nanoparticles embedded carbon nanotube interface for electrocatalytic oxidation of methanol Toward DMFC applications.
V. Sunil Kumar, M. Satyanarayana, K. Yugender Goud, K. Vengatajalabathy Gobi*
Clean Technologies and Environmental Policy (2018) 20, 759–768.

2. One-pot Synthesis of $Pd_{20-x}Au_x$ Nanoparticles Embedded in Nitrogen Doped Graphene as High-Performance Electrocatalysts Toward Methanol Oxidation.
V. Sunil Kumar, Shekher Kummari, K. Yugender Goud, M. Satyanarayana, K. Vengatajalabathy Gobi*
International Journal of Hydrogen Energy (2020) 45, 1018-1029

3. Pd nanocrystals grown on three-dimensional architectures made from graphene and $MoSe_2$ nanosheets: Highly efficient electrocatalysts toward methanol oxidation.
V. Sunil Kumar, Shekher Kummari, M. Satyanarayana, K. Yugender Goud, K. Vengatajalabathy Gobi* **(About to communicate)**

4. Palladium Nanoparticles Supported on Nitrobenzene-Functionalized Multiwalled Carbon Nanotube as Efficient Electrocatalysts for Methanol Oxidation.
V. Sunil Kumar, Shekher Kummari, K. Yugender Goud, M. Satyanarayana, K. Vengatajalabathy Gobi* **(Manuscript under preparation)**

Publications in Peer-Reviewed/Refereed International Conference Proceedings

1. "Synthesis and Characterization of Au-Chit-Pd Supported on Carbon Nanotubes for Highly Active Methanol Electro-oxidation in Alkaline Media"

   Sunil Kumar V., Satyanarayana M., Gobi K. V.

   MATCON-2016: VOLUME 2, PAGE 441-443 ISBN No: 978-93-80095-738

BIO-DATA

V. Sunil Kumar

Contact Address

S/O. Upender

H.NO: 2-6-612

APHB Colony, Hanamkonda

Warangal (District) – 506001

Telangana, India.

E-mail: sunilkumarvenishetty@gmail.com

venishettysunil@student.nitw.ac.in

Mobile: +91-9052041623

Objective: To be professionally associated with an organization, where I can utilize my Doctoral Research experience in solving the practical challenges and achieve the goals of the organization

Academic Qualifications:

December 2014 – Present: **Research Scholar (PhD Student)**

Under the supervision of **Prof. K. V. Gobi**, Department of Chemistry, National Institute of Technology Warangal, Telangana, India

Research Topic: "Development of Palladium and Non-noble Metal Based Nanocomposite Electrocatalysts Toward Methanol Oxidation in DMFC Applications"

Status: To be awarded (Thesis submitted)

June 2013 – August 2014: **Bachelor of Education (Physical Science and Biological Science)**

Kakatiya University, Warangal, Telangana, India

Percentage of Marks: **72.0 (First Division)**

July 2009 – June 2011: **Master of Science in Chemistry**

Kakatiya University, Warangal, Telangana, India

Percentage of Marks: **76.83 (Distinction)**

June 2006 – April 2009:	**Bachelor of Science (Biotechnology, Biochemistry and Chemistry)**
	Kakatiya University, Warangal, Telangana, India
	Percentage of Marks: **80.83 (Distinction)**
June 2003 – March 2005:	**Intermediate (Botany, Zoology, Physics and Chemistry)**
	Board of Intermediate Education, Andhra Pradesh, India
	Percentage of Marks: **89.20 (Distinction)**
June 2002– March 2003:	**Secondary School Certificate (High School)**
	Board of Secondary Education, Andhra Pradesh, India
	Percentage of Marks: **85.16 (Distinction)**

Professional Summary:

- **Ph.D. Research Fellow** at National Institute of Technology, Warangal, Telangana, India, from December 2014 to till date.

Personal Details:

- Name : V. Sunil Kumar.
- Father's Name : Upender
- Date of Birth : 10-05-1987
- Gender : Male
- Marital Status : Married
- Nationality : Indian
- Languages Known : <u>Telugu</u>, English and Hindi

Achievements:

- Received "**Best Oral Presentation Award**"at Asia Pacific Congress on Catalysis (**APCAT-7**). The Hotel Lalit, Mumbai, India, January 17-21, 2017.

- Qualified Graduate Aptitude Test in Engineering (**GATE**) 2014.

- Secured 2nd rank in B. Sc (Biotechnology, Biochemistry and Chemistry) 2009, Chaitanya Degree and PG college, Hanamkonda, Warangal, Telangana, India 506001

Technical Skills:

- Expertise in utilizing the software - Microsoft Office, Ngraph, Origin etc., Cemistry Related software - ChemDraw Ultra 12.0, HyperChem Release - 8.0.9, X'Pert HighScore Plus.

- Expertise in MENDELEY Reference Manager.

Expertise in Instrumental Techniques:

- Electrochemical Impedance Analyzer, Zahner-Elektrik (IM6e), GmbH, Germany

- Electrochemical Workstation, Sinsil CHI 619D and CHI6132e.

- UV-Visible Spectrophotometers, Analytik Jena Specord 205 and Shimadzu 1601

- FTIR Spectrophotometer, PerkinElmer

- Raman spectrometer, HR800 LabRAM confocal

- Scanning Electron Microscope, VEGA3, Tescon, USA

- Other small instruments relevant for materials characterization and analysis

Research Interests:

- Nanostructured Materials synthesis and characterization

- Biosensors and Electrochemical Sensors

- Nanostructured Materials

- Nano-composites towards Practical Applications of Electrochemistry.

- Electrochemical Techniques

Other Capabilities:

- Capable of carrying out both collaborative and independent research
- Motivated strong ethics and providing efficient service

- Very good interpersonal and communication skills along with management skills

- Good experience in writing technical papers, presentations and reports

- Guided many post-graduate students for their projects